Hadronic Energy Flow in Deep Inelastic Electron–Proton Scattering and Proton Structure at low Bjorken x.

Thesis submitted in accordance with the requirements of the University of Liverpool for the degree of Doctor of Philosophy

by

Tania Ebert

March 1995

Oliver Lodge Laboratory
University of Liverpool

Hadronic Energy Flow in Deep Inelastic Electron–Proton Scattering and Proton Structure at low Bjorken x.

Tania Ebert

Abstract

The electron-proton collider HERA has opened up a new kinematic region in which the structure of the proton can be studied. In particular it allows measurements to be made at low Bjorken x, where the gluon content of the proton is expected to be large and where novel QCD effects may be observed.

This thesis presents a first attempt at understanding the composition of the proton by studying the colour structure of the proton remnant in neutral current electron-proton deep inelastic scattering in the kinematic region $10^{-4} < x < 10^{-2}$ and $5 < Q^2 < 100\ GeV^2$. It is demonstrated that the way in which the total available energy is distributed in the hadronic final state depends on the nature of the colour force between the proton remnant and the final state partons. This observation is subsequently used to measure the fraction of gluon initiated events ($\gamma^* g \rightarrow q\bar{q}$), in which the proton remnant has a colour octet structure, as a function of x and Q^2. The interpretation of the result in terms of the gluon density in the proton is also discussed.

Acknowledgements

It is of course not possible to thank everyone who has been helpful to me during the three years of my PhD, and I apologise to those who aren't mention explicitly.

I would like to thank my supervisor, Professor John Dainton, for all his guidance and enthusiasm. Much thanks is also due to the other members of the Liverpool H1 group, in particular to Tim Greenshaw and Steve Maxfield, who have worked hard on the interpretation of the measurement made in this thesis, as well as answering countless stupid questions. I would also like to thank Roly Martin for his assistance during the past three years.

The work for this thesis would not have been possible without the financial support of the Particle Physics and Astronomy Research Council [1] and the hospitality of the DESY laboratory.

I would also like to thank Gunnar Ingelman, the author of LEPTO, the Monte Carlo used throughout this thesis.

Thanks is due to my parents and my sister Nicola, whose daily e-mail was much appreciated. I would also like to thank all my friends in Hamburg who made the time I spent there very enjoyable indeed (even if they don't appreciate good music.)

Finally, I would like to thank Steve McMahon, without whose unfailing help, support and encouragement none of this would have been possible.

[1] Formerly part of the Science and Engineering Research Council

To my parents

Contents

Chapter 1

Introduction

Historically, deep inelastic lepton-nucleon scattering experiments have played a fundamental role in our understanding of the structure of matter. They have led to the development of our model of the proton as a composite structure consisting of three valence quarks and a fluctuating sea of virtual gluons and quark-antiquark pairs. The strong force which binds the partons together is a consequence of the fact that they have a colour charge, in direct analogy to the force which exists between electrically charged particles. This colour force is described by the theory of Quantum Chromodynamics (QCD).

The electron-proton collider HERA has opened up a new kinematic region in which the constituents of the proton can be studied. The highest attainable Q^2 is of order $10^5\ GeV^2$, corresponding to a spatial resolution of about 10^{-18} m, and the lowest x is of order 10^{-5}. This is at least two orders of magnitude higher in Q^2 and two orders of magnitude lower in x than has been previously achieved by fixed target experiments. There are many questions about proton structure in this low x region which the HERA experiments may be able to answer. For example, although the gluon density in the proton is predicted to rise with decreasing x, neither its magnitude nor the steepness of the rise have ever been measured. In addition, the evolution of the parton densities with Q^2 may no longer follow the standard QCD prediction. The low x region is also theoretically challenging as the QCD interpretation of observations made in this region may be more naturally associated with photon rather than proton structure.

This thesis describes a first attempt at understanding the composition of

the proton at low x by studying the colour structure of the proton remnant in neutral current deep inelastic scattering. The approach is experimental, based on the observation that the distribution of energy in the hadronic final state depends on the colour force between partons before hadronization. The aim has been to measure the fraction of events in which a gluon has been removed from the proton, therefore leaving the remnant in a colour octet state. Although the interpretation of this measurement is theoretically complex, one possible method for extracting the gluon density within the proton is outlined in this thesis.

The content of this thesis is as follows. The theory of deep inelastic scattering is outlined in chapter 2 and the H1 detector is described in chapter 3. The selection of a sample of low Q^2 neutral current deep inelastic scattering events is explained in chapter 4. Chapter 6 is a study of the basic properties of the hadronic final state and in chapter 7 it is shown that the observed energy flow in the hadronic final state is related to the colour force between partons before hadronization. Finally the method used to measure the fraction of gluon initiated processes is outlined in chapter 8 and the interpretation of the result in terms of the gluon density in the proton is discussed.

Chapter 2

Deep Inelastic Scattering

2.1 Introduction

A schematic diagram showing the kinematics of a deep-inelastic scattering (DIS) event is shown in figure 2.1. The incoming lepton (electron or positron) interacts with a parton in the proton via the exchange of a virtual boson (Z^0 or γ for neutral current events and $W^{\pm}$ for charged current events). If the 4-momentum of the incident lepton is k and that of the scattered lepton is k' then the 4-momentum of the exchanged boson is $q = k - k'$.

The kinematics of a DIS event are usually defined in terms of the Lorentz invariant quantities x, Q^2, y and W. Q^2 is the negative square of the four-momentum transfer:

$$Q^2 = -q^2 = -(k - k')^2 \tag{2.1}$$

and defines the resolving power of the probe. The Bjorken scaling variable x is defined as:

$$x = \frac{Q^2}{2P \cdot q} \tag{2.2}$$

where P is the four-momentum of the incident proton. It can be thought of as that fraction of the incident proton's momentum which is carried by the struck parton in the infinite momentum frame of the proton. The same interpretation is possible if the partons are assumed to be massless. The variable y:

$$y = \frac{P \cdot q}{P \cdot k} \tag{2.3}$$

is equivalent either to the fractional energy loss of the lepton in the rest frame

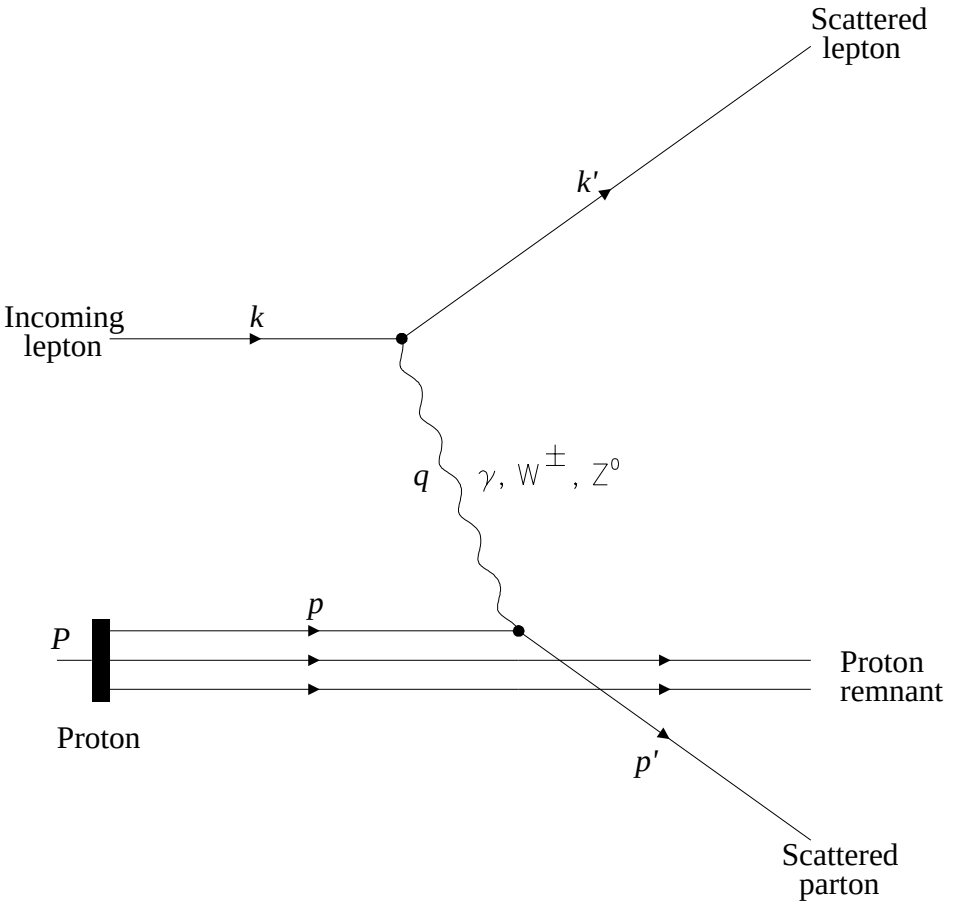

Figure 2.1: Schematic diagram of a DIS event.

of the proton, or to $\frac{1}{2}(1 - \cos\theta^*)$, where θ^* is the polar angle of the scattered lepton in the parton-lepton centre of mass frame. Both x and y are dimensionless quantities which lie in the range:

$$0 \leq x, y \leq 1$$

Finally, W is the invariant mass of the hadronic final state, given by:

$$W^2 = (q + P)^2. \tag{2.4}$$

The variable ν is also sometimes used. It is defined as the energy loss of the lepton in the rest frame of the proton:

$$\nu = \frac{P \cdot q}{m_p} \tag{2.5}$$

where m_p is the mass of the proton.

Only two of these variables are independent. For example, they are related by the equations:

$$Q^2 = sxy \tag{2.6}$$

where s is the square of the centre of mass energy of the lepton-proton system and:

$$x = \frac{Q^2}{Q^2 + W^2 - m_p^2} \tag{2.7}$$

Also:

$$\nu = \frac{Q^2}{2m_p x} \tag{2.8}$$

2.2 Kinematic Reconstruction

In Neutral Current deep inelastic electron-proton scattering, the kinematic variables can be calculated either from the angle and energy of the scattered electron, from the hadronic final state or by using a combination of the two. In this thesis, the scattered electron alone is used to calculate the event kinematics. Details of the method and its limitations will be discussed here, and details of other methods which can be used can be found elsewhere [1].

If the energy and polar angle (measured with respect to the incident proton direction) of the scattered electron are E'_e and θ_e and the energies of the incident proton and electron are E_p and E_e respectively, the relations in section 2.1 can be written as:

$$Q^2 = 4E_e E'_e \cos^2\left(\frac{\theta_e}{2}\right) \tag{2.9}$$

$$y = 1 - \frac{E'_e}{E_e}\sin^2\left(\frac{\theta_e}{2}\right) \tag{2.10}$$

and:

$$x = \frac{E_e E'_e \cos^2\left(\frac{\theta_e}{2}\right)}{E_p\left\{E_e - E'_e \sin^2\left(\frac{\theta_e}{2}\right)\right\}} \tag{2.11}$$

ignoring particle masses. The sensitivity of the reconstructed x and Q^2 to the accuracy of the measurement of E'_e and θ_e can be investigated by examining the following partial derivatives:

$$\frac{\partial Q^2}{\partial E'_e} = \frac{Q^2}{E'_e} \tag{2.12}$$

$$\frac{\partial Q^2}{\partial \theta_e} = -Q^2 \tan\left(\frac{\theta_e}{2}\right) \tag{2.13}$$

$$\frac{\partial x}{\partial E'_e} = \frac{x}{yE'_e} \tag{2.14}$$

$$\frac{\partial x}{\partial \theta_e} = x\tan\left(\frac{\theta_e}{2}\right)\left(x\frac{E_p}{E_e} - 1\right) \tag{2.15}$$

From these equations, it can be seen that:

- The resolution in Q^2 is dominated by the electron energy resolution, and is therefore very good (a few percent) except at large θ_e (low Q^2) where 2.13 becomes important.
- The error in x due to the angular resolution of the scattered electron is only significant at high x or large θ_e (low Q^2).
- The resolution in x at low y is very poor. This method of kinematic reconstruction is not accurate for measurements of x below $y \approx 0.1$.

2.3 The Quark Parton Model

The differential cross-section for Neutral Current DIS can be written as:

$$\frac{d^2\sigma}{dxdQ^2} = \frac{4\pi\alpha^2}{xQ^2}\left\{y^2 xF_1(x,Q^2) + (1-y)F_2(x,Q^2) + (y-\frac{y^2}{2})F_3(x,Q^2)\right\} \quad (2.16)$$

where α is the fine-structure constant. The three structure functions F_1, F_2 and F_3 describe the proton structure. For values of Q below the mass of the Z^0 boson ($\sim$ 91.2 GeV), the function F_3 is negligible. The data sample used in this thesis covers a range in Q^2 of $5 < Q^2 < 100\ GeV^2$ so we can assume the exchanged boson is always a virtual photon.

In 1969, Bjorken predicted that in the deep inelastic region (large ν and Q^2 but with ν/Q^2 finite) the structure functions should 'scale'; they should not depend explicitly on Q^2 and ν but only on their ratio. This is equivalent to saying that F_1 and F_2 are functions of x alone. Such behaviour of the structure functions was observed experimentally at SLAC in 1972 [2].

The observation of scaling provided the basis for the parton model of the proton. If the proton consists of free, pointlike fermions (partons) and we are observing elastic scattering from these, then the structure functions should depend only on the fraction of the proton's momentum carried by the parton, namely x. In the parton model, the distribution of partons in the proton are described by the parton density functions, $f_i(x)$, which are constrained by the momentum sum rule:

$$\sum_i \int_0^1 x f_i(x)\, dx = 1 \quad (2.17)$$

where the sum is over the different types of parton. These parton densities depend only on x if the partons are free.

In the parton model, the structure function F_2 is related to the parton densities by:

$$F_2(x) = \sum_i e_i^2 x f_i(x) \quad (2.18)$$

and, due to the fact that the partons are fermions (spin $\frac{1}{2}$):

$$F_2 = 2xF_1 \quad (2.19)$$

which is known as the Callan-Gross relation [3].

From 2.18, the structure function F_2 for electron-proton scattering can be written:

$$F_2^{ep}(x) = x\left\{\frac{4}{9}[u^p(x) + \bar{u}^p(x)] + \frac{1}{9}[d^p(x) + \bar{d}^p(x) + s^p(x) + \bar{s}^p(x)]\right\} \tag{2.20}$$

where u^p, for example, refers to the density of up quarks in the proton, and the contribution to the proton structure from charm and heavier quarks is assumed to be small. However, as the proton and the neutron form an isospin doublet, their quark content is related:

$$\begin{aligned} u^p(x) &= d^n(x) \equiv u(x) \\ d^p(x) &= u^n(x) \equiv d(x) \end{aligned}$$

Hence, for electron-neutron scattering we can write:

$$F_2^{en}(x) = x\left\{\frac{4}{9}[d(x) + \bar{d}(x)] + \frac{1}{9}[u(x) + \bar{u}(x) + s(x) + \bar{s}(x)]\right\} \tag{2.21}$$

The quark densities are constrained by the nucleon properties. Since the proton and neutron have no strangeness:

$$\int_0^1 [s(x) - \bar{s}(x)]\, dx = 0 \tag{2.22}$$

and from the proton and neutron charges:

$$\int_0^1 \left\{\frac{2}{3}[u(x) - \bar{u}(x)] - \frac{1}{3}[d(x) - \bar{d}(x)]\right\} dx = 1 \tag{2.23}$$

$$\int_0^1 \left\{\frac{2}{3}[d(x) - \bar{d}(x)] - \frac{1}{3}[u(x) - \bar{u}(x)]\right\} dx = 0 \tag{2.24}$$

which is equivalent to requiring:

$$\int_0^1 [u(x) - \bar{u}(x)]\, dx = 2 \tag{2.25}$$

$$\int_0^1 [d(x) - \bar{d}(x)]\, dx = 1 \tag{2.26}$$

In the Quark Parton Model (QPM), the nucleons contain three 'valence' quarks (uud for the proton and udd for the neutron) and many 'sea' quarks, $q\bar{q}$ pairs created virtually. Thus, in a nucleon the u and d quark contributions are parameterized by the sum of valence and sea contributions, while the antiquark and strange quark distributions only have contributions from the sea.

Other sum rules can be constructed using the results from various lepton-nucleon DIS experiments [4] and in this way information about the parton densities is extracted.

2.4 Evidence for Gluons in the Proton

The momentum sum rule states that:

$$\int_0^1 x\left\{u(x)+\bar{u}(x)+d(x)+\bar{d}(x)+s(x)+\bar{s}(x)\right\}dx = 1-\epsilon \tag{2.27}$$

where $\epsilon = 0$ if the proton only contains quarks.

From 2.20 and 2.21 and assuming that strange quarks carry only a small fraction of the nucleon's momentum:

$$\int_0^1 F_2^{ep}(x)\,dx = \frac{4}{9}\int_0^1 x\left\{u(x)+\bar{u}(x)\right\}dx + \frac{1}{9}\int_0^1 x\left\{d(x)+\bar{d}(x)\right\}dx \tag{2.28}$$

$$\int_0^1 F_2^{en}(x)\,dx = \frac{4}{9}\int_0^1 x\left\{d(x)+\bar{d}(x)\right\}dx + \frac{1}{9}\int_0^1 x\left\{u(x)+\bar{u}(x)\right\}dx \tag{2.29}$$

so:

$$\frac{9}{5}\int_0^1 \left\{F_2^{ep}(x)+F_2^{en}(x)\right\}dx = \int_0^1 U(x)\,dx + \int_0^1 D(x)\,dx \tag{2.30}$$

where $U(x) = u(x)+\bar{u}(x)$ and $D(x) = d(x)+\bar{d}(x)$. Using 2.27 therefore:

$$\epsilon \approx 1 - \frac{9}{5}\int_0^1 \left\{F_2^{ep}(x)+F_2^{en}(x)\right\}dx \tag{2.31}$$

Measurements made at SLAC in the early 1970's [5] showed that $\epsilon \approx 0.46$. Therefore, about 50% of the proton's momentum cannot be accounted for by the quarks alone. This suggests the existence of other partons in the proton, which are electrically neutral as they do not interact with the exchanged photon; these are the gluons.

2.5 Evidence for Colour

Quarks exist in three colours, conventionally called red (r), green (g) and blue (b), and antiquarks carry anticolour. Originally the idea of a colour quantum number was introduced to explain the existence of the Δ^{++} which consists of three identical u quarks in a symmetric ground state, therefore violating the Pauli exclusion principle. If each of the three u quarks has a different colour, this is no longer the case. More recently, measurements of :

$$R = \frac{\sigma(e^+e^- \rightarrow \text{hadrons})}{\sigma(\mathrm{e^+e^-} \rightarrow \mu^+\mu^-)}$$

have provided further evidence for colour. In the simple quark parton model,

$$R = \sum_i e_i^2$$

where the summation is over all possible quark species. For the five quarks u, d, s, c, b, therefore, we expect R to have the value of $\frac{11}{9}$ but measurements [6] have shown that in fact $R = \frac{11}{3}$, which is consistent with each of the five quark species existing in three coloured varieties [1].

Introduction of the colour quantum number would seem to suggest many candidate states for each of the observed particles. For example, the proton could be $u_r u_g d_b$, $u_r u_g d_g$, $u_b u_r d_r$ and so on. However, only one proton state exists, so the theory asserts that all particle states observed in nature are colourless. Mesons ($q\bar{q}$ states) are comprised of a quark of one colour and an anti-quark of the corresponding anti-colour and baryons (qqq or $\bar{q}\bar{q}\bar{q}$ states) contain one quark of each colour.

The colour charge is responsible for the strong interaction between quarks, and the gauge theory of this interaction is Quantum Chromodynamics (QCD). The quark-quark interactions are mediated by gluons, bosons which are believed to be massless. Gluons are bicoloured and exist in eight colour states:

$$r\bar{b}, r\bar{g}, b\bar{g}, b\bar{r}, g\bar{b}, g\bar{r} \frac{r\bar{r} - b\bar{b}}{\sqrt{2}}, \frac{r\bar{r} + b\bar{b} - 2g\bar{g}}{\sqrt{6}}$$

As gluons carry colour, gluon-gluon interactions are also possible.

2.6 Quantum Chromodynamics

The parton model described in the previous section ignores the presence of gluons within the proton. According to QCD, quarks can radiate gluons, with a probability characterized by the strong coupling constant $\alpha_s(Q^2)$, and gluons can split into $q\bar{q}$ pairs. Thus we must also consider interactions of the form $\gamma^* q \rightarrow qg$ (QCD Compton) and $\gamma^* g \rightarrow q\bar{q}$ (Boson-Gluon Fusion, or BGF) which give $O(\alpha\alpha_s)$ contributions to the cross-section, in addition to the $O(\alpha)$ term predicted by the QPM. The Feynman diagrams for these processes are shown in figure 2.2. Of

[1] Higher order corrections to the free parton model and effects due to the Z^0 mean that R is not exactly $\frac{11}{3}$.

course QCD predicts further, higher order corrections to the DIS cross-section but we will consider only the three processes shown in figure 2.2.

Adding the process $\gamma^* q \rightarrow qg$ to the parton model cross-section modifies 2.18 to the following [7]:

$$\frac{F_2(x,Q^2)}{x} = \sum_q e_q^2 \int_x^1 \frac{d\xi}{\xi} q(\xi) \left\{ \delta\left(1-\frac{x}{\xi}\right) + \frac{\alpha_s}{2\pi} P_{qq}\left(\frac{x}{\xi}\right) \log\left(\frac{Q^2}{\mu^2}\right) \right\} \tag{2.32}$$

where the fraction of the proton's momentum carried by the gluon is $(\xi - x)$ with ξ having any value from x to 1 (see figure 2.3). The presence of the $\log Q^2$ factor means that the parton model scaling prediction is violated, and F_2 is now a function of x and Q^2. This has been observed experimentally [8].

The splitting function P_{qq} is the probability that a quark, having radiated a gluon, is left with a fraction z $(= x/\xi)$ of it original momentum:

$$P_{qq}(z) = \frac{4}{3}\left(\frac{1+z^2}{1-z}\right) \tag{2.33}$$

P_{qq} has a singularity as $z \rightarrow 1$, called the 'soft' divergence as it is associated with the emission of a gluon with negligible momentum. It is cancelled by including the virtual diagrams shown in figure 2.4 in the cross-section. The parameter μ is introduced in 2.32 to regularize a second divergence, which arises when the quark emits a gluon collinear with itself (the 'collinear' divergence).

We can write 2.32 in terms of a modified parton density:

$$\begin{aligned} \frac{F_2(x,Q^2)}{x} &= \sum_q e_q^2 \int_x^1 \frac{d\xi}{\xi} [q(\xi) + \Delta q(\xi)] \delta\left(1-\frac{x}{\xi}\right) \\ &= \sum_q e_q^2 [q(x) + \Delta q(x,Q^2)] \end{aligned}$$

where:

$$\Delta q(x,Q^2) = \frac{\alpha_s}{2\pi} \log\frac{Q^2}{\mu^2} \int_x^1 \frac{d\xi}{\xi} P_{qq}\left(\frac{x}{\xi}\right) \tag{2.34}$$

It now has the same form as 2.18, but the quark density depends on both x and Q^2. We can interpret this as follows. At some value of the resolving power Q^2, say Q_0^2, the photon 'sees' just the valence quarks in the proton. If the quarks did not interact, as Q^2 increased, no further structure would be resolved and 'scaling', as predicted by the parton model, would be observed. In QCD this is not the case. The photon is able to resolve more of the constituents of the proton as Q^2

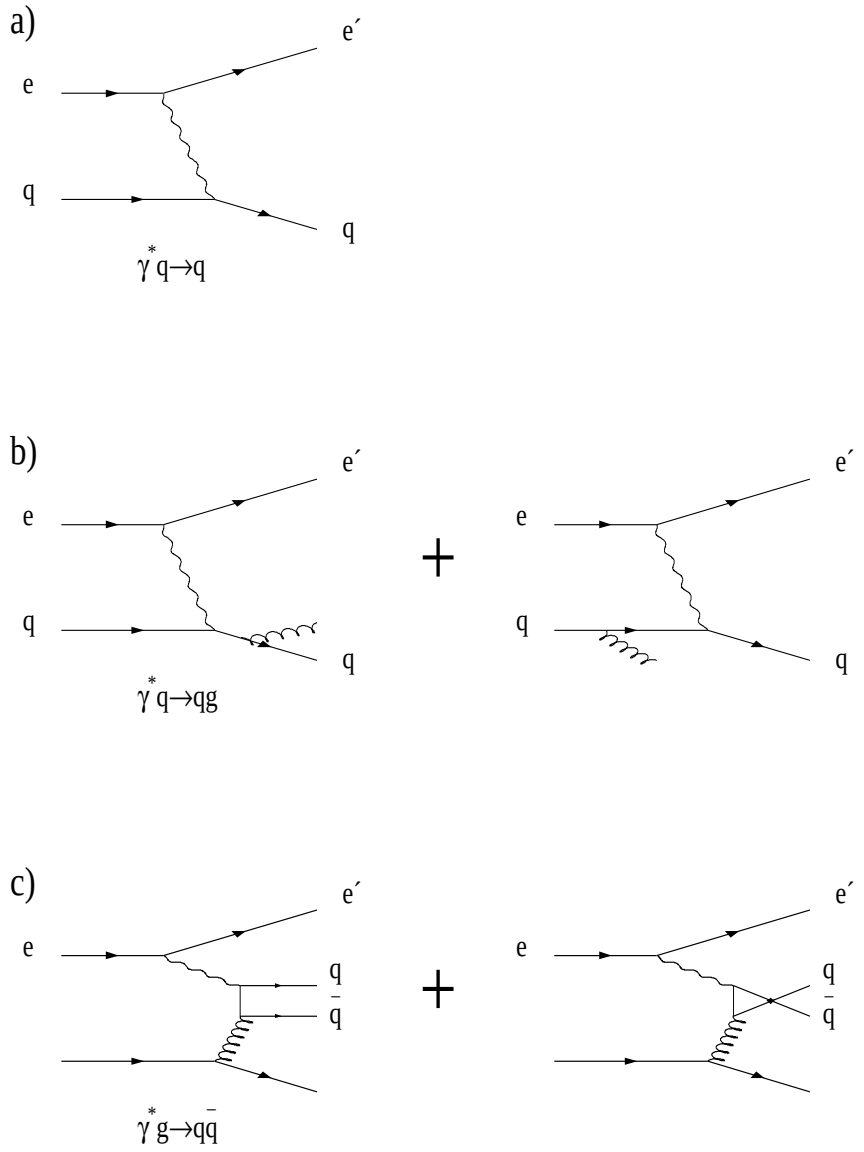

Figure 2.2: Feynman diagrams for the three $O(\alpha_s)$ processes in NC DIS: a) QPM; b) QCD Compton and c) BGF

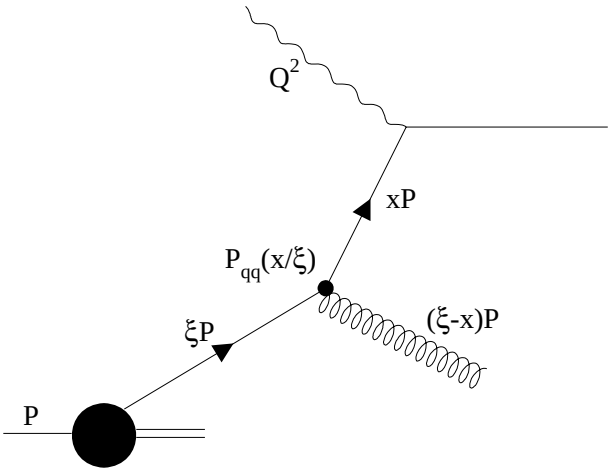

Figure 2.3: The QCD Compton process, $\gamma^* q \rightarrow qg$. The splitting function $P_{qq}(z)$ is the probability that a quark has a fraction z of its original momentum after radiating a gluon.

increases, and so the quark density itself must be a function of Q^2 as well as of x. Figure 2.5 shows schematically what happens as Q^2 increases.

The way in which the parton density evolves with Q^2 can be determined from equation 2.34. By considering the variation in the quark density with a small change in $\log Q^2$, 2.34 can be rewritten as:

$$\frac{dq(x,Q^2)}{d\log Q^2} = \frac{\alpha_s}{2\pi}\int_x^1 \frac{d\xi}{\xi} q(\xi,Q^2) P_{qq}\left(\frac{x}{\xi}\right) \tag{2.35}$$

This is an Altarelli–Parisi evolution equation [2] [9] and expresses the fact that a quark with momentum fraction x could have come from a quark with momentum fraction ξ which radiated a gluon.

However, as we stated before, we must also include a contribution to F_2 from

[2]This method of evolving parton density distributions is sometimes also referred to as DGLAP evolution after Dokshitzer, Gribov, Lipatov, Altarelli and Parisi

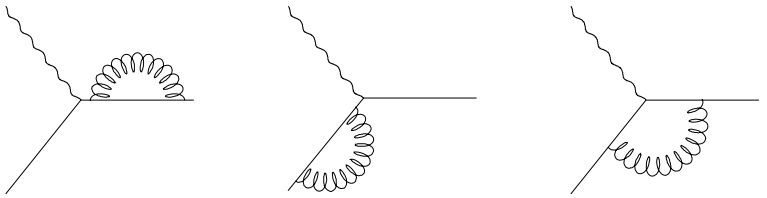

Figure 2.4: The virtual diagrams which must be included in the cross-section to cancel the 'soft' divergence.

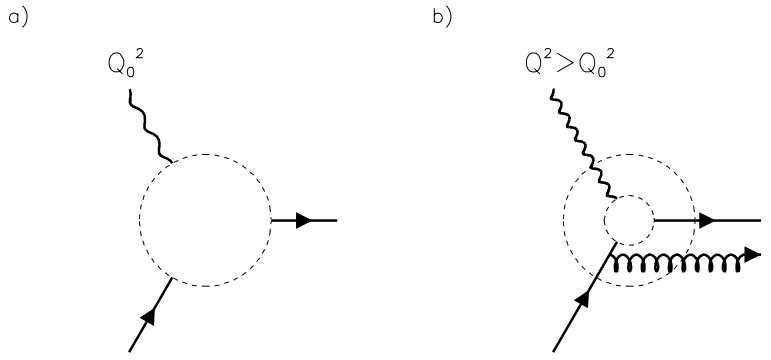

Figure 2.5: A schematic diagram showing how the structure of the proton as seen by the virtual photon changes as Q^2 increases. At some value of the resolving power Q^2, say Q_0^2, the photon 'sees' only the valence quarks inside the proton (a). As Q^2 increases, and correspondingly the wavelength of the photon probe decreases, additional structure can be resolved (b).

BGF, $\gamma^* g \to q\bar{q}$:

$$\frac{F_2(x,Q^2)}{x}|_{\gamma^* g \to q\bar{q}} = \sum_q e_q^2 \int_x^1 \frac{d\xi}{\xi} g(\xi) \frac{\alpha_s}{2\pi} P_{qg}\left(\frac{x}{\xi}\right) \log\left(\frac{Q^2}{\mu^2}\right) \tag{2.36}$$

where $g(\xi)$ is the gluon density in the proton and :

$$P_{qg}(z) = \frac{1}{2}\left\{z^2 + (1-z)^2\right\} \tag{2.37}$$

is the probability that a gluon splits into a $q\bar{q}$ pair such that the quark has a fraction z of its momentum. Hence 2.35 becomes:

$$\frac{dq_i(x,Q^2)}{d\log Q^2} = \frac{\alpha_s}{2\pi}\int_x^1 \frac{d\xi}{\xi}\left\{q_i(\xi,Q^2)P_{qq}\left(\frac{x}{\xi}\right) + g(\xi,Q^2)P_{qg}\left(\frac{x}{\xi}\right)\right\} \tag{2.38}$$

for each quark flavour, i. The possibility that a quark could have come from a gluon is now included.

We can also derive an equation for the evolution of the gluon density:

$$\frac{dg(x,Q^2)}{d\log Q^2} = \frac{\alpha_s}{2\pi}\int_x^1 \frac{dy}{y}\left\{\sum_i q_i(y,Q^2)P_{gq}\left(\frac{x}{y}\right) + g(y,Q^2)P_{gg}\left(\frac{x}{y}\right)\right\} \tag{2.39}$$

where $i = 1,\ldots,2n_f$ where n_f is the number of quark flavours and P_{gq} and P_{gg} are the splitting functions for a gluon being radiated from a quark and for a gluon radiated from another gluon respectively:

$$\begin{aligned} P_{gq} &= \frac{4}{3}\left\{\frac{1+(1-z)^2}{z}\right\} \\ P_{gg} &= 6\left\{\frac{1-z}{z} + \frac{z}{1-z} + z(1-z)\right\} \end{aligned}$$

Using these equations, a parton density measured at a particular value of Q^2, say Q_0^2, can be evolved to a higher value of Q^2.

In this section, we have only considered the first order QCD corrections to the simple quark parton model. Higher order corrections will lead to additional terms in the Altarelli-Parisi evolution equations and further modify the parton density functions.

Figure 2.6 shows a schematic view of DIS. The parton which interacts with the virtual photon is at the top of a ladder of parton emissions, at the other end of which is the parton from the proton. The phase space for emissions along this ladder depends on the difference between x_1 and x. By taking moments of

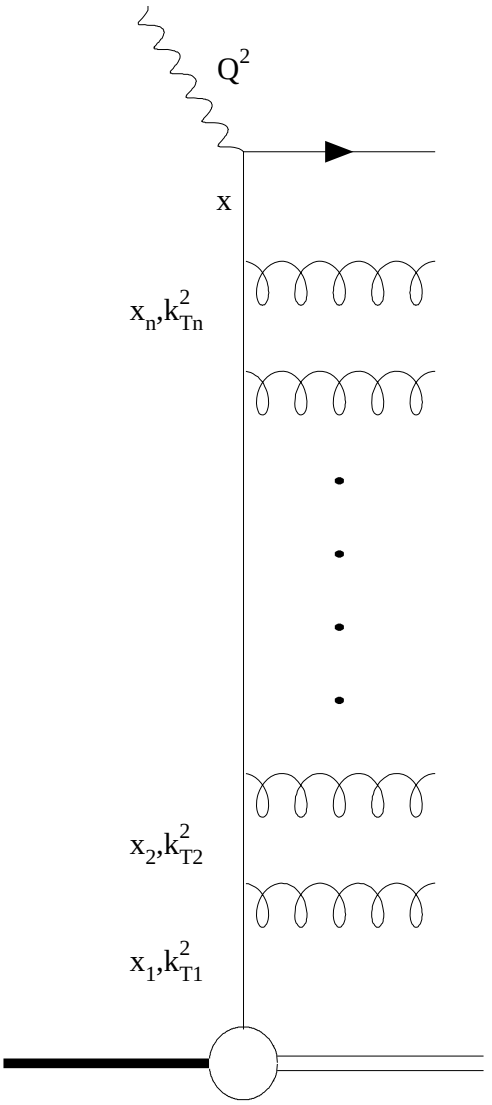

Figure 2.6: Schematic diagram showing a ladder of parton emissions. Although the space-like partons in this diagram are all quarks, they could be gluons, which may subsequently lead to time-like quarks as rungs of the ladder.

equations 2.38 and 2.39, it can be shown that the leading $\log Q^2$ term corresponds to a ladder in which the virtualities of the partons are strongly ordered in k_T:

$$k_{T1}^2 \ll k_{T2}^2 \ldots\ldots \ll k_{Tn}^2 \ll \ldots\ldots \ll Q^2$$

However, at low x it might be expected that the gluonic terms in the evolution equations dominate. In this approximation, $P_{gg} \approx 6/z$ and:

$$\frac{dxg(x,Q^2)}{d\log Q^2} = \frac{3\alpha_s}{\pi}\int_x^1 \frac{d\xi}{\xi} g(\xi, Q^2) \tag{2.40}$$

This is known as the Double Leading Log Approximation (DLLA) and gives rise to terms of order $\alpha_s \log\frac{1}{x}\log Q^2$ which become significant at low x and high Q^2. The DLLA is equivalent to summing ladders in which the partons are strongly ordered in both tranverse and longitudinal momenta:

$$\begin{aligned} k_{T1}^2 &\ll k_{T2}^2 \ldots\ldots \ll k_{Tn}^2 \ll \ldots\ldots \ll Q^2 \\ x_1 &\gg x_2 \ldots\ldots \gg x_n \gg \ldots\ldots \gg x \end{aligned}$$

However, this only includes the leading term in $\log Q^2$ with the leading term in $\log\frac{1}{x}$. For finite Q^2 at low x we want to sum the leading $\log\frac{1}{x}$ terms whilst keeping the full Q^2 dependence. This requires the relaxation of the strong ordering in k_T and using the unintegrated gluon distribution $f(x,k_T^2)$ where:

$$xg(x,Q^2) = \int_0^{Q^2} \frac{dk_T^2}{k_T^2} f(x,k_T^2) \tag{2.41}$$

and $f(x,k_T^2)$ satisfies the BFKL equation [10]. By solving the BFKL equation analytically at fixed α_s, the form of $f(x,k_T^2)$ is found to be:

$$f(x,k_T^2) \sim x^{-\lambda} \tag{2.42}$$

where $\lambda \sim 0.5$. Thus from equation 2.41, the x dependence of the gluon density is predicted to be $xg(x,Q^2) \sim x^{-0.5}$.

2.7 Parton Distribution Functions

As can be seen from the above dicussion, theoretical calculations of the structure functions and of the cross-sections for DIS processes requires a knowledge of the parton density functions. These must be extracted from experimental data.

The parton distribution functions used in the Monte Carlo used in this thesis are the MRSH set, obtained by Martin, Roberts and Stirling [11]. The parton density distributions are parameterized at a fixed Q_0^2, chosen to be 4 GeV^2 which is large enough for perturbative calculations to be valid. The parameterizations are then evolved using the the next-to-leading-order Altarelli-Parisi equations to higher values of Q^2, where comparisons can be made with experimental data. The unknown parameters in the parton density functions are obtained by performing a global fit to data from many different experiments (various lepton-nucleon deep inelastic scattering experiments and nucleon-nucleon scattering experiments). In the MRSH set of parton density functions, the gluon density is motivated by the solution to the BFKL equation and has the form $xg(x,Q^2) \sim x^{-0.3}$. It is also assumed that the gluon density drives the sea quark density, and the two have the same functional form. The 1992 HERA F_2 measurements are included in the global fit to extract the parton density functions.

Figure 2.7 shows the MRSH parton density distributions for $Q^2 = 20$ GeV^2 and $Q^2 = 50$ GeV^2.

2.8 The LEPTO Monte Carlo

Deep inelastic scattering experiments aim to relate the experimental observation of hadrons in a complex array of detectors to the interaction which occured between the exchanged boson and a parton within the nucleon. This requires knowledge of the detector performance and an understanding of hadronization. In practice, our theoretical understanding, the results from previous experiments and a model for hadronization is implemented in a computer program, a Monte Carlo generator. Using this in conjunction with a detector simulation program, direct comparisons can be made with the data. Each Monte Carlo implements the theory in a different way, and makes different assumptions. The Monte Carlo used throughout this thesis is LEPTO 6.1 [12]. It is based on a description of DIS as the interaction of a virtual boson with the partonic content of the proton (a so-called 'standard' DIS Monte Carlo).

LEPTO uses the leading order electroweak cross-section and calculates the cross-sections for the two $O(\alpha_s)$ processes (QCD Compton and BGF) from the exact first order matrix elements. As has been observed previously, however, the

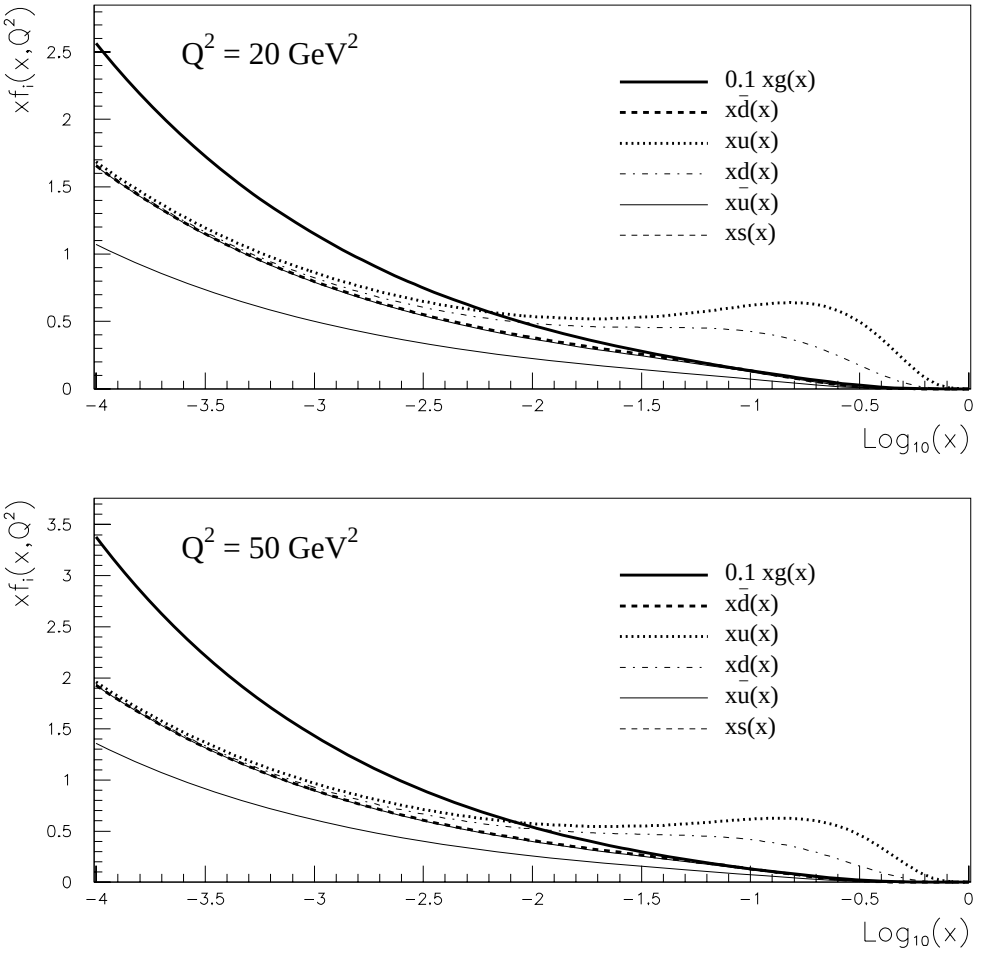

Figure 2.7: The MRSH parton densities at $Q^2 = 20\ GeV^2$ and $Q^2 = 50\ GeV^2$. Note the scale change for the gluon densities in both cases.

matrix elements are divergent, and for Monte Carlo generation this requires the implementation of a cut-off. The details of this cut-off will be explained in section 7.2.

The parton shower approach is used to simulate higher orders in α_s, although only in the leading-log approximation. The incoming and the outgoing partons emit cascades of partons, based on the basic branchings $q \rightarrow qg$, $g \rightarrow gg$ and $g \rightarrow q\bar{q}$ as described by the Altarelli-Parisi equations in the leading log approximation. There are, however, limitations to this model. The initial and final state parton showers are treated separately, thus neglecting the possibility of interference between them. The use of the leading log approximation means that although the emission of partons which are soft or close to the direction of the emitting parton is well described, the emission of hard partons at a large angle is not. To overcome this problem in LEPTO 6.1, the first order matrix element is used to generate the hard emission, and extra, softer emissions are added using parton showers.

Hadronization is performed using the Lund string model as implemented in the program JETSET [13].

Chapter 3

The H1 Detector

3.1 HERA

The Hadron Electron Ring Anlage (HERA), situated at DESY in Hamburg, is designed to collide 820 GeV protons with 30 GeV electrons (or positrons), thus achieving a centre of mass collision energy of 314 GeV.

The electrons and protons are accelerated independently and stored in separate rings [14]. They are then injected into the HERA ring and brought together with a zero degree crossing angle, at four equidistant points, every 96 ns. The layout of HERA and the necessary pre-accelerators can be seen in figure 3.1. The H1 experiment is situated in the North Experimental Hall.

In the 1993 data taking period, the electron beam energy was 26.7 GeV. The HERA machine operated with 94 electron bunches and 90 proton bunches, 84 of which were colliding, compared with the design specifications of 210 proton and 210 electron bunches. The non-colliding bunches can be used for background studies.

The integrated luminosity delivered by the HERA machine in 1993 was 1 pb^{-1}. When operating at design specifications, an integrated luminosity of 10^5 nb^{-1} per year can be achieved (a luminosity of 1.5×10^{31} $cm^{-2}s^{-1}$).

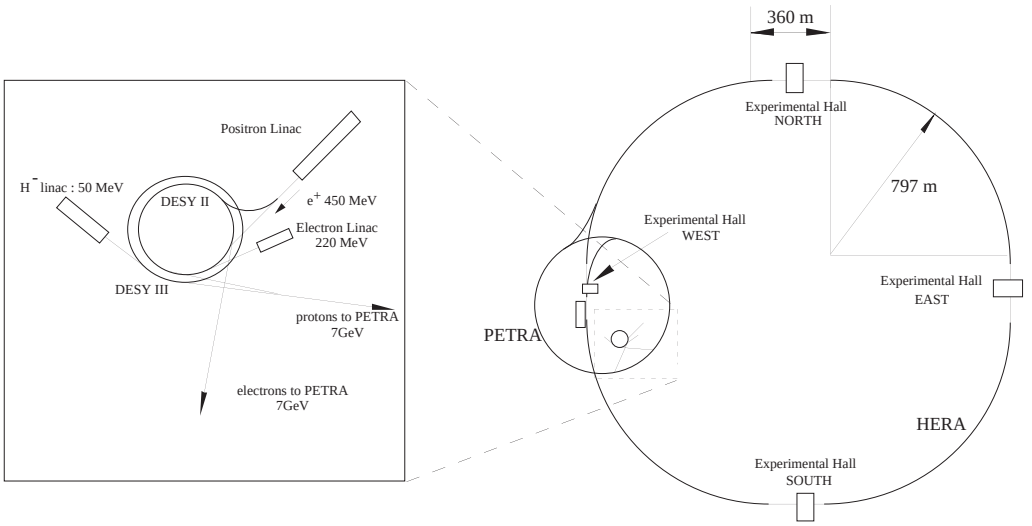

Figure 3.1: The layout of HERA and the pre-accelerators

3.2 The H1 Coordinate system

A standard coordinate system is used to describe both the H1 detector and the particle trajectories. The orientation of this co-ordinate system is illustrated in figure 3.2.

The origin is the nominal interaction point. The Cartesian coordinates (x, y, z) form a right handed set with the positive z axis defined by the incident proton beam and the positive y axis pointing vertically upwards. The cylindrical co-ordinates (θ, ϕ, z) are also used, where z is defined as above and the polar angle θ is measured with respect to the direction of the incident proton beam. The x axis corresponds to $\phi = 0°$. The terms "forward" and "backward" are often used to define the regions of the detector with $\theta < 90°$ and $\theta > 90°$ respectively.

3.3 The H1 Detector

The H1 detector [15], shown in figure 3.3, consists of tracking chambers,

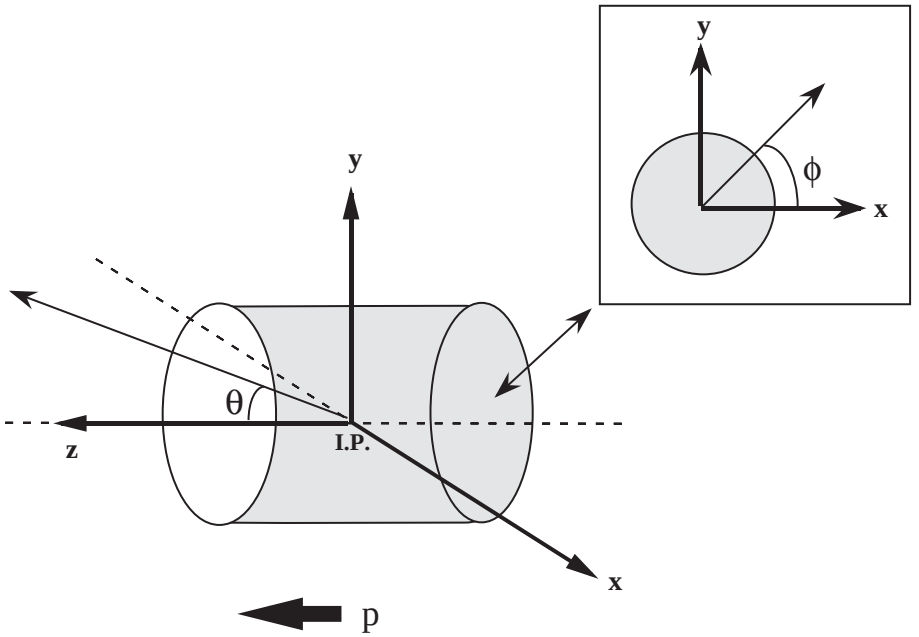

Figure 3.2: The H1 Coordinate system

calorimeters, scintillators and muon detectors. It provides complete angular coverage of the interaction region, so only particles within the beam pipe itself will remain undetected. The density of particles is highest in the forward (proton) direction, due to the large difference in the energies of the proton and electron beams. Hence the detector is asymmetric, with additional tracking, calorimetry and muon detectors in the forward direction.

In DIS experiments, the identification and accurate energy measurement of the scattered electron is very important. In addition, a hermetic calorimeter is needed for studies of the hadronic final state and for the detection of neutrinos in charged current physics by the measurement of the 'missing' transverse momentum in an event. In H1, the Liquid Argon Calorimeter serves the dual purpose of hadron detection and, at high Q^2 (above about 100 GeV^2), the detection of the scattered electron. At low Q^2 (less than 100 GeV^2) the electron is scattered into the Backward Electromagnetic Calorimeter.

The reconstruction of charged particles requires accurate and efficient tracking detectors in a uniform magnetic field. In H1, the large cylindrical superconducting coil surrounding the Liquid Argon Calorimeter provides a uniform magnetic field

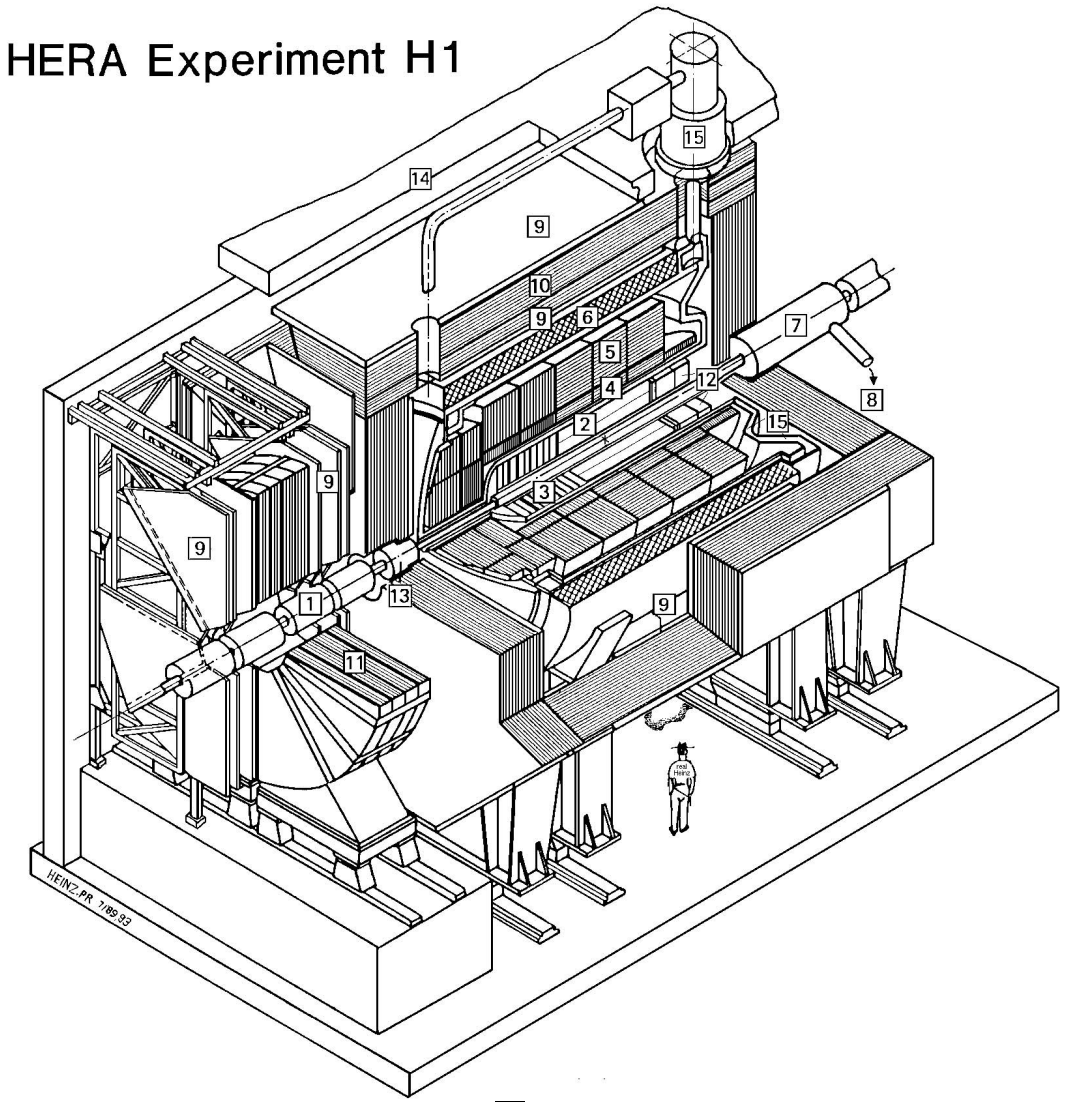

1. Beam pipe and beam magnets
2. Central track detector
3. Forward track detector
4. Electromagnetic calorimeter
5. Hadronic calorimeter
6. Super conducting coil ($1.15T$)
7. Compensating magnet
8. Helium cryogenics
9. Muon chambers
10. Instrumented iron
11. Forward muon toroid magnet
12. Backward electromagnetic calorimeter
13. Plug calorimeter
14. Concrete shielding
15. Liquid argon cryostat

Figure 3.3: A 3-dimensional view of the H1 detector

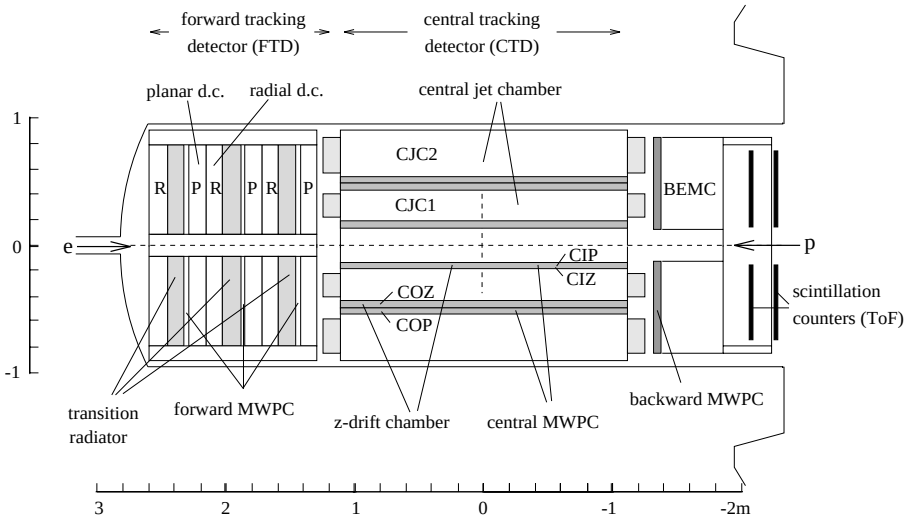

Figure 3.4: An r-z view of the H1 tracking system

which deviates at most by only 4.5% from its nominal value of 1.15T [15].

Muon identification is vital in the search for exotic particles and the study of heavy quark production. H1 contains muon detectors in the iron return yoke of the magnet and an additional muon spectrometer in the forward region.

The short bunch crossing interval of 96 ns and the high background rate necessitates the implementation of a sophisticated trigger system and methods of background rejection. The scintillator systems installed behind the H1 detector (not shown in figure 3.3) are used in the selection of genuine *ep* interactions.

Finally, an accurate luminosity measurement is needed for cross-section measurements.

3.4 Tracking

The tracking detectors in H1 are divided into three sections; the Central Tracking Detector (CTD), the Forward Tracking Detector (FTD) and the Backward Proportional Chamber (BPC). They are designed to provide accurate charged particle reconstruction ($\sigma_p/p^2 \approx 3 \times 10^{-3} GeV^{-1}$ and $\sigma_\theta \approx 1$ mrad), particle identification and triggering in a high multiplicity environment. A combination of drift chambers and proportional chambers are used to achieve this.

An $r-z$ view of the H1 tracking system is shown in figure 3.4.

Drift Chambers

A drift chamber is typically sub-divided into cells, each of which contains anode ("sense") wires and a cathode, and is gas-filled. A uniform electric field is maintained across each cell.

When a charged particle traverses the chamber, atoms of the gas are ionized. The now free electrons drift towards the anode wires, and the positive ions drift towards the cathode. As the electrons approach the sense wires (at a distance of about a wire diameter from the wire itself), the field strength increases rapidly. They are accelerated and more gas atoms are ionized, thus producing an avalanche of electrons, which subsequently deposit charge on the sense wires.

The time taken for the electrons to drift to the sense wires is directly related to the distance between the ionizing particle and the wire. In addition, the mean charge deposited on the sense wires is a well-known function of the particles mass and momentum, a fact which can be exploited for particle identification (dE/dx).

If the sense wires are made of a resistive material, it is possible to use the charge division method to determine the point along the wire at which the ionization was collected. This involves comparing the charge measured at the two ends of the wire. The typical resolution of such a method is $\approx 1\%$ of the wire length, compared to a resolution in the drift co-ordinate of 150–200 μm.

For a chamber with drift cells which are symmetric about the line of sense wires there is no way of determining the direction in which the electrons drifted. However, this ambiguity can be resolved by staggering the sense wires alternately left and right about their mid-plane position. This ensures that the relative time taken for the signal to reach two adjacent wires depends on the sign of the drift velocity.

Proportional Chambers

In a proportional chamber, the sense wires are very close together. Any particle traversing the chamber must pass close to an anode, the region in which multiplication (the production of an avalanche of electrons) occurs. Consequently, the signal is received very quickly (a few tens of nanoseconds) after the particle entered the chamber, making proportional chambers ideal for triggering. Either the anode wires or the cathode pads can be read out, although in the latter case the position resolution of the chamber will be poor.

3.4.1 Central Trackers

The tracking detectors in the central region cover the range $25° < \theta < 155°$. Moving radially outward from the interaction point, a particle encounters the inner proportional chamber (CIP), the inner z chamber (CIZ), the inner jet chamber (CJC1), the outer z chamber (COZ), the outer proportional chamber (COP) and the outer jet chamber (CJC2). Figure 3.5 shows a section through the CTD.

The main components of the CTD are the two large drift chambers, CJC1 and CJC2. The sense wires in both of these chambers are strung parallel to the beam axis. CJC1 is divided into 30 cells in ϕ, with 24 sense wires per cell, whereas CJC2 has 60 cells in ϕ with 32 sense wires in each. The actual positions of the sense wires are staggered by $\pm$ 150 μm from the nominal sense wire plane. Both ends of the sense wires are read out, thus enabling the z co-ordinate to be determined by charge division. In addition, the drift cells are tilted 30° from the radial axis, as is clearly visible in figure 3.5. This means that in the presence of a magnetic field the electrons drift almost perpendicular to stiff, high momentum tracks from the interaction region, thus achieving optimum track resolution. Also, the ambiguity in the sign of the drift can be resolved by linking track segments from adjacent cells and as most tracks cross the sense wire plane at least once in both CJC1 and CJC2, accurate timing information is available.

Tracks from the jet chambers can be used in the reconstruction of the event vertex. The measurement of dE/dx (resolution $\sim 12\%$) can also used for particle identification.

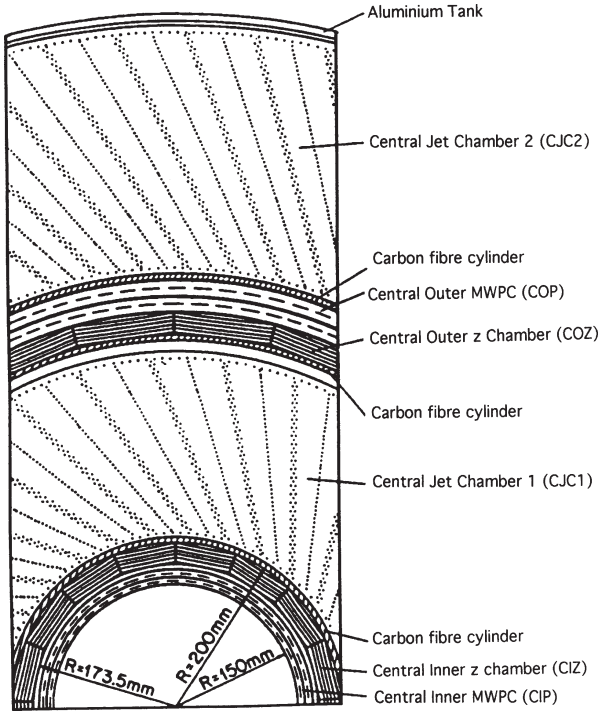

Figure 3.5: A cross-section through the CTD

The two thin drift chambers (CIZ and COZ) which surround the inner jet chamber are designed to improve the z resolution of tracks in the CTD, as in both these chambers, the electrons drift in the z direction. They consist of drift cells which form rings around the beam pipe. Each ring has four sense wires at the same z co-ordinate but different radii. The CIZ consists of 15 drift cells, each of which is a 16-sided polygon in cross-section, and the COZ is composed of 24 cells, each in the form of a 24-sided polygon.

Track elements from the two z chambers typically have a resolution of 300 μm in z. ϕ is determined from charge division, with a resolution of 1–2%.

The two central proportional chambers (CIP and COP) are designed to trigger on tracks from the interaction region. Each consists of two concentric cylindrical chambers with anode wires parallel to the beam axis but only the cathode pads are read out. For the CIP, the pads are 36.6 mm long in z and cover 45° in ϕ. The pads in the two layers are offset by half a cell in ϕ to halve the effective resolution. For the COP, the pads are 120 mm long in z and cover 22.5° in ϕ.

3.4.2 Forward Trackers

The FTD consists of three identical supermodules and is designed to detect charged particles in the range $5° < \theta < 30°$. Each supermodule contains (moving forward in z) a planar wire drift chamber, a multiwire proportional chamber (FMWPC), a transition radiator module and a radial wire drift chamber.

Each planar chamber consists of three planes of wires strung perpendicular to the beam axis. Each plane is four wires deep in z, and is rotated with respect to the next by 60° in ϕ. By combining information from the three planes, an accurate x-y co-ordinate can be reconstructed.

The three FMWPC's are used for triggering. Each chamber contains two planes of anode wires, which are not read out, and two cathode planes with pad readout. The radial size of the pads varies from 18 mm at the inner radius of the chamber to 32 mm at the outer radius. The pads all cover 45° in ϕ, except the four outermost ones which each cover 22.5°. In addition, the pads are offset by half a pad radius to improve the effective resolution.

The radial chambers are divided into 48 wedge shaped drift cells in ϕ. There are 12 sense wires per wedge, strung radially and connected between wedges at 105° in ϕ. The wires are staggered by 287 μm each side of a plane bisecting the wedge to resolve the ambiguity in the sign of the drift velocity.

The radial chambers can also be used for particle identification, using either dE/dx, or transition radiation (TR).

When a relativistic particle travels from one dielectric medium to another, it may emit an X-ray photon (transition radiation). The probability that it does so is small, however, and requires that the ratio of the momentum of the particle

to its mass is large. This means that TR can be used to identify electrons below about 80 GeV, as they are the only particles which produce TR photons in this momentum range.

To improve the efficiency for the production of TR photons, the transition radiator module in the FTD contains 400 polypropylene foils, thus providing many interfaces between materials of different dielectric constants. If the transition radiator module is filled with a gas which is transparent to the TR photons, they will enter the radial chambers, through an x-ray transparent Mylar window. In addition if the radial chambers contain a gas with a high capture cross-section for TR photons (a Xenon gas mixture), they can be detected as an excess of charge on the first sense wire of the chamber.

3.4.3 Backward Proportional Chamber

The BPC is a circular Multiwire Proportional Chamber, situated in front of the Backward Electromagnetic Calorimeter (BEMC). It is designed both for triggering, and to give an accurate space point for particles moving in the backward direction ($155° < \theta < 174.5°$). Hence the anode wires, as opposed to the cathode pads, are read out.

The chamber consists of four planes of wires, orientated at 45° with respect to each other. A coincidence of hits on three out of the four wire planes is sufficient to define a space point.

A track reconstructed using a space point in the BPC and the event vertex has an angular resolution of approximately 0.5 mrad [15].

3.5 Calorimetry

A sampling calorimeter consists of two parts; a material which causes an incident particle to shower (the absorber) and a sensitive medium to measure the development of the shower. However, the details of the calorimetry are different for the detection of hadronic and electromagnetic particles.

When high energy electrons and photons interact with an absorber, more elec-

trons and photons are produced by bremsstrahlung and pair production. Subsequently further interactions take place, and the result is a shower of particles. The size of the shower depends of the radiation length of the material it traverses (X_0), defined as the distance over which the mean energy of an electron is reduced by a factor e. In time, all the energy of the incident particle is lost through ionization. By ensuring that the shower is fully contained and by measuring the total ionization, the energy of the incident particle can be determined.

In contrast, hadrons incident on a material lose most of their energy in inelastic nuclear collisions. The resulting particles may then undergo further interactions, thus producing a shower of particles. The dimension of such a shower depends on the nuclear absorption length (λ_I) of the material. In general, $X_0 \ll \lambda_I$. However, there are two specific features which limit the energy resolution of hadronic calorimeters:

1. Many of the particles produced in these collisions are π^0's, which decay electromagnetically, without any further nuclear interactions. The statistical fluctuations in the number of π^0's will lead to fluctuations in the visible energy of a hadronic shower.

2. A sizable ($\approx 30\%$) amount of the available energy is used in the excitation or break up of nuclei, resulting in the production of very low energy photons which cannot be detected. This means that most calorimeters have a better response for electromagnetic particles than for hadronic particles of the same energy (so called non-compensating calorimeters).

The energy resolution of a calorimeter is governed by the statistical fluctuations in the number of particles (N) in the shower:

$$\frac{\sigma}{E} \approx \frac{1}{\sqrt{N}} \approx \frac{1}{\sqrt{E}}$$

. In practice, other factors such as noise and energy leakage will degrade this resolution further.

Figure 3.6 shows the position of the calorimeters in the H1 detector. There are four separate calorimeters; the Liquid Argon Calorimeter, the Backward Electromagnetic Calorimeter, the Tail Catcher and the Plug Calorimeter.

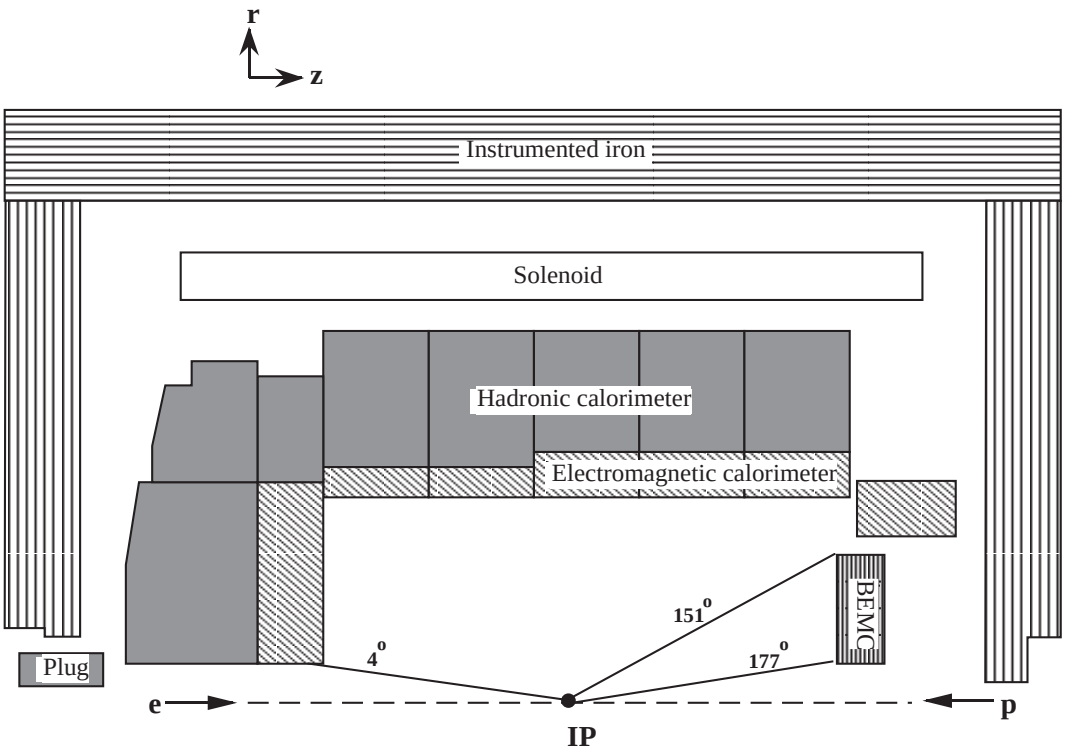

Figure 3.6: An r-z view of the H1 Calorimeters

3.5.1 Liquid Argon Calorimeter

The H1 Liquid Argon Calorimeter [16] measures energy deposited between $\theta = 4°$ and $\theta = 153°$. It consists of an electromagnetic section (the EMC) and a hadronic section (the HAC) enclosed in a single cryostat. It is a non-compensating calorimeter, so the visible energy ('response') for electromagnetic particles is higher than that for hadronic particles of the same energy. This means that the energy deposited in the calorimeter must be weighted differently in the two cases.

The EMC uses 2.4 mm thick lead plates as the absorber, each separated from the next by a gap of 35 mm. The volume between the plates is filled with liquid argon and contains a plane of readout pads from which the signals are taken. The total thickness of the EMC varies between 20 and 30 radiation lengths and the resolution is $\sigma_E/E \approx 12\%/\sqrt{E} \oplus 1\%$ (E in GeV).

The HAC consists of 19 mm thick stainless steel plates interleaved with two volumes of liquid argon, each 2.4 mm thick. The two volumes of active material are separated by a plane of readout pads. The depth of the HAC varies between $5\lambda_I$ and $7\lambda_I$, and the resolution is $\sigma_E/E \approx 50\%/\sqrt{E} \oplus 2\%$ (E in GeV).

Both the EMC and the HAC are highly segmented, into a total of approximately 45,000 cells. The fine granularity enables hadronic showers to be distinguished from electromagnetic showers by the shower profile and the energy reweighted accordingly [17]. In addition, isolated cells registering a significant energy deposition can be readily identified as noise.

There is an additional uncertainty in the absolute energy scale of the calorimeter. In 1993, this was $\approx 3\%$ for the EMC and $\approx 7\%$ for the HAC [20].

3.5.2 Backward Electromagnetic Calorimeter

The Backward Electromagnetic Calorimeter (BEMC)[18] is designed to measure the energy and direction of the scattered electron in low Q^2 ($Q^2 < 100\ GeV^2$) deep inelastic scattering events. It covers the range $151° < \theta < 177°$, so that there is a continuous transition between the BEMC and the Liquid Argon Calorimeter.

The BEMC is circular in cross-section and layered in z with alternately 2.5 mm of lead and 4 mm of plastic scintillator. In total, there are 50 layers of scintillator, and 49 layers of lead. Furthermore, the BEMC is divided into 88 stacks in the $x - y$ plane. Most of the stacks are squares of side 159 mm, but at the outer rim of the calorimeter the stacks are trapezoidal and 4 triangular stacks surround the beam pipe.

A cross-section through the BEMC is shown in figure 3.7.

Signals from wavelength shifters located at the sides of each stack are read out using photodiodes. The quadratic stacks have two pairs of 8 cm wide wavelength shifters on opposite sides of the stack. They cover the entire depth of the stack and the sharing of energy between them is used to calculate the centre of gravity of a cluster with a precision of about 13 mm [15]. A 16 cm long wavelength shifter is located on each of the other two sides of the stack, but these cover only the last 15 layers of lead and scintillator. They provide information on the shower depth.

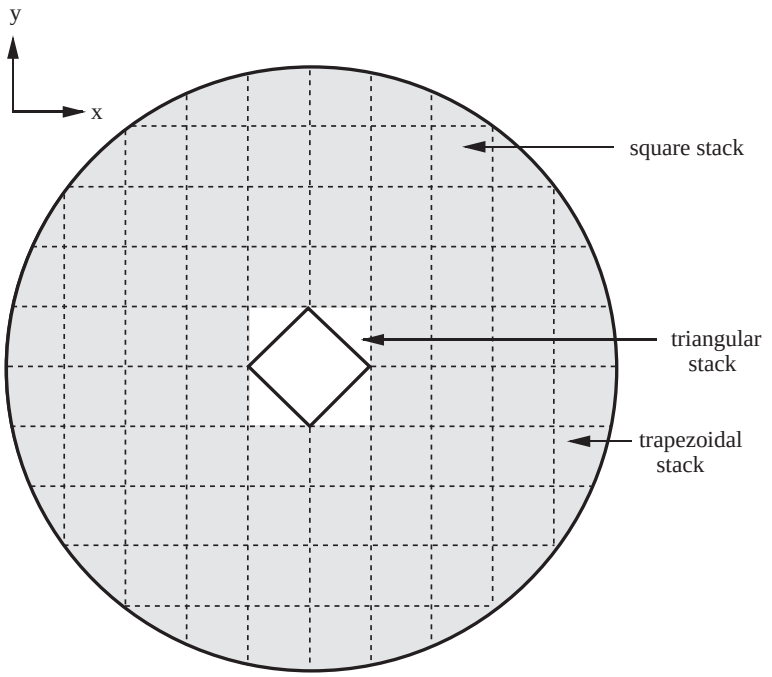

Figure 3.7: A cross-section of the BEMC

The triangular stacks contain wavelength shifters on the two shortest sides.

The BEMC has a depth of 22.5 X_0 and 0.97 λ_I. As a consequence of this, whilst electromagnetic showers are well contained, the hadronic response is poor. Hadrons typically deposit only 30% of their energy in the BEMC and 30% of all hadrons do not interact at all in the calorimeter [15].

The resolution of the BEMC is $\sigma_E/E \approx 10\%/\sqrt{E}$ (E in GeV) for electromagnetic particles and $\sigma_E/E \approx 80\%/\sqrt{E}$ for hadronic particles. There is an additional uncertainty of 2% in the absolute energy scale.

3.5.3 Plug Calorimeter

The plug calorimeter is designed to measure energy between the beam pipe ($\theta \approx 0.6°$) and the most forward part of the liquid argon calorimeter ($\theta \approx 3°$). It consists of nine layers of copper absorber interleaved with eight layers of silicon detectors.

The energy resolution of the plug calorimeter is $\sigma_E/E \approx 150\%/\sqrt{E}$ (E in GeV), but the device suffers from coarse sampling and has problems with shower containment.

The plug calorimeter was not used in any energy flow measurements presented in this thesis, owing to the present uncertainty in its energy scale.

3.5.4 Tail Catcher

Eleven of the sixteen layers of streamer tubes in the iron return yoke (used for muon detection; see section 3.6) are equipped with readout pads. These are then used to measure the energy of hadrons which are not fully contained in the liquid argon calorimeter and the BEMC.

The tail catcher has a depth of $\sim 4.5\lambda_I$ and a resolution of $\sigma_E/E \approx 100\%/\sqrt{E}$ (E in GeV),

3.6 Muon Detection

The return yoke of the magnet consists of 10 layers of iron interleaved with 16 layers of limited streamer tubes (LSTs). Each LST is 1 cm square in cross section, with a single wire running down its length. The gas gain is high, making signal amplification unnecessary. The signal is read either from the wires or from pads or strips on the covers of the tubes. The efficiency of the individual wires is $\sim 85\%$.

A muon having an energy greater than 1.2 GeV can reach the instrumented iron and may be detected there.

The Forward Muon Spectrometer is used to detect muons with 5 GeV $< E <$ 200 GeV in the range $3° < \theta < 17°$. It consists of three drift chambers either side of a toroidal magnet. Two of the chambers have sense wires strung radially and are used to measure the azimuthal angle of a track whereas the other four have sense wires strung around the beam axis and are used to measure the polar angle. The momentum resolution ($\Delta p/p$) of the Forward Muon Spectrometer is 24% at 5 GeV/c and deteriorates to 36% at 200 GeV/c.

3.7 Scintillators

There are two systems of scintillators installed upstream (in the incident proton direction) from the interaction region, which are designed to reject proton beam associated background.

The Time-of-Flight Counters

The Time of Flight device (ToF), situated at $z \approx$ -2 m, consists of two walls of plastic scintillator, perpendicular to the beam and covering an area approximately equal to that of the BEMC. The most forward of the two planes is divided into 16 counters and the other into eight counters. Each scintillator is sandwiched between 6.5 mm thick plates of lead which absorb the synchrotron radiation from the electron beam.

If, in a particular beam crossing, an ep interaction occurs, the ToF will register a signal from particles produced in the interaction about 13 ns after the proton bunch has entered the H1 detector. However if a proton from the bunch interacts with either the beam pipe or the residual gas therein, the resulting particles will reach the ToF before the proton and electron bunches cross. This enables the ToF to discriminate effectively between the two classes of events. Used in the level 1 (L1) trigger, the ToF leads to a 99% reduction in the overall trigger rate [15].

The Veto Walls

There are two further double scintillator systems, at $z \approx -6.5$ m (the Inner Veto Wall) and at $z \approx -8.1$ m (the Outer Veto Wall). The Outer Veto Wall covers an area of $5 \times 4\ m^2$ and has a timing resolution of $\sim$ 8 ns. The Inner Veto Wall extends only 1m from the beam pipe and has a timing resolution of $\sim$ 3 ns. Both work on the same principle as the ToF, and are used to identify background events.

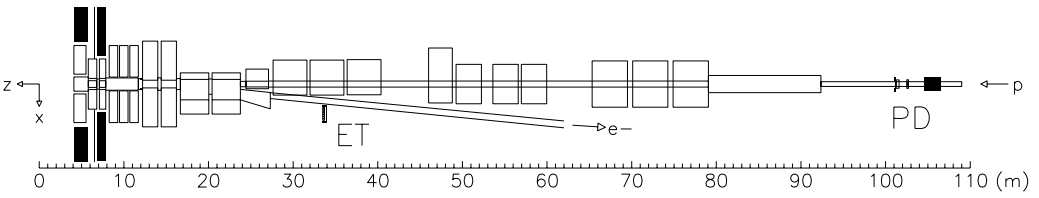

Figure 3.8: The H1 Luminosity system, showing the location of the electron tagger (ET) and the photon detector (PD).

3.8 The Luminosity System

The luminosity in H1 is calculated from the measured rate of the bremsstrahlung interaction $ep \rightarrow \gamma ep$, a process which has a large, well-known cross-section at low Q^2, when the structure of the proton is not resolved. The main source of background in this measurement is bremsstrahlung from the residual gas in the beam pipe, which has the same signature as the $ep \rightarrow \gamma ep$ events. The rate of these background events depends on the vacuum in the beam pipe and for the 1993 was about 10% of the $ep \rightarrow \gamma ep$ rate. It is measured using the electron "pilot" bunches (bunches of electrons with no corresponding proton bunch) and subsequently subtracted from the luminosity measurement.

The luminosity system detects electrons and photons in coincidence. As the angular distribution for electrons and photons produced in $ep \rightarrow \gamma ep$ events is strongly peaked in the direction of the incident electron beam, the detectors must be close to the beam pipe and far from the interaction point. The luminosity system, shown in figure 3.8, thus consists of an electron tagger (ET) at z≈ -33 m and a photon detector (PD) at z≈ -100 m. Both detectors are Čerenkov calorimeters made of crystals, with a total depth of $\approx 20\ X_0$. The ET is 154 mm square and made of 49 crystals whereas the PD is 100 mm square with 25 crystals. The position resolution of both detectors is 0.3–1.2 mm, and they have an energy resolution of $\sigma_E/E = 10\%/\sqrt{E} \oplus 1\%$ (E in GeV).

A lead filter and a water Čerenkov counter infront of the PD protects it from

the high synchrotron radiation flux and a 2 m long iron wall behind it shields it from the proton beam halo. In addition, the water counter can be used as a veto (VC) to select events where the photon did not interact with the lead filter.

Both the ET and the PD are on movable platforms, which enables them to be moved away from the beam line during injection and before the beams are dumped.

The luminosity system can also be used to identify photoproduction events at very low Q^2 ($Q^2 < 0.01\ GeV^2$) by requiring a signal in the ET and using the PD and VC as a veto.

The systematic error on the luminosity measurement for the 1993 running period, the main contribution to which arises from changes in the acceptance of the luminosity detectors with changes in the angle of the electron beam, is about 5% [22].

3.9 Trigger

The purpose of the trigger system is to select ep interactions and reject beam-induced background. It consists of four levels of triggers although, in the running period of 1993, only levels one and four had been implemented.

Every 96 ns an electron and a proton bunch cross and an ep interaction may occur. In order to decide whether an interaction occurred, information must be collected from nine separate trigger systems, each based on different parts of the H1 detector, and logically combined to form up to 128 subtriggers. This is the task of the first level trigger, L1. If any one of the subtriggers fires, an "L1 keep" signal will be generated and the event read out. However, much of the information needed by the L1 trigger to make its decision is not available until several bunch crossings after the event took place, due to cable delays and the finite response time of the detectors (for example, the longest drift time in the CJC is 1 μs, approximately ten bunch crossings). In fact the final L1 trigger decision is typically not available until 24 bunch crossings later.

To overcome this problem, the readout of the sub-detectors is pipelined. This means that each subdetector writes a continuous stream of digitized information

(for example, wire charge) to a buffer. The information is over-written after 2.5 μs, which gives sufficient time after an interaction for all the information to be collected and an L1 trigger decision to be made.

If the L1 trigger decides that an ep interaction has occurred, the event is read out. It is only then that the detector is disabled and "dead time" begins. As it takes on average about 1 ms to read out an event, in the future, a second level trigger, L2, will be used to reduce the amount of time for which the detector is disabled. It will be activated during the time the detector is being readout, and will analyse the event according to the subtrigger which produced the "L1 keep" signal. The L2 trigger will have a fixed time of 20 μs to make its decision. If it rejects the event, read-out stops and the detector is re-enabled. Then the net effect is that the detector was inactive for only 20 μs instead of 1 ms. If the L2 trigger accepts the event, readout continues.

The third level of triggering (L3) will use more complex topological studies of the event to make its decision in a few hundred μs. When implemented, it will lead to a further reduction is the deadtime.

The fourth level of triggering (L4) introduces no further dead-time as the detector is not disabled whilst the events are analyzed. It is a software trigger integrated into the central data acquisition system and has the raw data of the event available as a basis for the decision making algorithms. Tracks and clusters are reconstructed at this stage using the full reconstruction package H1REC [19] and cuts are applied according to the physics process which is believed to have occurred. An event accepted by the L4 trigger will be assigned to a class of physics events. The L4 trigger rejects about 70% of all the events accepted by L1 triggers.

This gives a general outline of the H1 triggering system. A more specific description of how it is used to select the sample of events used for the analysis in this thesis will be given in Chapter 4.

Chapter 4

Data Selection

4.1 Introduction

This chapter describes the selection of a sample of Neutral Current DIS events from the $\sim 500\ nb^{-1}$ of luminosity collected by H1 in 1993. In the following, a low Q^2 DIS event is defined as one in which the scattered electron is detected in the BEMC, limiting the Q^2 to be below about 120 GeV^2.

At the HERA design luminosity of $1.5 \times 10^{31} cm^{-2} s^{-1}$, the total rate of DIS events is approximately 0.1–1 Hz. This is small in comparison with the rate of beam induced background (interactions of the incident beams with either the beampipe itself or with the residual gas inside it) which at design luminosity is about 10^5 Hz. In 1993, the peak luminosity reached $1.5 \times 10^{30} cm^{-2} s^{-1}$, 10% of the design value.

In addition to the beam induced background, the dominant physics process at low Q^2 is photoproduction, with a rate of $\sim$ 120 Hz. As the momentum transfer from the incident electron in a photoproduction event is typically very small, the scattered electron will often remain in the beam-pipe. In some cases, it may be detected in the H1 luminosity system. Frequently (about 40% of the time), however, it is not and hadrons and photons produced in the backward direction may deposit energy in the BEMC, sometimes mimicking the signal of a low Q^2 DIS event.

The selection of a clean sample of low Q^2 events includes an L1 and L4 trigger

selection followed by a series of physics motivated cuts.

4.2 Trigger Selection

4.2.1 The L1 trigger

The initial selection of a possible DIS candidate is a hardware based decision from a specific L1 trigger, the BEMC Single Electron Trigger (BSET)[21]. The purpose of this trigger is to identify candidate scattered electrons in the BEMC.

The analogue signals from the four long wavelength shifters on the sides of each BEMC stack (see section 3.5.2) are summed to give a measure of the energy deposited in the stack. These stack energies are then compared to two energy thresholds; a low threshold ($\sim$1.3 GeV) just above the level of the noise and a high threshold ($\sim$2.3 GeV) which is used as a cluster seed. Any stack with an energy greater than the high threshold is clustered with all of its neighbours which have an energy above the low threshold.

There are several different trigger elements for the BSET, but the one used in the identification of low Q^2 DIS events requires the event to contain at least one cluster with energy greater than a threshold value, set to $\sim$ 7 GeV in 1993.

The efficiency of the BSET is a function of the cluster energy. It is $\sim$ 50% for a cluster of 8 GeV and $\sim$ 100% for one of 10 GeV [22].

As background events may also produce a large energy deposition in the BEMC, the BSET trigger is used in coincidence with the ToF system to ensure that a genuine ep interaction took place.

4.2.2 The L4 algorithm

The events accepted by L1 will then be passed to the L4 trigger. After the full reconstruction of tracks and clusters (see section 4.3), a decision is made based on a series of physics motivated cuts. The algorithm used depends on the L1 trigger which accepted the event.

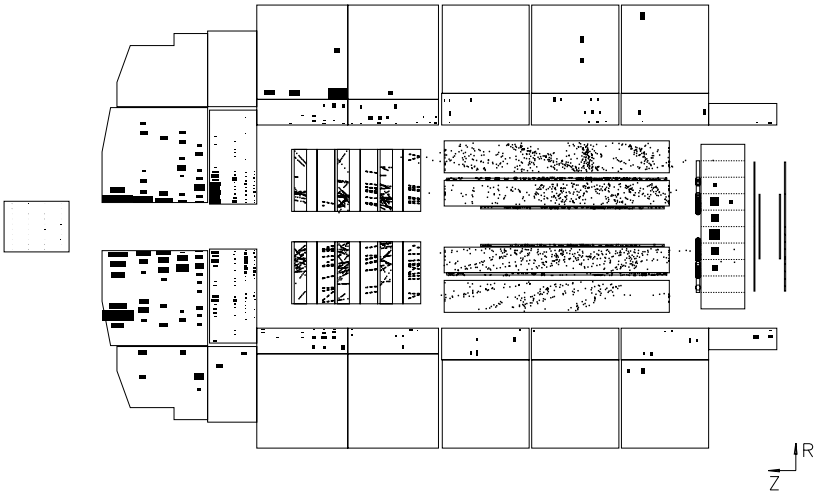

Figure 4.1: An r-z view of a beam-gas interaction. The vertex is clearly upstream from the nominal interaction point.

For an event accepted by the BSET trigger, the L4 algorithm is very simple. The first part is designed to remove events in the sample which are not genuine ep interactions. The event is rejected if it contains three or more reconstructed tracks in the CTD which originated from a point upstream from the detector, in the incident proton direction, or if it contains one or two such tracks with no additional reconstructed tracks coming from the interaction point. Such events are likely to have been an interaction between the incident proton beam and either the beam-pipe or the gas within it. An example of a beam-gas interaction can be seen in figure 4.1. The tracks in the CTD clearly originate from a point behind the BEMC.

The BSET trigger has a large background due to particles hitting a single photodiode in a BEMC stack. Such events are mainly caused by synchrotron radiation. So, an event will be rejected by the L4 trigger if any one diode in a stack registers more than 80% of the signal in that stack.

4.3 Event Reconstruction

The reconstruction of tracks and clusters is performed using the H1REC[19] program. As this thesis is concerned primarily with energy flow, I will describe briefly the reconstruction of clusters in the H1 calorimeter system[26]. Details of track reconstruction may be found elsewhere ([15] and references therein) .

The aim of the reconstruction program is to take the digitized charge information from each calorimeter cell and convert it into an energy measurement, correcting for the effects of dead material, eliminating noise and compensating for the different response to electromagnetic and hadronic showers.

The Liquid Argon Calorimeter

The first stage of cluster reconstruction in the Liquid Argon Calorimeter is noise suppression. The noise level for each cell is known, corresponding to an energy of between 10 and 30 MeV, and the signal is approximately Gaussian. After pedestal subtraction, the signal is required to be either $\pm 2\sigma$ or $\pm 3\sigma$ from the noise level of the cell, where σ is the width of the Gaussian, depending on the position of the cell within the calorimeter. A further noise cut applied off-line rejects all cells with signals within $\pm 4\sigma$ of the noise level, unless the cell passed the on-line noise cuts and is adjacent to one which passed this 4σ cut. The aim of this procedure is to keep as much of the signal near the edges of the showers as possible, given constraints on data volume. By keeping cells with a negative energy, the noise which exists in addition to the signal for the positive cells is compensated for.

The scaling from charge to energy (the electromagnetic scale) involves applying a calibration factor which was determined for each stack in calibration runs at CERN [17].

In low Q^2 events ($Q^2 < 100\ GeV^2$), the particles produced are low energy (the average energy per particle is ~ 800 MeV for a hadron and ~ 400 MeV for a photon) and the average energy deposited in the barrel region of the calorimeter is only 4.5 GeV. For such events, about 15% of the energy deposited in the calorimeter is lost during noise suppression. For high Q^2 events, the loss is much

smaller (about 5%).

All the cells which pass the off-line noise cuts are used in cluster reconstruction. The aim is to form clusters from groups of cells such that there is a close correspondence between clusters and particle showers. However, there are conflicting requirements for the typically small electromagnetic showers and the more dispersed hadronic showers. The algorithm is tuned to collect the cells from a single electromagnetic shower into one cluster, but the hadronic showers are typically reconstructed as several clusters.

The clustering algorithm is as follows:

- All cells with positive energy are grouped into clusters.
- Negative cells close to clusters are merged with them.
- Clusters with negative energy are considered unphysical and are disregarded.
- Isolated negative cells remain unclustered.

In low Q^2 DIS about 10% of the energy deposited in the calorimeter is lost in dead material (the beam-pipe, CTD, inner wall of the cryostat etc). The corrections for this energy loss are obtained from detailed Monte Carlo simulations [15].

Electromagnetic clusters are identified by examining the cluster shapes. As the Liquid Argon Calorimeter is a non-compensating calorimeter, a weighting factor, obtained from Monte Carlo studies, must be applied to all the hadronic clusters. In addition, in 1993, an additional factor of 1.25 was applied to all energy deposits in the very backward region of the Liquid Argon Calorimeter, where there is no hadronic section in the calorimeter [26].

The BEMC

In the BEMC, there is no noise suppression performed at the cell level. Any cell with an energy greater than 3σ ($\sim$ 400 MeV) is a cluster seed, and forms

a cluster with all eight of its neighbours, including those with a negative energy. If two clusters overlap, each cell in the overlap region is treated as an individual cluster. Negative energy clusters are then discarded.

In addition, all hadronic energy deposits in the BEMC are scaled by a factor of 1.6 ([26]), owing to the poor hadronic response of the detector (see section 3.5.2).

The Tail Catcher

In the tail catcher, all cells with a positive energy above 3σ are kept, and assigned to a cluster. In addition, a scale factor of 1.6 is applied to all energy in the most backward region of the iron, beyond the edge of the HCAL ([26]).

4.4 Off-line Selection

The sample of events accepted by the L4 trigger will still include some photoproduction and beam induced background events. An additional set of cuts applied off-line are designed to reduce this background further.

The candidate scattered electron, defined as the most energetic BEMC cluster, is required to have an energy greater than 14 GeV. This cut substantially reduces the photoproduction background in the sample. Figure 4.2 shows the energy spectrum above 10 GeV of the candidate electrons for the data (points) and LEPTO, a standard DIS Monte Carlo (see section 2.8). The distributions are normalized to have the same number events above 14 GeV, where they are in good agreement. Below 14 GeV, the energy spectrum shows a rise for the data which is not predicted by LEPTO. This can be attributed to photoproduction background in the data, when the scattered electron is undetected but hadrons and electrons in the backward direction give rise to a BEMC cluster. It can be seen that the energy of such clusters is typically below 14 GeV, as the electron energy spectrum is satisfactorily described by a DIS Monte Carlo above this energy.

The most energetic BEMC cluster must be accompanied by at least one hit

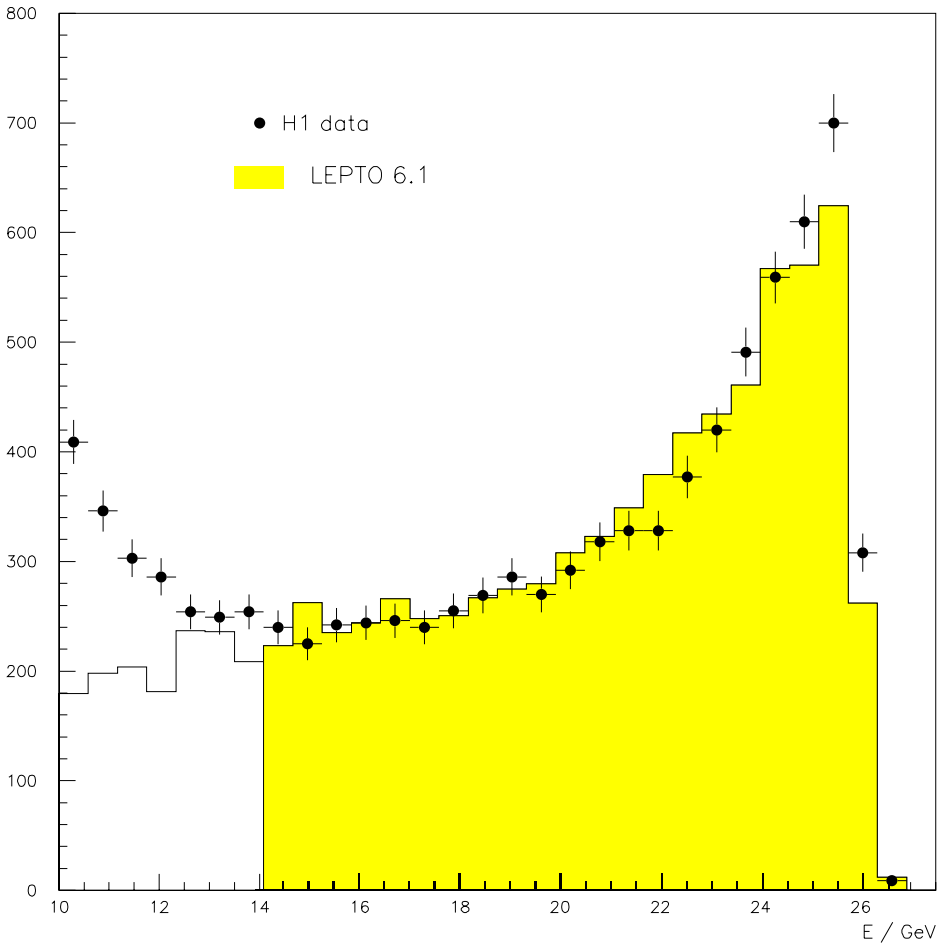

Figure 4.2: The energy of the most energetic BEMC cluster for data (points) and LEPTO 6.1. The two distributions are normalized to have the same number of events above 14 GeV. The data shows a rise in the energy spectrum below 14 GeV which LEPTO does not reproduce. This can be attributed to the presence of photoproduction in the data sample. The distributions are in good agreement above 14 GeV.

in the BPC within 5 cm of its centre of gravity in order to define the angle of the scattered electron accurately. In addition the hit must be at a radius of less than 60 cm, to ensure that the associated BEMC cluster is well contained.

As the energy calibration of the BEMC triangular stacks close to the beam-pipe is not properly understood, the candidate electron cluster must lie outside this region ie:

$$| x_e | > 14\text{cm}$$

$$| y_e | > 14\text{cm}$$

Also, to ensure full containment of the shower in the BEMC, the polar angle θ of the candidate scattered electron must be less than 173°.

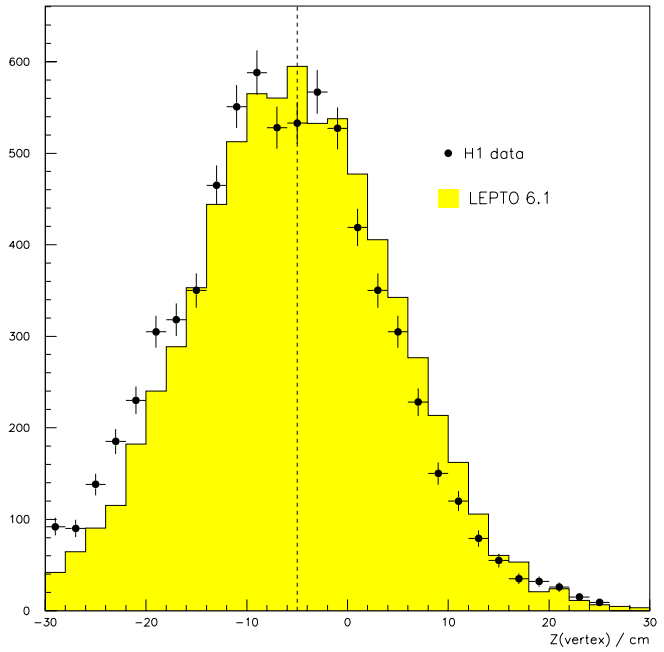

Figure 4.3: The z vertex distribution for a sample of selected low Q^2 events for data (points) and LEPTO 6.1 (shaded histogram) The nominal interaction point is at -5cm and the cut of ± 30 cm has been applied

An event vertex, defined from tracks in the CTD and FTD, must be reconstructed and the z coordinate must lie between ± 30 cm. As the nominal interaction point in the 1993 data is at -5 cm, this cut removes more events with

a negative z vertex than with a positive z vertex. This is designed to remove events in which protons in the non-colliding bunches interact with residual gas in the beam pipe, as these will have a negative z vertex. At least one of the tracks in the CTD must satisfy the following criteria to ensure that the quality of the vertex reconstruction is good:

- Number of hits ≥ 10
- $P_T > 100$ MeV
- $\frac{\delta p}{p} < 0.5$ where δp is the error on the measured momentum p
- The track fit must have a χ^2 per degree of freedom less than 10.

The distribution of the z vertex after the cuts for both the data sample and events from LEPTO after detector simulation is shown in figure 4.3.

To ensure a substantial amount of hadronic energy in the calorimeter, the invariant mass of the hadronic system, W^2 (calculated from the double-angle method [1]) is required to be greater than 3000 GeV^2.

Finally, there must be no coherent noise (a group of cells registering a signal which in reality is not associated with an energy deposition but comes directly from the electronics in the readout) identified in the Liquid Argon Calorimeter. Events from the period of 1993 when the H1 magnetic field was zero are also not included.

4.5 Electron Identification

The identification of the scattered electron in a DIS event is crucial. In the data sample used in this analysis, the highest energy BEMC cluster is assumed to be the electron. The electron energy is reconstructed from the cluster energy after corrections for losses due to the material in front of the BEMC. The angles θ and ϕ are calculated from the BPC hit closest to the centre of gravity of this cluster.

Figures 4.4*a–f* show the resolution in the reconstruction of the electron 4-vector. The reconstructed electron E, θ and ϕ are compared with the generated quantities.

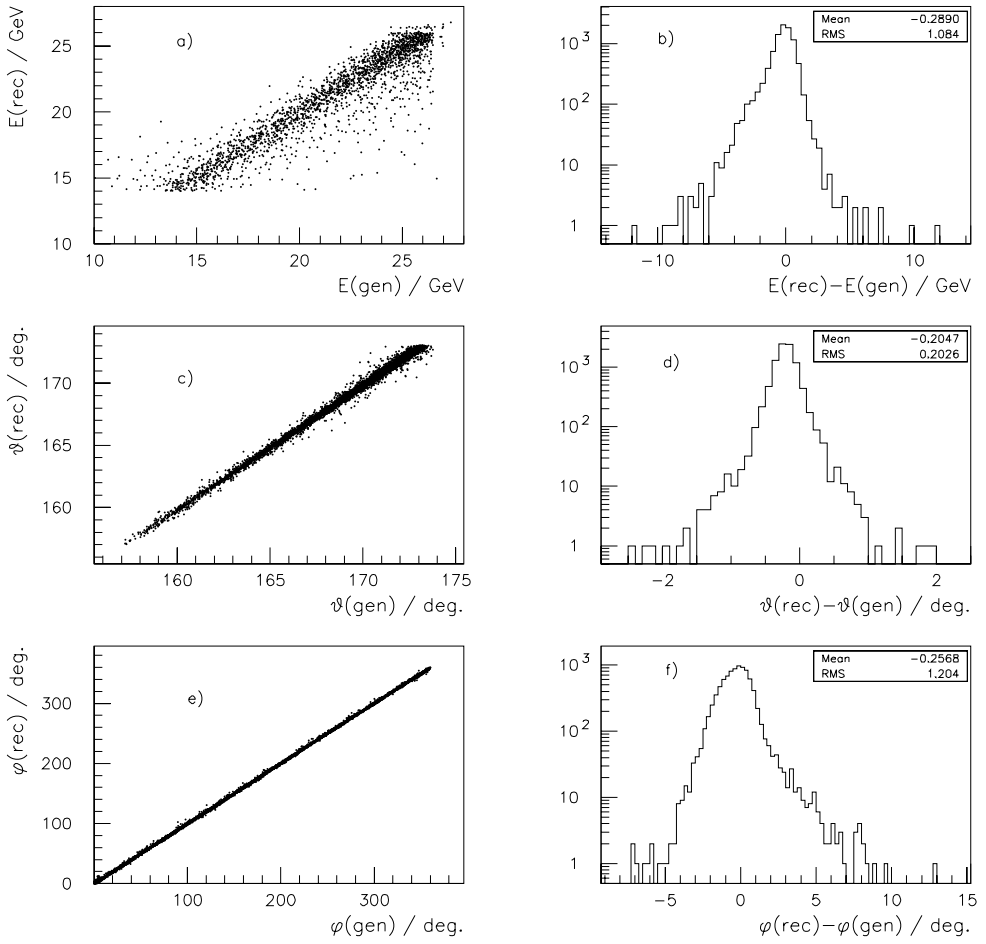

Figure 4.4: The reconstructed electron compared with the generated electron: a),b) Energy; c),d) θ; e),f) ϕ

4.6 Residual background in the data sample.

To study the amount of background remaining in the low Q^2 DIS sample, a comparison between the data and LEPTO 6.1 was made.

4.6.1 Study of background using $E - P_z$

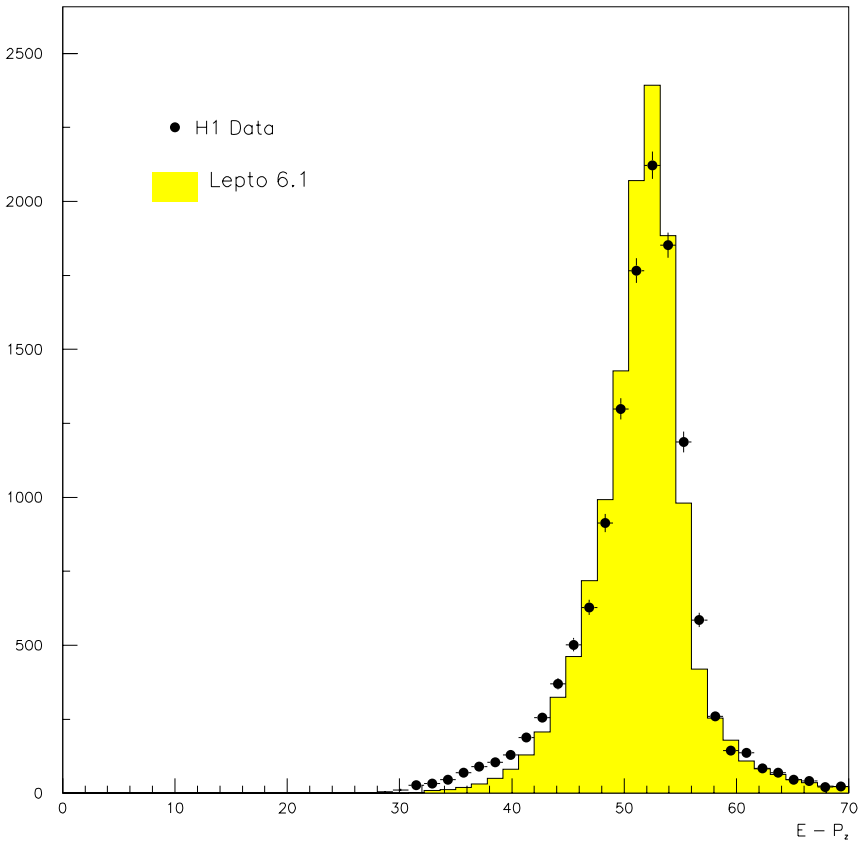

Figure 4.5: $E - P_z$ distributions for data and LEPTO 6.1.

A useful variable to consider is $E - P_z$, where E is the total energy reconstructed in an event, and P_z is the z component of the total momentum. If all the particles produced in the interaction are detected:

$$E = E^p + E^e$$

$$P_z = P_z^p + P_z^e$$

where the superscript p refers to the incident proton and e to the incident electron. Assuming the masses of the particles are small, $E^p = P_z^p$ and $E^e = -P_z^e$ so:

$$E - P_z = 2E^e$$

However, in the H1 detector, particles are lost down the beam-pipe. If the superscript + refers to the forward direction and − to the backward direction:

$$E = E^p + E^e - E^+(lost) - E^-(lost)$$

$$P_z = P_z^p + P_z^e - P_z^+(lost) - P_z^-(lost)$$

Again, $E^+(lost) = P_z^+(lost)$ and $E^-(lost) = -P_z^-(lost)$, so:

$$E - P_z = 2E^e - 2E^-(lost)$$

In a DIS event, particles are primarily lost only in the forward (proton) direction, so $E - P_z \approx 2E^e$. In a photoproduction event, however, the scattered electron is lost in the backward direction, so $E - P_z \ll 2E^e$. If a proton in the incident beam interacts with a stationary particle in the beam-pipe or with the beam-wall itself, $E = E_p$ and $P_z = P_z^p$, so $E - P_z \approx 0$. Thus, the distribution of $E - P_z$ is useful in discriminating DIS events from photoproduction and proton beam background.

Figure 4.5 shows the $E - P_z$ distribution for the low Q^2 DIS sample, compared with the prediction from LEPTO. Both distributions are normalized to the same number of events. The peak at $2E^e$ (53.4 GeV) is clearly visible, although broad as the experimental resolution in the measurement of $E - P_z$ is poor. There is reasonable agreement between data and Monte Carlo. There are a few more events with $E - P_z \ll 2E^e$ in the data than LEPTO predicts, but this is consistent with the small amount (less than 3% [24]) of residual photoproduction in the data sample.

There is no hint of a class of events in the data for which $E - P_z \ll 2E^e$ or zero, so the number of beam induced background events in the low Q^2 event sample appears to be small (it has been measured to be less than 1% [23]).

4.6.2 Rapidity Gap events

There is an additional class of events in the data sample which cannot be explained by a standard DIS Monte Carlo.

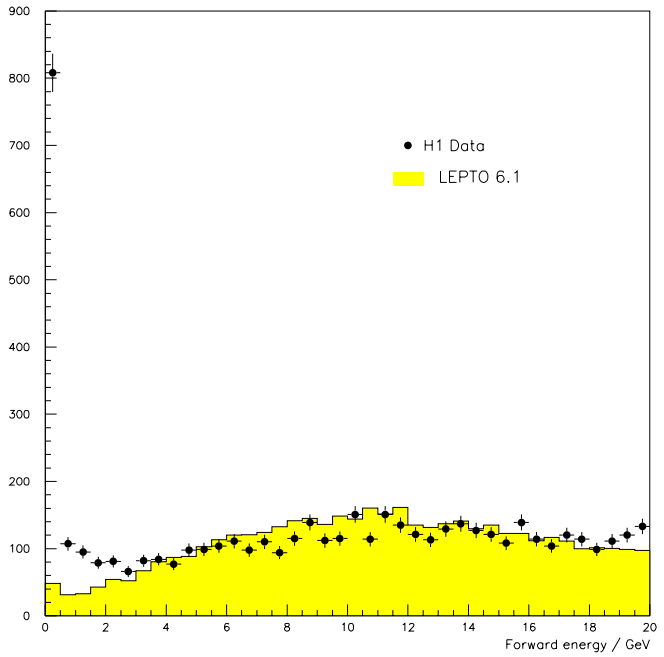

Figure 4.6: The total energy in the forward region of the detector ($\theta < 15°$). The distributions are normalized to have the same number of events above 500 MeV. There are clearly more events in the data where the energy in the forward region is negligible (E <500 MeV) than are predicted by LEPTO. These are the 'rapidity gap' events.

Figure 4.6 shows the distribution of the total amount of energy in the very forward ($\theta < 15°$) region of the detector for both data (points) and LEPTO (solid histogram). The two distributions are normalized to have the same number of events above 500 MeV. It can be seen that in the data there is a class of events in which the energy in the forward region of the detector is virtually zero ($\leq$ 500 MeV). This is not true in the DIS Monte Carlo.

These events with little or no forward energy are referred to as 'rapidity gap' events [27], and are believed to be diffractive in nature [28]. The 'empty' forward calorimeter is consistent with there being no colour flow between the struck object and the proton remnant. As the Monte Carlo used in this analysis does not include such events, they are removed from the data sample by requiring that the total amount of energy in the Liquid Argon Calorimeter in the region $\theta < 15°$ is greater

than 500 MeV.

The background from diffractive events has been estimated as 8% [25], although a fraction of these events will be removed by the exclusion of 'rapidity gap' events.

4.7 Summary

Using a selection based on an electron trigger and a series of physics cuts designed to remove background from photoproduction and non ep interactions, a clean sample of approximately 25,000 NC DIS events in the range $5 < Q^2 < 100 GeV^2$ and $10^{-4} < x < 10^{-2}$ was selected. One of the events in the sample, showing the reconstructed tracks and clusters, is shown in figure 4.7.

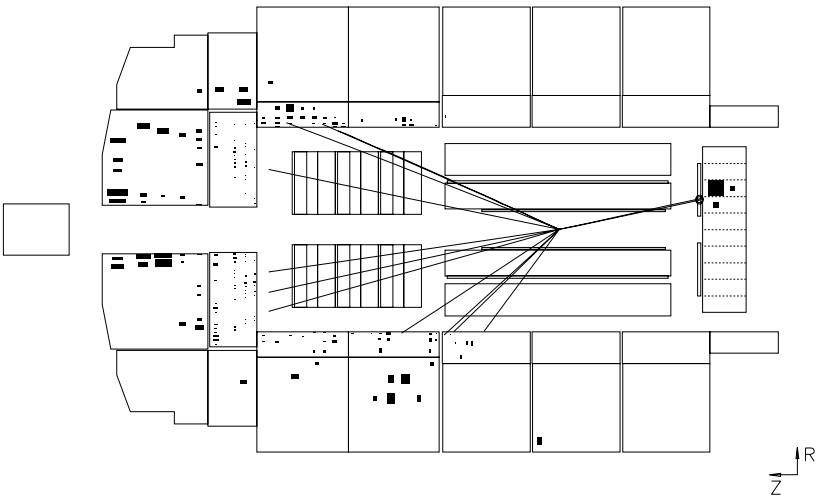

Figure 4.7: An r-z view of a low Q^2 DIS event in the H1 detector showing the reconstructed tracks and clusters.

The population of the events on the x, Q^2 plane is shown in figure 4.8. The effect of the cuts on the energy and the angle of the scattered electron are clearly seen.

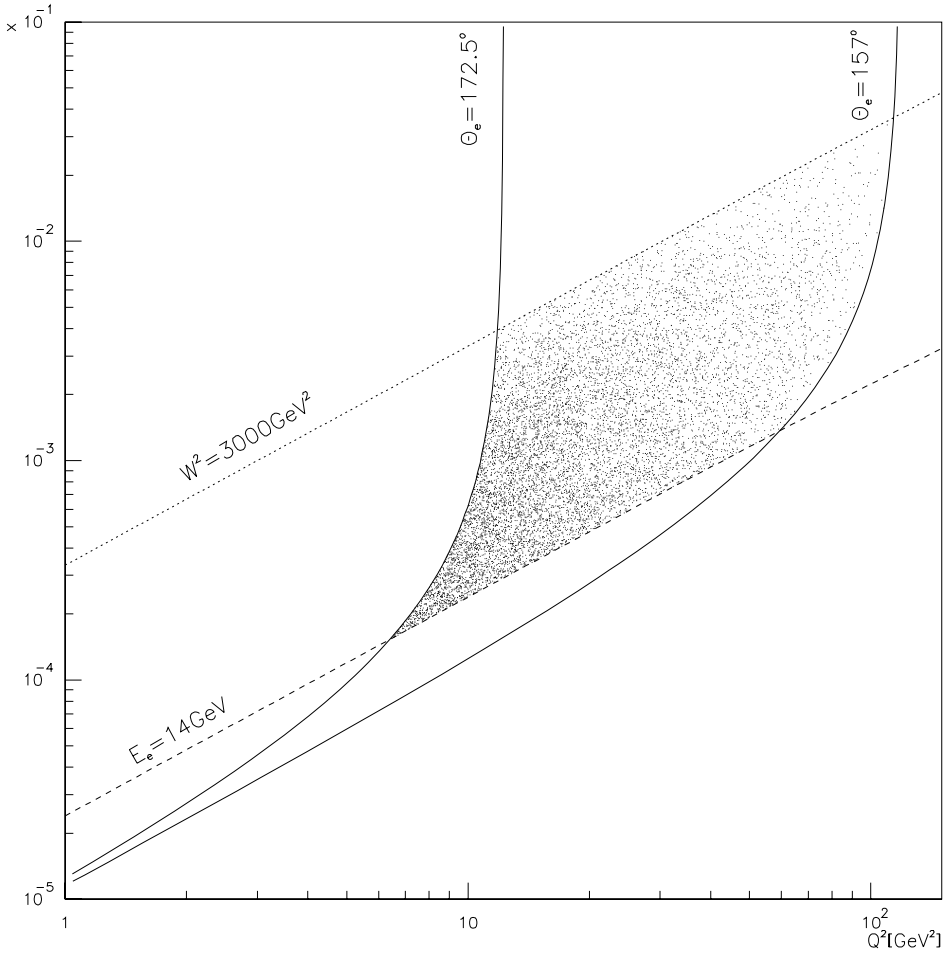

Figure 4.8: The (x, Q^2) plane showing the data sample used in this analysis. The effects of the cuts on the electron and on W^2 are clearly seen

Chapter 6

Hadronic Energy Flow

6.1 Introduction

In the naive picture of DIS in the Quark Parton Model (QPM) introduced in chapter 2, a single quark is scattered out of the proton by the virtual boson "emitted" from the incident electron. QCD tells us that, in reality, gluons may be radiated from the quark and also that the boson can interact with a gluon inside the proton by means of a quark line (BGF) (see figure 2.2). Such QCD effects have already been seen by other experiments (eg.[33]). The increased phase space (low x, high W) available for QCD radiation at HERA energies makes the hadronic final state an ideal place to examine these QCD effects.

In this chapter, the basic properties of the hadronic final state in the sample of low Q^2 NC DIS events are studied, both in the laboratory frame and in the Hadronic Centre of Mass frame (HCMS). The results are compared with the QCD inspired model LEPTO 6.1 [29] described in chapter 2. Further model comparisons may be found elsewhere ([23] and [31]).

6.2 P_t balance in the Laboratory frame

If the exchanged boson interacts with a stationary parton inside the proton, the transverse momentum of the scattered electron (P_t^e) with respect to the beam-axis must balance that of the hadronic final state (P_t^{had}). In practice, however,

this is only approximately true as the partons in the proton are not stationary, but have a "primordial" transverse momentum (k_T). Moreover, hadrons within the beam pipe remain undetected, and will not contribute to the measurement of P_t^{had}.

The distribution of the ratio of P_t^{had} to P_t^e is useful because the mean value depends only on the electromagnetic energy scale of the BEMC, where the electron is detected, and on the hadronic energy scale of the Liquid Argon Calorimeter. It has already been shown that the electron energy spectra for data and LEPTO are in good agreement (figure 4.2) and therefore that the BEMC electromagnetic scale is well-known (to a precision of $\sim 2\%$ [32]). Consequently, any difference in the mean value of the P_t balance for data and for a sample of events generated by LEPTO and passed through the full detector simulation, H1SIM [30], can be entirely attributed to an uncertainty in the absolute hadronic energy scale of the Liquid Argon Calorimeter.

Figure 6.1*a* shows the ratio of P_t^{had}/P_t^e for events generated by LEPTO after the standard simulation of the H1 detector. Figure 6.1*b* shows the same distribution for the data. In both cases, P_t^{had} is calculated from the calorimeter clusters. As expected, both distributions have a mean value below one, but the value of the mean is significantly lower for the data (0.867 compared with 0.913). This implies a 5% difference between the Liquid Argon Calorimeter hadronic energy scale in the data and that used in the standard detector simulation. Figure 6.1*c* shows the same two P_t balance distributions after applying a 5% scale factor to all the hadronic energy detected in the Liquid Argon Calorimeter in the H1 data sample. The data and Monte Carlo distributions are now in good agreement. This calibration factor is applied throughout the analysis described in this thesis.

6.3 Energy Flow in the Lab Frame

The topology of an event depends strongly on the kinematics. In the naive Quark Parton Model, there is a direct relation between the energy and the angle of the struck quark and y and Q^2. If we denote the polar angle of the struck quark as γ and its energy as E_q:

$$\cos\gamma = \frac{Q^2(1-y) - 4E_e^2y^2}{Q^2(1-y) + 4E_e^2y^2} \tag{6.1}$$

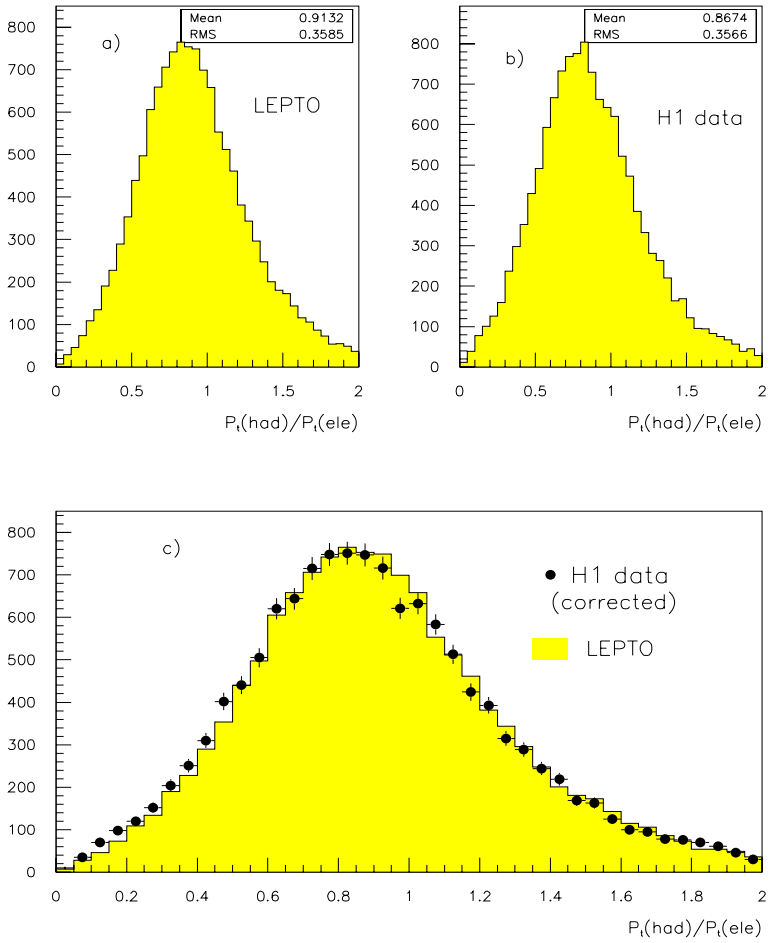

Figure 6.1: P_t^{had}/P_t^e for a) LEPTO 6.1 after full detector simulation, b) H1 data, c) LEPTO 6.1 after detector simulation (solid histogram) and H1 data (points) after applying a 5% correction factor to all hadronic energy in the Liquid Argon Calorimeter

$$E_q = \frac{Q^2(1-y) + 4E_e^2 y^2}{4E_e y} \tag{6.2}$$

In the QPM, the scattered quark and the scattered electron will be back-to-back in the azimuthal angle, ϕ.

Figures 6.2*a–c* show the transverse energy flow (E_t) relative to the direction of the scattered quark as predicted by the QPM. Figure 6.2*a* shows the two dimensional energy flow in (η,ϕ) space, where the pseudorapidity η is defined as:

$$\eta = -\ln(\tan\frac{\theta}{2})$$

for the low Q^2 data sample. Although a clear jet structure can be seen (the 'current' jet), higher order QCD processes and hadronization effects shift the position of the jet away from the origin (the predicted quark direction), towards the proton remnant, and result in energy being deposited between the jet and the proton remnant.

Figures 6.2*b* and *c* show the projections of figure 6.2*a* onto the ϕ and η axes respectively. In both cases it can be seen that the energy flow close to the predicted quark direction is reasonably well described by LEPTO after detector simulation. Away from this region the data has a significant excess of transverse energy over the Monte Carlo prediction.

Figure 6.3 shows the mean transverse energy flow (E_T) per event as a function of η in several different bins of x and Q^2. In each case, the position of the struck quark as predicted by the simple QPM (equation 6.1) is shown by a dotted line. The points are from the low Q^2 data sample and the shaded histogram is the prediction from the LEPTO Monte Carlo after detector simulation.

The initial rise in the distribution for negative values of η marks the beginning of the current jet. In this region, there is good agreement between the sample of events generated by LEPTO and the data. The position of the current jet does not coincide exactly with the QPM prediction, because of the presence of higher order QCD processes, but it does move with x and Q^2 in a similar way.

As we move forward in η, away from the current jet and towards the proton remnant, there is significant disagreement between the data and the events from LEPTO. This is especially true at low x and Q^2 (figures 6.3 *a–d*). The data has significantly more transverse energy in this region than LEPTO with standard detector simulation predicts.

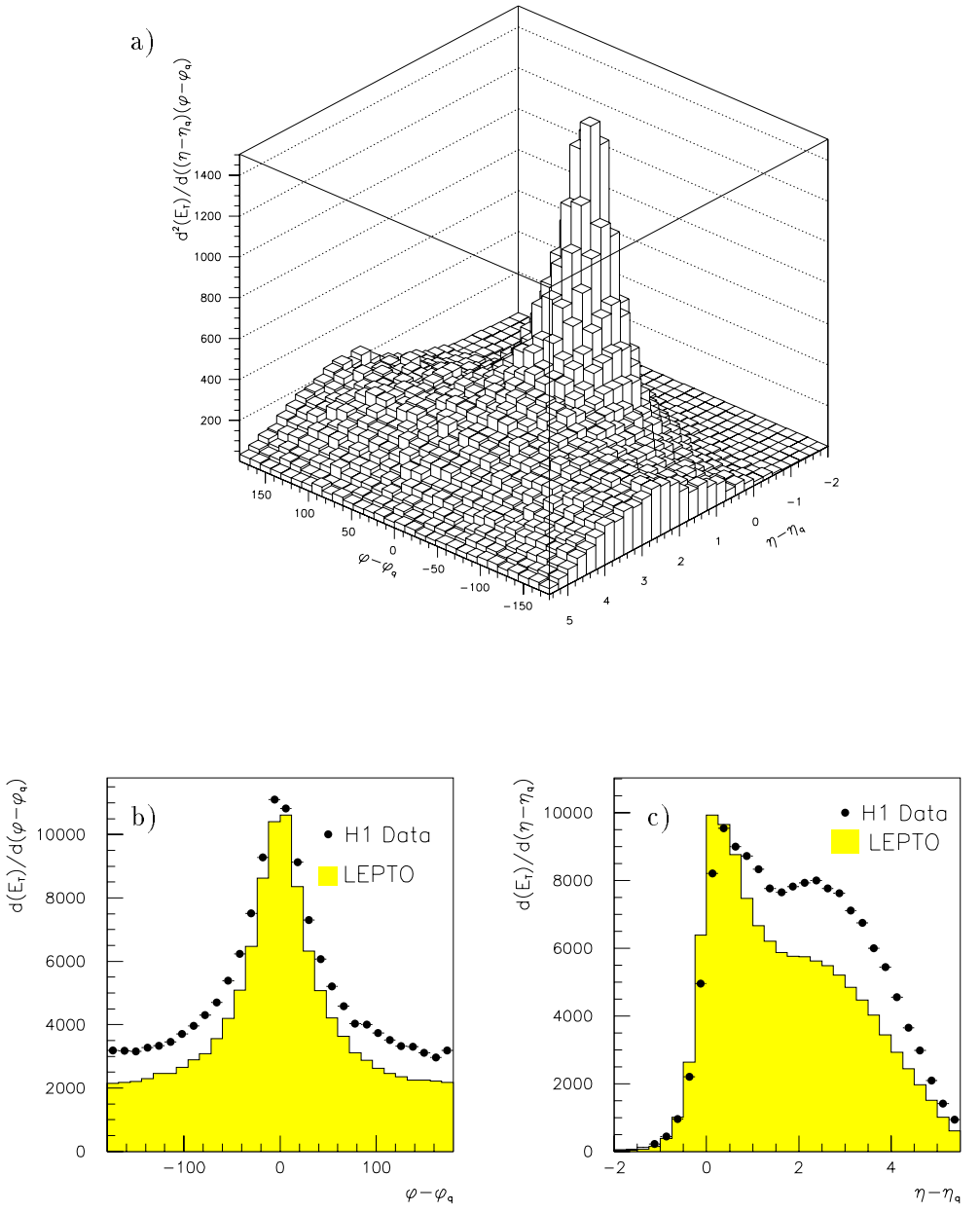

Figure 6.2: Transverse energy flow around the direction of the scattered quark as predicted by the QPM. a) shows the energy flow in (η,ϕ) space for the sample of low Q^2 data. b) and c) show the projections in ϕ and η respectively for the data sample and for a sample of events generated by LEPTO with full detector simulation.

This effect has been noticed with other Monte Carlo generators [23] and will be discussed further in the course of this thesis.

6.4 The Hadronic Centre of Mass Frame

The HCMS is the centre of mass frame of the proton and the exchanged boson. It is a natural frame in which to study the hadronic final state and provides, at least in the QPM case, a clear separation in rapidity between the struck quark and the proton remnant.

The boost from the laboratory to the HCMS can be defined entirely from the co-ordinates of the scattered electron, E'_e, θ_e and ϕ_e. If the incident electron has energy E_e then the 4-vector of the exchanged boson is defined as:

$$q = \begin{pmatrix} E_e - E'_e \\ -E'_e \sin\theta \cos\phi \\ -E'_e \sin\theta \sin\phi \\ -E_e - E'_e \cos\theta \end{pmatrix} \tag{6.3}$$

Thus, if the energy of the incident proton is E_p, the 4-vector of the HCMS in the laboratory is:

$$q + p = \begin{pmatrix} E_e - E'_e + E_p \\ -E'_e \sin\theta \cos\phi \\ -E'_e \sin\theta \sin\phi \\ -E_e - E'_e \cos\theta + E_p \end{pmatrix} \tag{6.4}$$

The co-ordinate system in the HCMS is shown in figure 6.4. The boson direction defines the positive z axis, and the plane formed by the incident and scattered electron is defined as $\phi = 0°$. The polar angle in the HCMS, θ^*, is defined with respect to the boson direction. In this frame and within the QPM, the scattered quark moves forward and the proton remnant backwards.

Clearly, the resolution in the reconstruction of the scattered electron 4-vector will lead to an error on the momentum measurement of particles in the HCMS.

Figures 6.5*a–d* show the effect of the resolution of the scattered electron

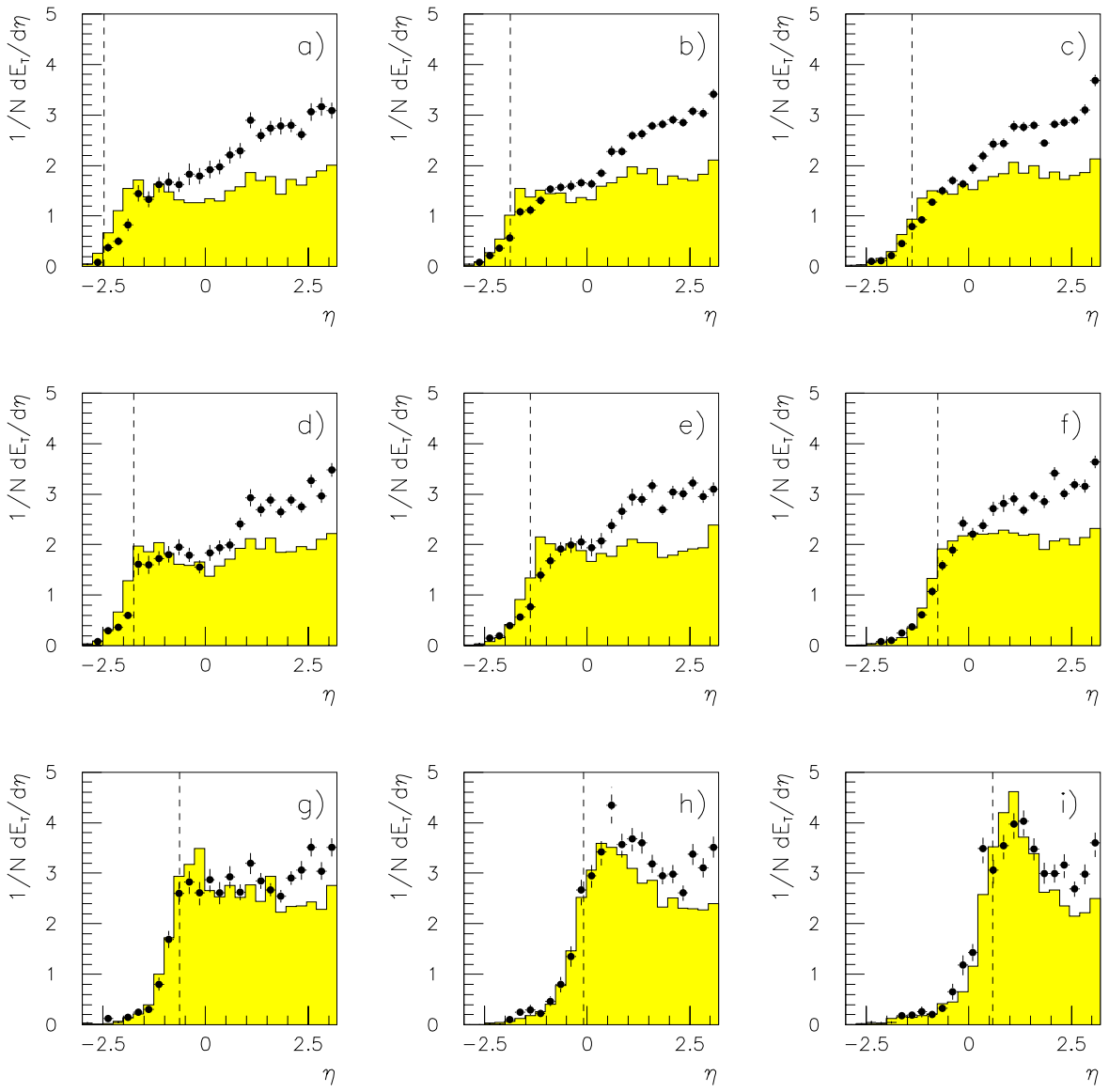

Figure 6.3: E_T flow per event versus pseudorapidity, η, in the laboratory frame, in the following bins of x and Q^2:

a) $10.0 \leq Q^2 < 13.3$; $-3.7 \leq \log x < -3.5$; **b**) $10.0 \leq Q^2 < 13.3$; $-3.5 \leq \log x < -3.3$
c) $10.0 \leq Q^2 < 13.3$; $-3.3 \leq \log x < -3.2$; **d**) $17.8 \leq Q^2 < 23.7$; $-3.3 \leq \log x < -3.2$
e) $17.8 \leq Q^2 < 23.7$; $-3.2 \leq \log x < -3.0$; **f**) $17.8 \leq Q^2 < 23.7$; $-3.0 \leq \log x < -2.8$
g) $42.2 \leq Q^2 < 56.2$; $-2.8 \leq \log x < -2.5$; **h**) $42.2 \leq Q^2 < 56.2$; $-2.5 \leq \log x < -2.3$
i) $42.2 \leq Q^2 < 56.2$; $-2.3 \leq \log x < -2.0$

The points are for H1 data and the solid histogram for LEPTO after full detector simulation. The dotted line in each case marks the direction of the struck quark predicted by the QPM. Note the disagreement between the data and LEPTO in the forward region.

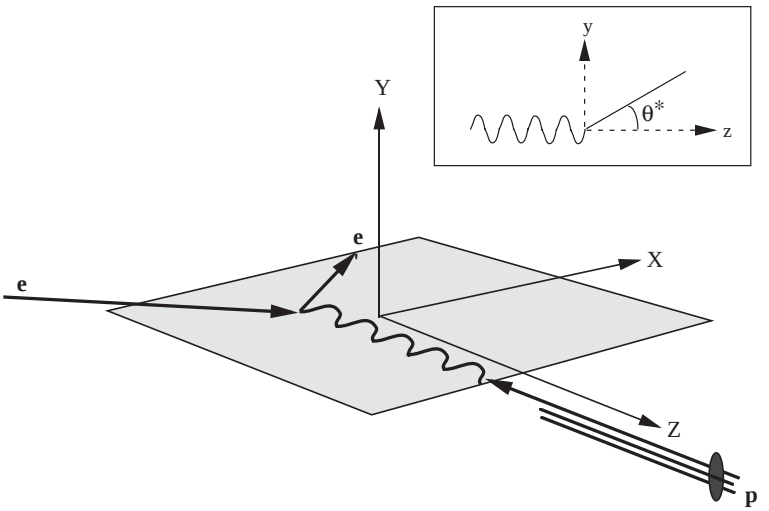

Figure 6.4: The coordinates in the HCMS

4-vector on the reconstruction of the hadron vectors in the HCMS, using the LEPTO Monte Carlo. The 4-vectors in the HCMS obtained by boosting using the reconstructed electron are compared to those obtained when the boost is performed using the true scattered electron. The boost from the laboratory frame to the HCMS consists of a longitudinal boost along the proton direction, a transverse boost (as the proton and boson are not collinear in the laboratory frame) and a rotation. However, the longitudinal boost is much larger than the transverse boost. This results in the error on the measurement of P_z in the HCMS being larger than either the error on P_x or on P_y. This can be seen in figure 6.5. Moreover, the transverse boost is essentially within the lepton plane (the $x-z$ plane) , so the error on P_y is significantly less than the error on P_x.

6.5 Energy Flow in the Hadronic Centre of Mass

Figure 6.6 shows the energy flow as function of the cosine of the polar angle in the HCMS, θ^*. The points show the energy flow for the data and the shaded histogram is the prediction from LEPTO after full detector simulation. The distributions are normalized such that the number of events is the same in both cases.

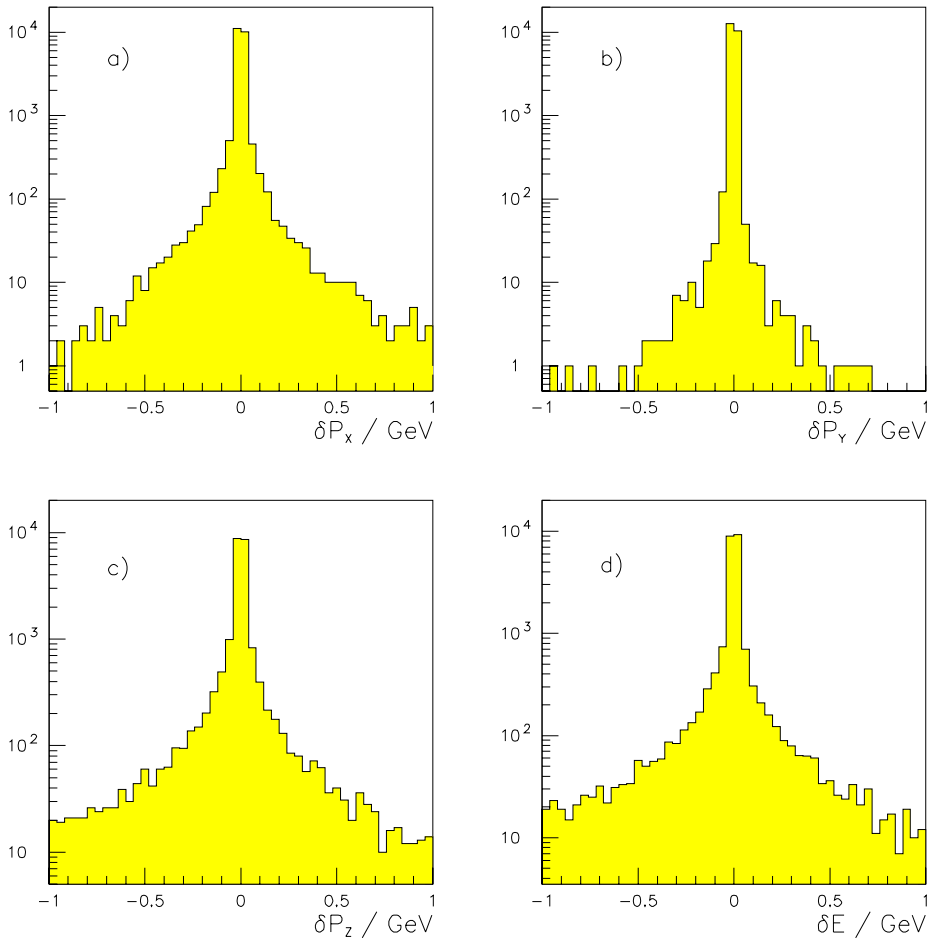

Figure 6.5: The effect of the resolution of the scattered electron 4-vector on the reconstruction of the hadronic final state in the HCMS. A comparison is made between the 4-vectors in the HCMS obtained using the true electron co-ordinates to define the boost and using the measured electron 4-vector. Figures *a–d* show the differences in P_x, P_y, P_z and E for each 4-vector in the HCMS

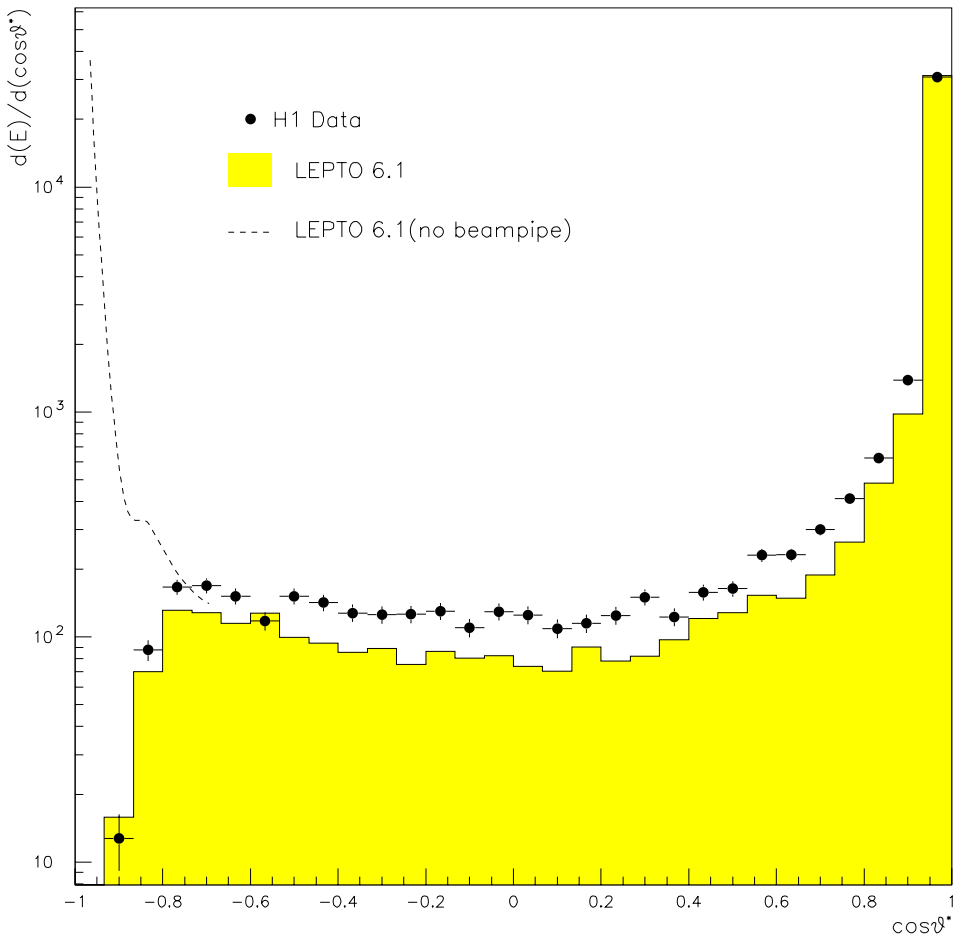

Figure 6.6: Energy flow as a function of $\cos\theta^*$ in the HCMS. All the distributions are normalized to the same number of events. The dotted line shows the prediction from LEPTO without the effects of detector acceptance.

In the QPM, we expect the struck quark to be at $\cos\theta^* = 1$ and the proton remnant at $\cos\theta^* = -1$. The current jet is clearly visible at $\cos\theta^* = 1$ in figure 6.6. The dotted line shows the prediction from LEPTO after hadronization but without detector simulation and the proton remnant jet is clearly visible. In reality, of course, we do not see the proton remnant, so the shape of the distribution near $\cos\theta = -1$ in the data can be explained by detector acceptance.

The energy in the central region of this plot arises from hadronization effects and from the presence of higher order QCD processes in the data. It can be seen that the energy in this region is higher for the data than for the LEPTO model after standard detector simulation. The details of this distribution will be discussed further in the next chapter.

As explained in section 6.4, the incident and scattered electron define a plane. The component of the momentum of a hadron in the HCMS which is perpendicular to this lepton plane is less sensitive to the accuracy of the boost to the HCMS than either of the momentum components in the plane. As the vectorial sum of the momentum components perpendicular to this plane is expected to be zero (boost errors and smearing will mean this is not totally true), we use a scalar sum:

$$P^{out} = \sum_i \mid P_y^i \mid \tag{6.5}$$

where the summation is performed over all clusters in the hadronic final state except the electron. In the QPM, the scattered quark and the proton remnant both lie along the z axis in the HCMS, and at the parton level P^{out} is zero. We believe that P^{out} could be sensitive to the presence of higher order QCD processes in the data and to hadronization effects.

Figure 6.7 shows the distributions of P^{out} for data and a sample of events from LEPTO after detector simulation. The two distributions are normalized to the same number of events. It can be seen that LEPTO predicts significantly less events with a large value of P^{out} than is seen in the data. Again, the details of this distribution will be discussed further in the following chapter.

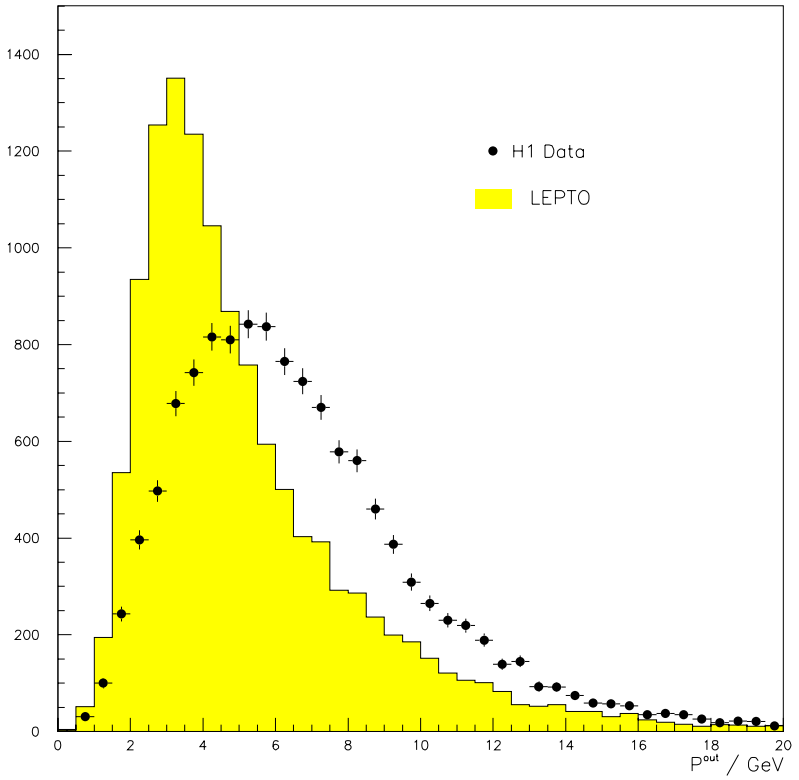

Figure 6.7: P^{out} for H1 data and LEPTO.

6.6 Conclusions

In this chapter we have discussed the basic topology of the hadronic final state, both in the laboratory frame and the HCMS. It has been shown that although the distributions for the sample of low Q^2 events are qualitatively correct, they are not described in detail by LEPTO with the standard detector simulation. The implications for this will be discussed in the following chapters.

Chapter 7

The Colour Force in DIS

7.1 Introduction

In Neutral Current DIS, the gluon content of the proton cannot be measured directly as the exchanged boson couples only to quarks. However, it can in principle be calculated at $O(\alpha_s)$ from the rate of gluon initiated processes.

In this chapter, differences in the hadronic final states of the three hard subprocesses QPM, QCD Compton and BGF (see chapter 2) are studied, with a view to finding a way to distinguish between them and hence to measure the rate of BGF in the data. The origin of the differences is discussed, and is shown to be a consequence of the colour nature of the partonic state before hadronization.

7.2 Definition of Hard Subprocesses in LEPTO

As discussed in chapter 2, the BGF and QCD Compton Matrix Elements are divergent (soft and collinear singularities). This means that for practical Monte Carlo simulation it is necessary to avoid the singular regions of the matrix elements. One way of achieving this is to apply a cut-off in the invariant mass of the parton pairs produced in BGF and QCD Compton, m_{ij}. BGF and QCD Compton events will then only be generated if they satisfy the requirement of the cut-off. In other words, the definition of a sample of QPM, QCD Compton or BGF events in a Monte Carlo depends on the value of this cut-off.

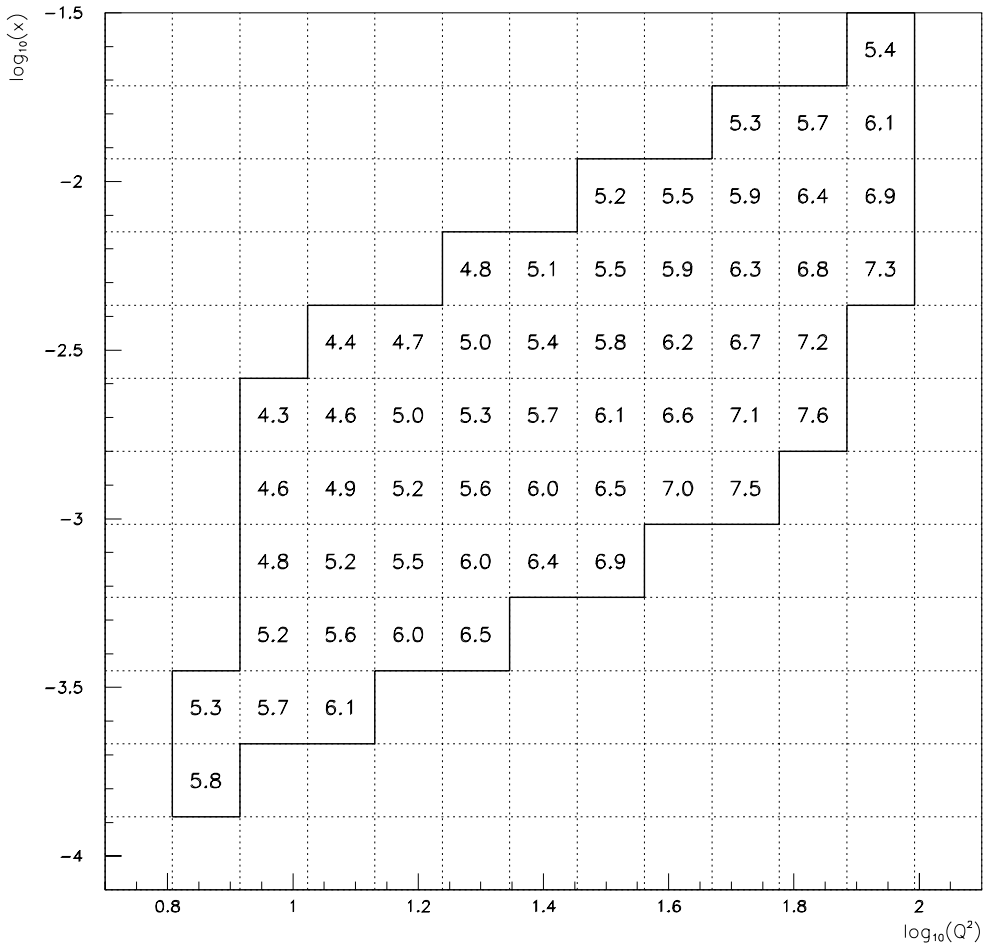

Figure 7.1: Value of the cut-off (in GeV) in the parton pair invariant mass (m_{ij}) as implemented in LEPTO for the kinematic region of the low Q^2 data sample.

In this section I will explain how this cut-off is implemented in the Monte Carlo used throughout this analysis (LEPTO 6.1). This will thus clarify what is meant by the samples of QPM, QCD Compton and BGF events from LEPTO as used in this analysis.

In LEPTO, the divergences in the Matrix Element are avoided by the requirement that the invariant mass m_{ij} of any pair of partons in the final state, including the proton remnant, must satisfy the relation $m_{ij}^2 \geq y_{cut} W^2$. The value of y_{cut} is chosen in order to include as much of the phase space as possible without getting too close to the divergent regions. The most effective way of achieving this is to parameterize the divergence limit, at which the rate of $O(\alpha_s)$ processes exceeeds the total cross-section, as a function of x and Q^2 and define the cut-off in m_{ij} in terms of this. So, the parameter y_{cut} is chosen to be a smoothly varying function defined as:

$$y_{cut}(x, Q^2) = \frac{\{D(x, Q^2) + C\}^2}{W^2} \tag{7.1}$$

where $D(x, Q^2)$ is the parameterization of the divergence limit and C is a constant, chosen in this analysis to be 2 GeV.

Figure 7.1 shows the variation of the value of the cut-off (in GeV) in the invariant mass m_{ij} across the kinematic region of the low Q^2 data sample, where y_{cut} is defined according to equation 7.1. It can be seen that it varies smoothly between about 4 GeV and 7.5 GeV in this region.

7.3 Energy flow at the Parton Level

At the parton level, ignoring parton showers (see section 2.8), the QPM process contains only the scattered quark and the proton remnant in the final state. In contrast, for both QCD Compton and BGF the final state consists of two partons and the proton remnant. Therefore we expect to see significant differences at the parton level in the topology of the QPM events compared to that of the two $O(\alpha_s)$ processes. Differences between QCD Compton and BGF are expected only in the ϕ distributions of the partons in the HCMS [34].

Figures 7.2*a–d* show the average energy flow per event at the partonic level as a function of $\cos\theta^*$ in the HCMS for each of the three processes (QPM, QCD Compton and BGF) as predicted by the LEPTO event generator. In each case,

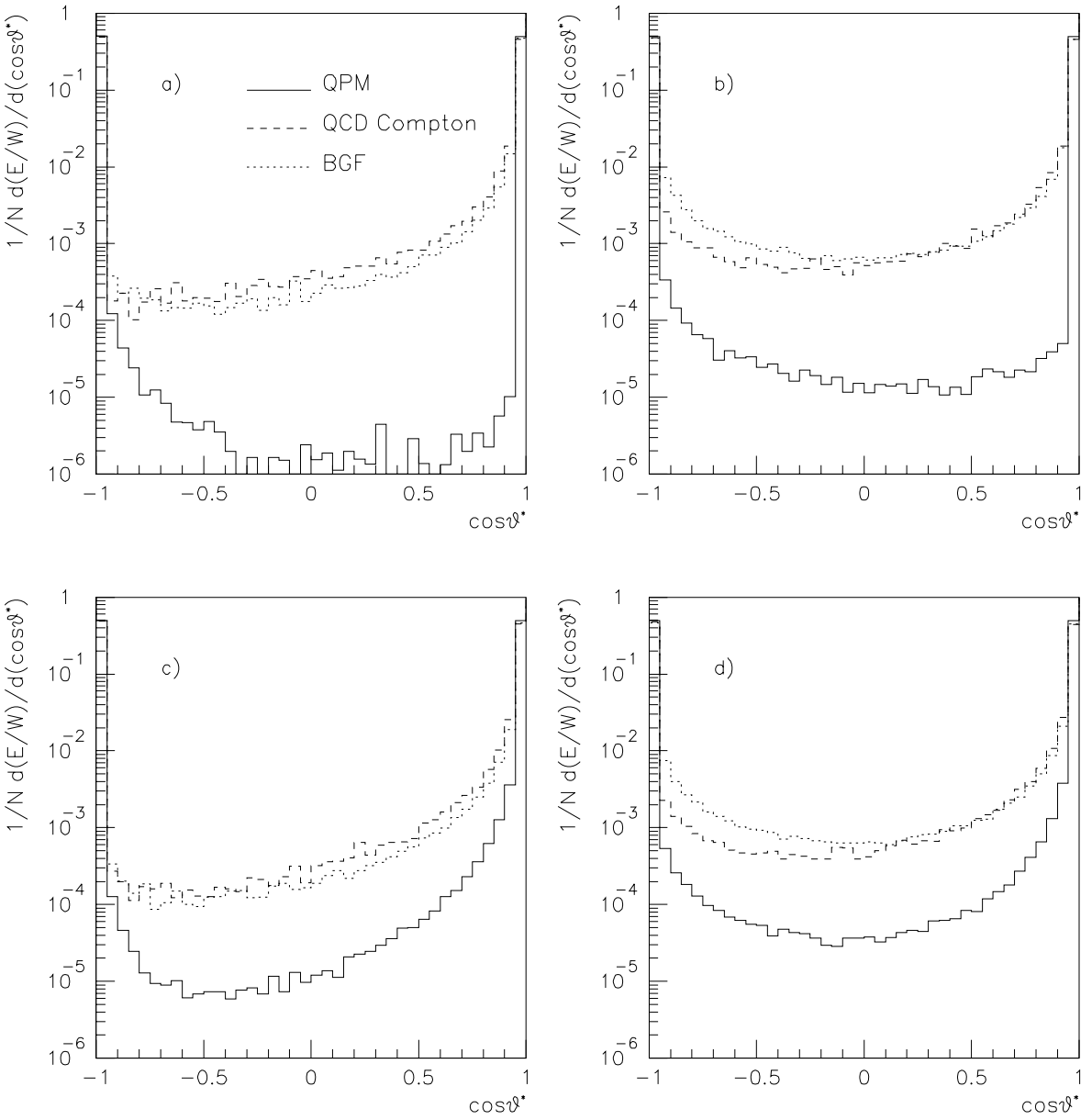

Figure 7.2: Mean energy flow per event at the parton level as a function of $\cos\theta^*$, expressed as a fraction of the total available energy, W, for: a) LEPTO ME only; b) LEPTO ME with initial state parton showers; c) LEPTO ME with final state parton showers; d) LEPTO ME with all parton showers. In each case, the predictions for QPM, QCD Compton and BGF are shown separately, according to the key in figure a)

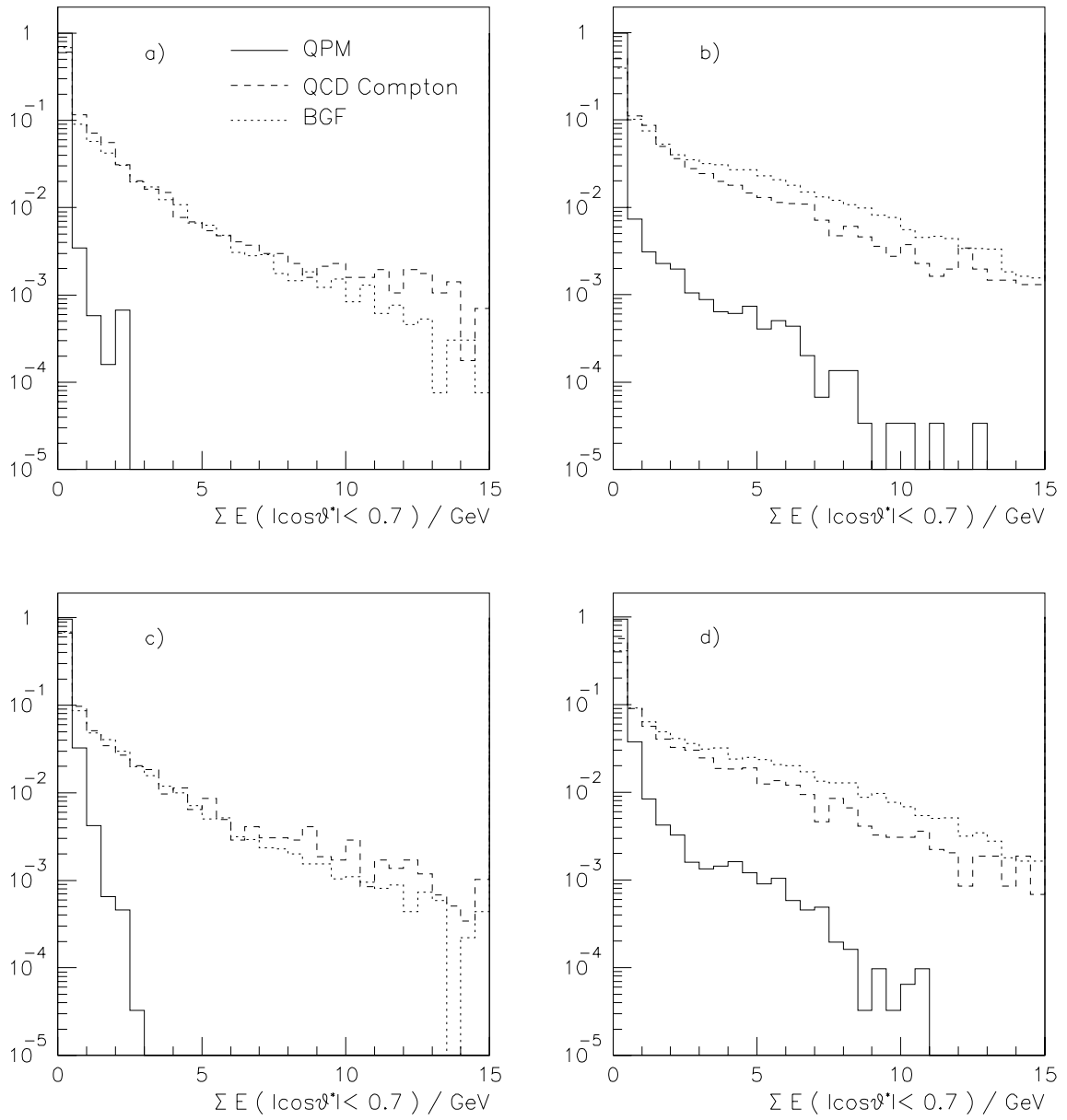

Figure 7.3: Total energy per event in the region $|\cos\theta^*| < 0.7$ at the parton level for: a) LEPTO ME only; b) LEPTO ME with initial state parton showers; c) LEPTO ME with final state parton showers; d) LEPTO ME with all parton showers. In each case, the predictions for QPM, QCD Compton and BGF are shown separately, according to the key in figure a)

the energy is expressed as a fraction of the total available energy in the event, W (calculated from the scattered electron 4-vector), as we are interested in the way in which the energy is distributed in an event, independent of its magnitude. No detector acceptance effects are included.

In figure 7.2*a*, parton showers are turned off, so only the partons from the hard sub-process and the proton remnant are included. As predicted, the distributions for QCD Compton and BGF are identical, as we are averaging over the azimuthal angle ϕ. Also, the topologies of the two $O(\alpha_s)$ processes are very different to the topology of a QPM event, purely as a result of the parton kinematics. Next we consider the effect of parton showers. Figure 7.2*b* shows the same distribution when initial state parton showers are included. As expected, the energy in the incident proton direction ($\cos\theta^* < 0$) is increased for all three processes but the fraction of the total available energy which is deposited in this region is about twice as much for BGF events as for QCD Compton events. This is a consequence of the fact that the probability that a gluon radiates a parton is greater than the probability that a quark radiates a gluon. Figure 7.2*c* shows the effect of including parton showers in the final state alone. This time the energy increases in the region $\cos\theta^* > 0$ in all three cases. The fraction of energy deposited in this region is slightly greater for QCD Compton events than for BGF events - the result of a qg final state compared to a $q\bar{q}$ final state. Finally, figure 7.2*d* shows the energy flow at the parton level when both initial state and final state parton showers are included.

Figures 7.3*a–d* show the total energy per event at the parton level in the region $|\cos\theta^*| < 0.7$. The chosen range in $\cos\theta^*$ is arbitrary, but lies between the struck quark and the proton remnant in the QPM model. Detector acceptance effects are not included. The predictions for QPM, QCD Compton and BGF are shown separately, and each distribution is normalized to the same number of events. In figure 7.3*a*, parton showers are turned off and figures 7.3*b* and 7.3*c* show the effect of including initial and final state parton showers respectively. In figure 7.3*d*, both initial and final state parton showers are included. It can be seen that the total energy per event in this region of $\cos\theta^*$ is typically larger for the two $O(\alpha_s)$ processes than for the QPM events but that the differences between QCD Compton and BGF events are very small.

7.4 Energy Flow at the Hadron Level

We can also study the same distributions after hadronization.

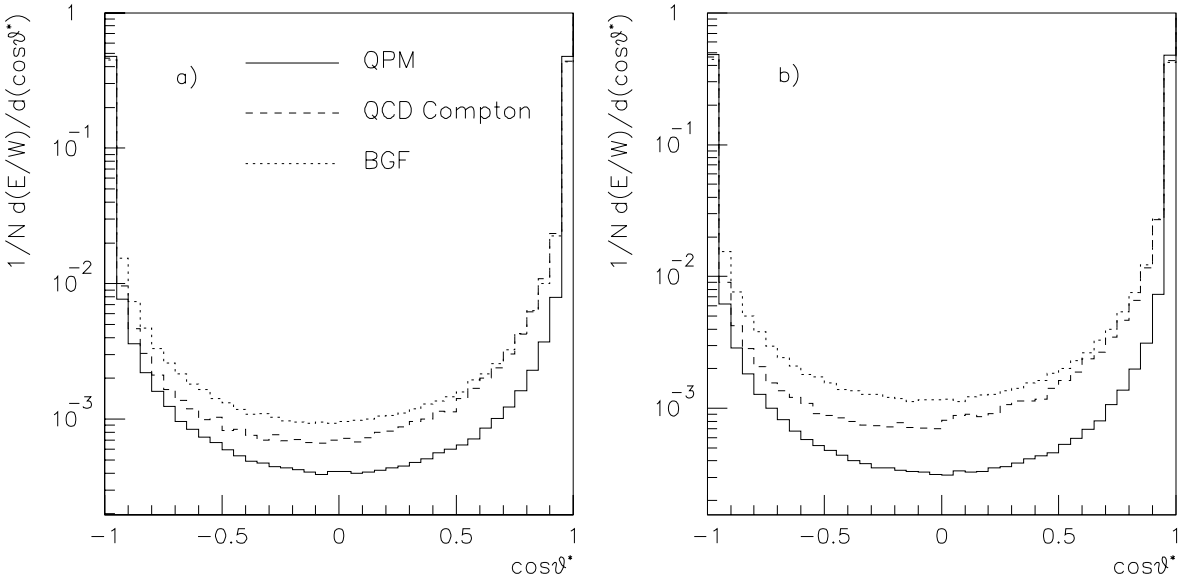

Figure 7.4: Mean energy flow per event after hadronization, expressed as a fraction of the total available energy W for a) matrix element only ; b) matrix element plus parton showers. In each case, the predictions for QPM, QCD Compton and BGF are shown separately, according to the key in figure a).

Figure 7.4 shows the average hadronic energy flow per event in the HCMS as a function of $\cos\theta^*$ for the same samples of QPM, QCD Compton and BGF events from LEPTO. Again, we express the energy as a fraction of W and detector effects are not included.

In figure 7.4*a*, all parton showers are turned off. The fraction of the total energy which is deposited in the central region of $\cos\theta^*$ is approximately twice as large for BGF events than for QCD Compton events. This is in striking contrast to the same distribution at the parton level (figure 7.2*a*) where there was no difference between BGF and QCD Compton. This effect is also visible in figure 7.4*b*, which shows the effect of including all parton showers and should be compared to figure 7.2*d* at the parton level.

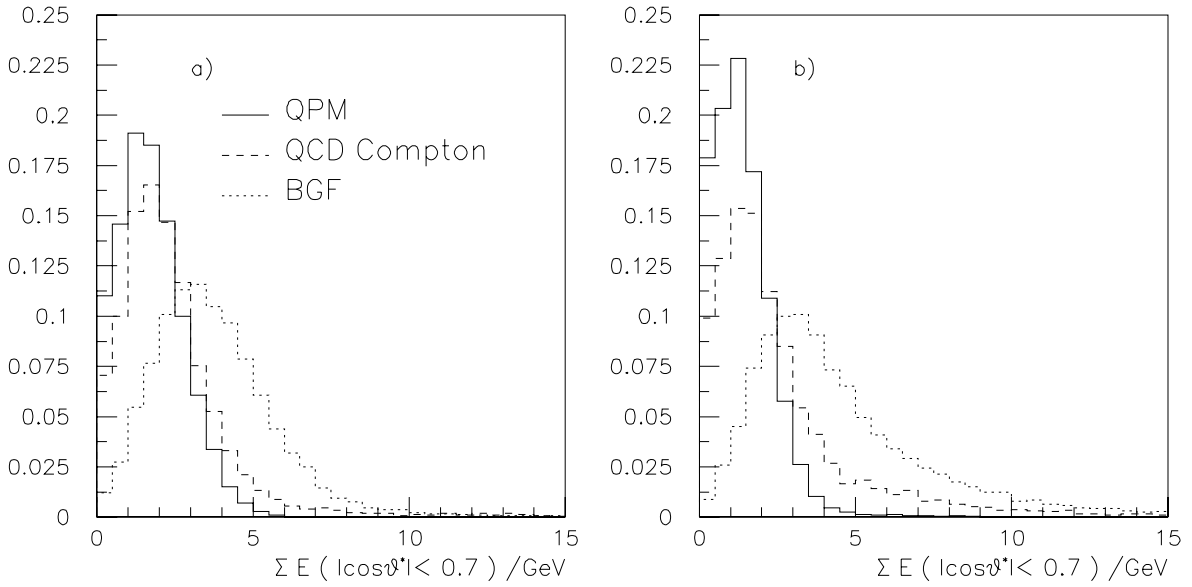

Figure 7.5: Total energy per event in the region $|\cos\theta^*| < 0.7$ at the hadron level for: a) LEPTO ME only; b) LEPTO ME with parton showers In each case, the predictions for QPM, QCD Compton and BGF are shown separately, according to the key in figure a)

Figures 7.5*a* and 7.5*b* show the total energy per event after hadronization in the region $|\cos\theta^*| < 0.7$ with and without parton showers respectively. These two figures should be compared to figures 7.3*a* and 7.3*d* at the parton level. The BGF events tend to have more energy in this region of $\cos\theta^*$ than either QPM or QCD Compton events, whether or not parton showers are included. Indeed after hadronization the mean energy in this region (including the effects of parton showers) is 4.4 GeV for BGF events compared to 2.5 GeV for QCD Compton and only 1.4 GeV for QPM events.

Thus, although QCD Compton and BGF were virtually indistinguishable on the parton level, after hadronization there are significant differences between the two. In other words, there is a difference in the details of the hadronization process for BGF and for QCD Compton events. The net results of this is more energy being produced in the central region of $\cos\theta^*$ for the BGF events. This effect can be understood in terms of the the colour force between partons.

7.5 The Colour Force

For both QPM and QCD Compton processes, the exchanged boson interacts with a quark inside the proton ('quark initiated' processes). This means that the proton remnant is left in a colour triplet (or anti-triplet) state, depending on whether the boson interacted with a quark or an anti-quark. To conserve colour therefore, the rest of the partonic system must be in a colour anti-triplet (or triplet state). In contrast, for BGF, a 'gluon initiated' process, the proton remnant is left in a colour octet (8) state and so the rest of the partonic system also forms a colour octet state. The colour $(8, 8)$ force is stronger than the colour $(3, \bar{3})$ force, by a factor of 9/4 (see appendix A). This means that during hadronization a larger fraction of the total available energy (W) is produced between the current system and the proton remnant for a BGF event than for either of the quark initiated processes.

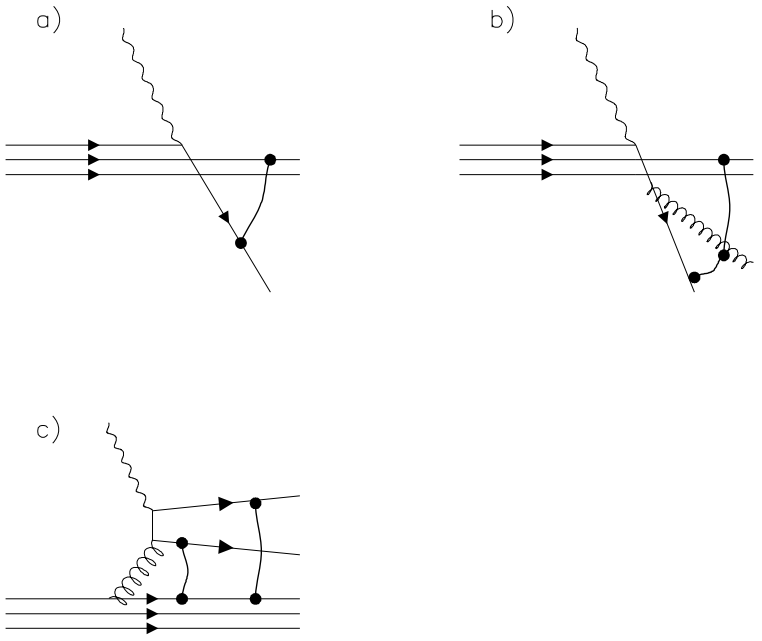

Figure 7.6: A schematic diagram showing the location of the strings in the LUND string model for a) QPM, b) QCD Compton and c) BGF events.

In the LEPTO Monte Carlo, this effect is modelled by the strings used in the hadronization process. Figure 7.6 shows the location of the strings for each of the three $O(\alpha_s)$ processes. For QPM, there is a single string between the struck quark and the proton remnant. For QCD Compton, there is also just one string, which

joins the struck quark to the proton remnant via the gluon. However, for BGF, there are two strings, joining both the quark and the anti-quark to the remnant. Thus, in both quark initiated processes there is only one string joining the current system to the proton remnant, but for BGF there are two. We therefore expect more of the energy to be produced between the current system and the proton remnant for BGF than for either quark initiated process. In particular, for fixed W we would expect to see approximately twice the amount of energy in this region for BGF than for QCD Compton, which as we have already seen is identical to BGF at the parton level. This is consistent with the observations made in section 7.4.

When parton showers are included, there are many strings joining the partons in the final state. However, they must still be equivalent to the simplistic picture described above, as the colour composition of the entire partonic state, excluding the proton remnant, must still be either a colour 3 or a colour 8 state, depending on the hard sub-process.

In QED, the radiation from a moving particle depends on the electric charge q_e and the deceleration $\ddot{x}$:

$$\text{radiation} \propto q_e^2 \times \ddot{x}$$

If we consider the QCD analogy, we have a moving colour charge q_c and:

$$\text{radiation} \propto q_c^2 \times \ddot{x}$$

As the initial deceleration is itself proportional to the total energy in the event, W, by looking at the energy flow as a fraction of W, we expect to see only the effect of the colour charge.

This explains the observations made in section 7.4. In figure 7.4, the energy flow was expressed as a fraction of W, and indeed we see about twice the fraction of energy in the central region for the BGF sample than for the QCD Compton events, even though they were identical at the parton level. It may also provide an explanation for the disagreement between data and LEPTO observed in chapter 6. In all cases, it was noticed that LEPTO described the data in the region of the current quark as predicted by the Quark Parton Model, but that there was more energy in the region between the proton remnant and the current system in the data than was predicted by LEPTO after standard detector simulation. The region in which the discrepancy was observed is precisely the region where

we expect to see the effect of the colour force. More specifically, by changing the proportion of quark and gluon processes in the LEPTO Monte Carlo, we could significantly change the amount of energy in this region.

7.6 Energy flow out of the Lepton Plane

The variable P^{out} was introduced in chapter 6, and defined as the amount of energy perpendicular to the lepton plane in the HCMS. As was shown in figure 6.7, the agreement between data and LEPTO with detector simulation was poor. However, we expect this variable to be sensitive to hadronization effects and, in particular, to depend on the energy between the proton remnant and the current system.

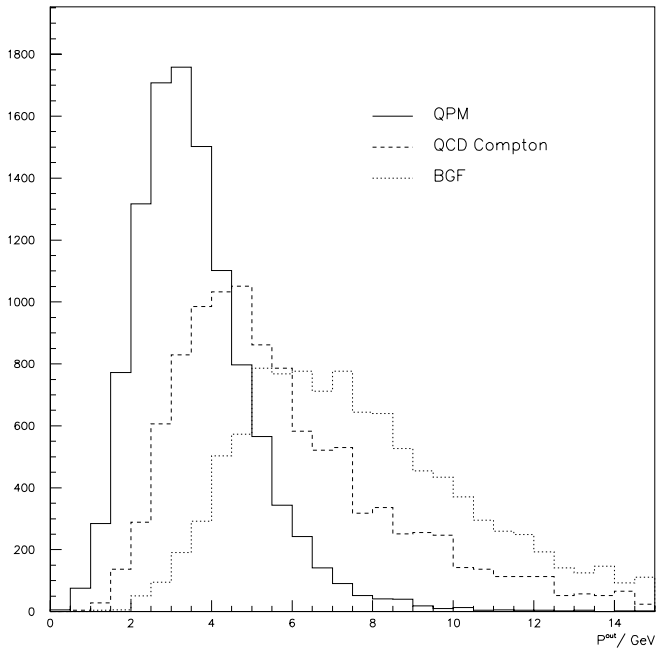

Figure 7.7: Distributions of P^{out} for QPM, QCD Compton and BGF events from LEPTO. In each case the distributions are normalized to the same number of events.

The P^{out} distributions for each of the three processes, QPM, QCD Compton and BGF, as predicted by LEPTO at the hadron level after detector simulation

are shown in figure 7.7. The difference between the distributions for the QPM and the QCD Compton events is a result of having one parton or two partons in the final state. However, as we have seen previously, at the parton level, when we average over ϕ, BGF and QCD Compton are virtually indistinguishable. At the hadron level, however, there is significantly more P^{out} per event for the BGF events. This is entirely consistent with the idea that for QCD Compton we are fragmenting a colour $(3, \bar{3})$ system in contrast to a colour $(8, 8)$ system for BGF.

As we move in x and Q^2, we expect the proportion of quark and gluon initiated processes to change. Thus, we expect a distribution which is different for quark and gluon initiated processes to reflect the change in the mixture of processes.

Figure 7.8 shows the distribution of P^{out} for the low Q^2 data sample in four bins of x. The prediction from LEPTO after hadronization and detector simulation is overlayed, normalized to the same number of events. The shaded histogram shows the contribution to this from BGF events in the Monte Carlo.

It can be clearly seen that the agreement between data and LEPTO improves with increasing x. However, there are more events in the data with a high value of P^{out} than LEPTO predicts, particularly in the lowest x bins (figures 7.8 a and b). The shaded histograms show that, as seen in figure 7.7, the large P^{out} events are mainly BGF events. These observations would seem to suggest that that there are more gluon initiated events in the data than LEPTO predicts, particularly at low x.

In addition, it can be observed that the P^{out} distribution in the data evolves with x. The mean and width of the distribution are larger in the lowest x bin than in the highest x bin. This is consistent with the contribution from gluon initiated processes decreasing with increasing x.

7.7 Conclusions

In this chapter it has been shown that there are differences in the hadronic final states of quark and gluon initiated processes. These observations are consistent with the differences which are to be expected on the basis of the different colour forces between the partons in the two cases.

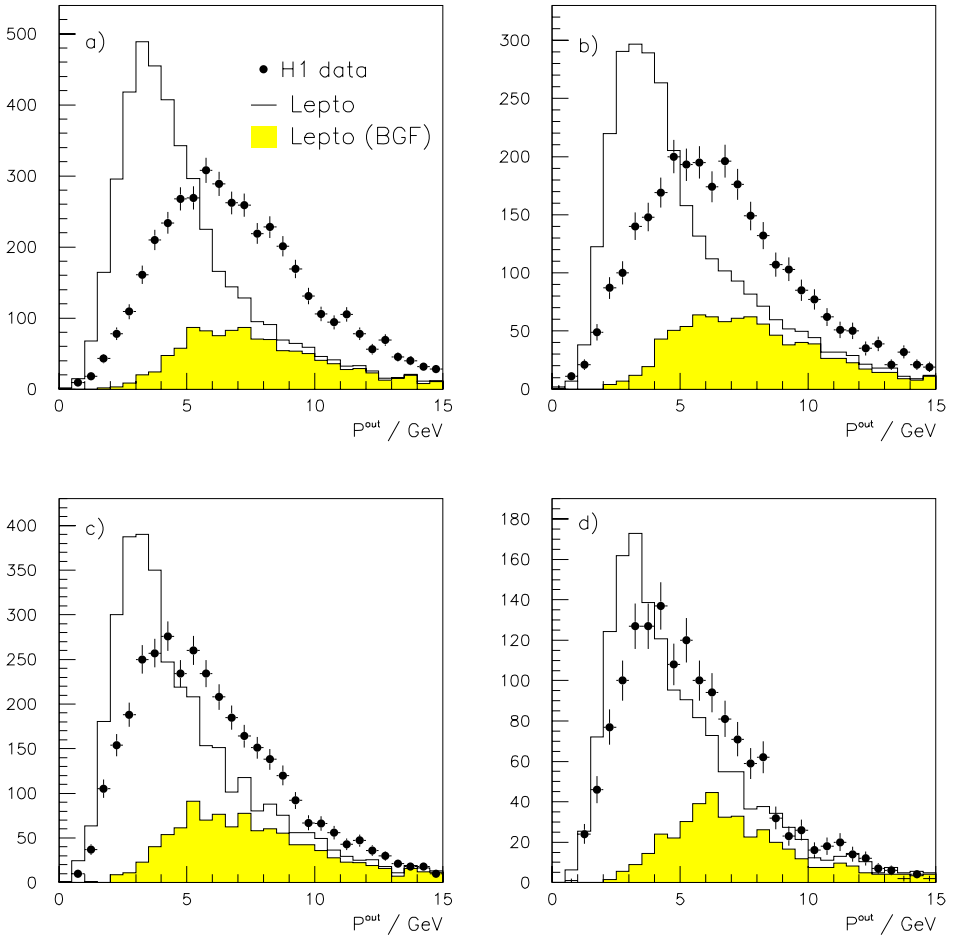

Figure 7.8: P^{out} in bins of x: a) $x < 1 \times 10^{-3}$; b) $1 \times 10^{-3} \leq x < 2 \times 10^{-3}$; c) $2 \times 10^{-3} \leq x < 5 \times 10^{-3}$; d) $x \geq 5 \times 10^{-3}$. In each case, the points are for the H1 data, the solid line is the prediction from LEPTO (normalized to the same number of events as the data) and the shaded histogram shows the contribution to the LEPTO prediction from BGF events.

It has also been shown qualitatively that the disagreement between the data and LEPTO in the region between the proton remnant and the current system could be due to the incorrect mixture of QPM, QCD Compton and BGF in the Monte Carlo. This will be pursued further in the following chapter.

Chapter 8

Measuring the Fraction of Gluon Initiated Processes at Low x

8.1 Introduction

It has been shown in chapter 7 that the different colour forces involved in quark and gluon initiated processes ($(3,\bar{3})$ and $(8,8)$ respectively) lead to observable differences in the hadronic final state. In particular it has been demonstrated that a larger fraction of the total available energy is deposited in the region between the proton remnant and the current system for gluon initiated than for quark initiated processes. The Monte Carlo prediction for the total energy flow in this region must therefore be very sensitive to the mixture of quark and gluon initiated processes which it contains.

In this chapter we use energy flow to measure the fraction of gluon initiated processes as a function of x and Q^2 in the low Q^2 data sample. Subsequently the result is used to re-weight events from the standard LEPTO Monte Carlo and to examine how the prediction for the energy flow changes. Finally, the contribution to the structure function F_2 from gluon initiated processes is calculated and the interpretation of this measurement in terms of the gluon content of the proton is discussed.

8.2 Method

This analysis uses the same bins in x and Q^2 as were used in the measurement by H1 of the proton structure function F_2 by the "electron method" [1] [25]. In the "electron method", the event kinematics are calculated from the scattered electron alone, and the same method of kinematic reconstruction is used in this analysis. There are 28 bins in total and figure 8.1 shows the location of the bins in x and Q^2. The bin size in x is chosen according to the resolution in x, which is determined from Monte Carlo with full detector simulation. In particular, for the electron method the bins at low y are excluded, as the resolution in x is poor (see section 2.2). For $x < 10^{-3}$ there are six bins per decade, equidistant in $\log x$, and for $x > 10^{-3}$ there are four bins per decade, equidistant in $\log x$. The Q^2 bin size is determined by the number of events in the data sample. The edges of the Q^2 bins are 7.50, 10.00, 13.37, 17.78, 23.71, 31.62, 42.17, 56.23 and 74.99 GeV^2.

In order to measure the fraction of gluon initiated processes in the low Q^2 data sample we need to use a property of the hadronic final state which is sensitive to the nature of the colour force. As we saw in chapter 7, the energy flow in the central region of $\cos\theta^*$, between the current and spectator systems, expressed as a fraction of the total available energy (W) satisfies this criterion. The range of $\cos\theta^*$ is chosen to be $|\cos\theta^*| < 0.7$; this choice is arbitrary, and account is taken of this in the systematic error on the measured fraction of processes.

The fractional energy flow in this range of $\cos\theta^*$ is parameterized as an nth order polynomial of orthogonal functions:

$$\frac{dE}{W\, d(\cos\theta^*)} = \sum_{l=0}^{n} a_l f_l(\cos\theta^*) \tag{8.1}$$

This expression is fitted to the measured energy flow distribution to obtain the coefficients a_l of the expansion. As the functions used in the expansion are orthogonal, the errors on the coefficients are uncorrelated.

In practice, a fifth order polynomial is sufficient to describe the observed energy flow as a function of $\cos\theta^*$. The functions f_i used in the expansion are

[1] The values of F_2 used in this analysis are those presented at the 1993 Moriond Conference, and are only preliminary. The final results have not been published at the time of writing this thesis.

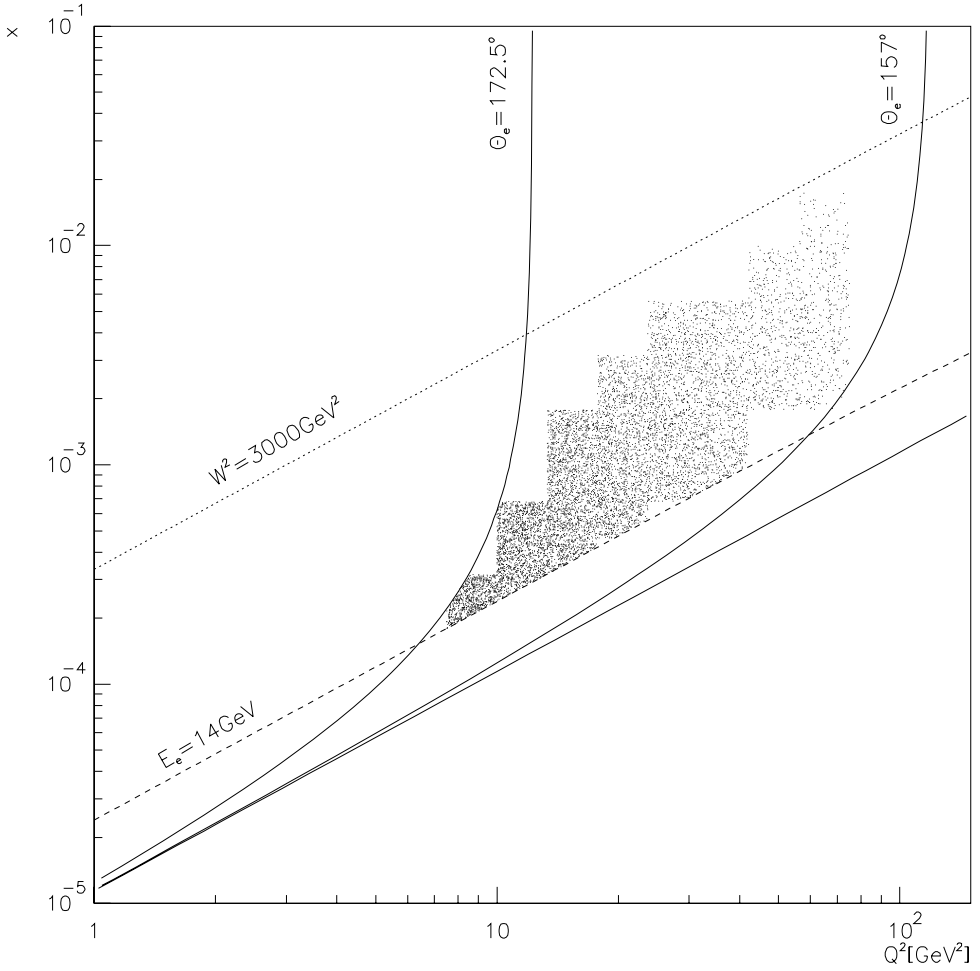

Figure 8.1: The x and Q^2 plane showing the bins used in this analysis.

i	f_i
0	1
1	$\frac{z}{c}$
2	$\frac{1}{2}(\frac{3}{c^2}z^2 - 1)$
3	$\frac{1}{2}(\frac{5}{c^3}z^3 - \frac{3}{c}z)$
4	$\frac{1}{8}(\frac{35}{c^4}z^4 - \frac{30}{c^2}z^2 + 3)$
5	$\frac{1}{8}(\frac{63}{c^5}z^5 - \frac{70}{c^3}z^3 + \frac{15}{c}z)$

Table 8.1: The terms in the polynomial 8.1 fitted to the energy flow in the region $|\cos\theta^*| < c$.

listed in table 8.1. The parameter c is introduced to represent the range in $\cos\theta^*$ over which the energy flow is fitted. The functions are Legendre polynomials with modified coefficients to ensure that they are orthogonal in the range of $\cos\theta^*$ under consideration.

The first term of this expansion, a_0, is proportional to the fraction of the total available energy which is deposited in the region $|\cos\theta^*| < 0.7$, the region between the current system and the proton remnant. From the results of chapter 7 we have shown that this depends on the colour charges of the partons from the hard sub-process and the proton remnant. Thus we expect a_0 to be sensitive to the nature of the colour force. The other coefficients in the polynomial depend only on the shape of the energy flow distribution in the chosen range of $\cos\theta^*$ which, as shall be demonstrated later on in this chapter, is determined by the detector acceptance. We have no evidence that the shape of the distribution alone would enable us to distinguish between two processes with identical parton kinematics but different colour forces.

We can test if a_0 is sensitive to the colour force by comparing the values for quark and gluon initiated processes. The polynomial 8.1 is fitted to the energy flow as a fraction of W in the range $|\cos\theta^*| < 0.7$ for QPM events, QCD Compton

events and BGF events (as predicted by LEPTO with full detector simulation) separately, in each of the (x,Q^2) bins. The energy flow distributions obtained from the data are fitted in the same way. The resulting values of a_0 are listed in table 8.2.

Figures 8.2 and 8.3 show the fitted distributions in two of the bins used in the analysis.

From table 8.2 it can be seen that throughout the kinematic range under consideration the value of a_0 for the sample of BGF events is higher than the value of a_0 for either of the quark initiated processes. Also, in general, the value of a_0 for the data is lower than the BGF prediction, and higher than either of the quark processes, which is as to be expected given that the data is a mixture of these processes, assuming that the hadronic final state of these processes is accurately modelled by LEPTO.

We can also calculate the ratio of a_0 for the BGF sample to a_0 for the QCD Compton sample, in each bin. These two processes are identical at the parton level (provided we average over ϕ) and so any observed differences at the hadronic level must be a consequence solely of the details of the hadronization. The results are shown in figure 8.4, where the bins are numbered consecutively according to their position in table 8.2. It can be seen that the ratio is constant with x and Q^2, even though, as can be seen from table 8.2, the values of a_0 are not. Also, the mean value of the ratio (1.87 ± 0.30) is consistent with the fact that theory predicts the colour (8,8) force to be about twice the strength of the colour ($3,\bar{3}$) force. This indicates that a_0 is indeed sensitive to the nature of the colour force.

It should be noted, however, that LEPTO uses one particular hadronization model, the Lund string model. We would expect the ratio of a_0 for the BGF sample to a_0 for the QCD Compton sample to be largely independent of the hadronization model if it depends only on the fundamental differences in the colour forces. However the absolute values of the a_0 coefficients for the processes may depend on the hadronization model used in the Monte Carlo. This question of sensitivity to the hadronization model is discussed in section 8.5.2.

The acceptance of the H1 detector in the HCMS changes with x and Q^2. This is illustrated in figure 8.5 which shows the energy flow as a fraction of W in the central region of $\cos\theta^*$ from LEPTO for four x bins at $Q^2 = 15\ GeV^2$. The open

Bins		LEPTO 6.1			
Q^2	x	QPM	QCD Compton	BGF	H1 Data
8.5	0.18×10^{-3}	0.354 ± 0.009	0.435 ± 0.032	0.946 ± 0.035	1.035 ± 0.033
	0.26×10^{-3}	0.398 ± 0.005	0.597 ± 0.019	1.138 ± 0.019	1.141 ± 0.017
12.0	0.26×10^{-3}	0.369 ± 0.007	0.530 ± 0.031	1.065 ± 0.029	1.027 ± 0.026
	0.40×10^{-3}	0.429 ± 0.005	0.625 ± 0.018	1.218 ± 0.018	1.203 ± 0.018
	0.60×10^{-3}	0.557 ± 0.006	0.936 ± 0.024	1.563 ± 0.021	1.475 ± 0.021
15.0	0.40×10^{-3}	0.382 ± 0.007	0.549 ± 0.020	1.131 ± 0.023	1.187 ± 0.026
	0.60×10^{-3}	0.455 ± 0.006	0.629 ± 0.020	1.287 ± 0.020	1.248 ± 0.020
	0.80×10^{-3}	0.598 ± 0.008	0.824 ± 0.029	1.764 ± 0.026	1.514 ± 0.027
	0.14×10^{-2}	0.694 ± 0.008	1.233 ± 0.035	2.029 ± 0.029	1.725 ± 0.028
20.0	0.60×10^{-3}	0.391 ± 0.008	0.518 ± 0.020	1.271 ± 0.026	1.109 ± 0.022
	0.80×10^{-3}	0.489 ± 0.008	0.698 ± 0.024	1.538 ± 0.028	1.333 ± 0.026
	0.14×10^{-2}	0.659 ± 0.009	1.061 ± 0.038	1.913 ± 0.028	1.810 ± 0.035
	0.26×10^{-2}	0.780 ± 0.011	1.424 ± 0.048	2.398 ± 0.040	1.761 ± 0.037
30.0	0.80×10^{-3}	0.413 ± 0.008	0.653 ± 0.028	1.297 ± 0.027	1.164 ± 0.026
	0.14×10^{-2}	0.621 ± 0.009	0.914 ± 0.026	1.717 ± 0.027	1.400 ± 0.027
	0.26×10^{-2}	0.753 ± 0.013	1.109 ± 0.036	2.160 ± 0.040	1.768 ± 0.041
	0.50×10^{-2}	0.865 ± 0.017	1.490 ± 0.061	2.423 ± 0.055	1.898 ± 0.053
40.0	0.80×10^{-3}	0.356 ± 0.014	0.455 ± 0.032	1.177 ± 0.040	1.051 ± 0.038
	0.14×10^{-2}	0.528 ± 0.011	0.820 ± 0.029	1.554 ± 0.028	1.282 ± 0.027
	0.26×10^{-2}	0.730 ± 0.014	1.216 ± 0.041	2.131 ± 0.043	1.753 ± 0.043
	0.50×10^{-2}	0.870 ± 0.018	1.724 ± 0.070	2.455 ± 0.056	1.734 ± 0.053
50.0	0.26×10^{-2}	0.681 ± 0.015	1.205 ± 0.046	2.122 ± 0.054	1.474 ± 0.037
	0.50×10^{-2}	0.804 ± 0.019	1.412 ± 0.057	2.320 ± 0.053	1.914 ± 0.058
	0.80×10^{-2}	0.992 ± 0.027	1.627 ± 0.004	2.403 ± 0.079	1.885 ± 0.070
65.0	0.26×10^{-2}	0.548 ± 0.018	0.951 ± 0.047	1.879 ± 0.055	1.512 ± 0.050
	0.50×10^{-2}	0.746 ± 0.021	1.659 ± 0.083	2.195 ± 0.053	1.591 ± 0.050
	0.80×10^{-2}	0.867 ± 0.027	1.762 ± 0.073	2.383 ± 0.076	1.971 ± 0.080
	0.014	1.088 ± 0.053	1.572 ± 0.012	3.070 ± 0.179	1.840 ± 0.106

Table 8.2: The coefficients $a_0 \times 10^3$ with their errors for QPM, QCD Compton and BGF events from LEPTO after full detector simulation, and for the low Q^2 data sample. The values are quoted at the bin centres in each case.

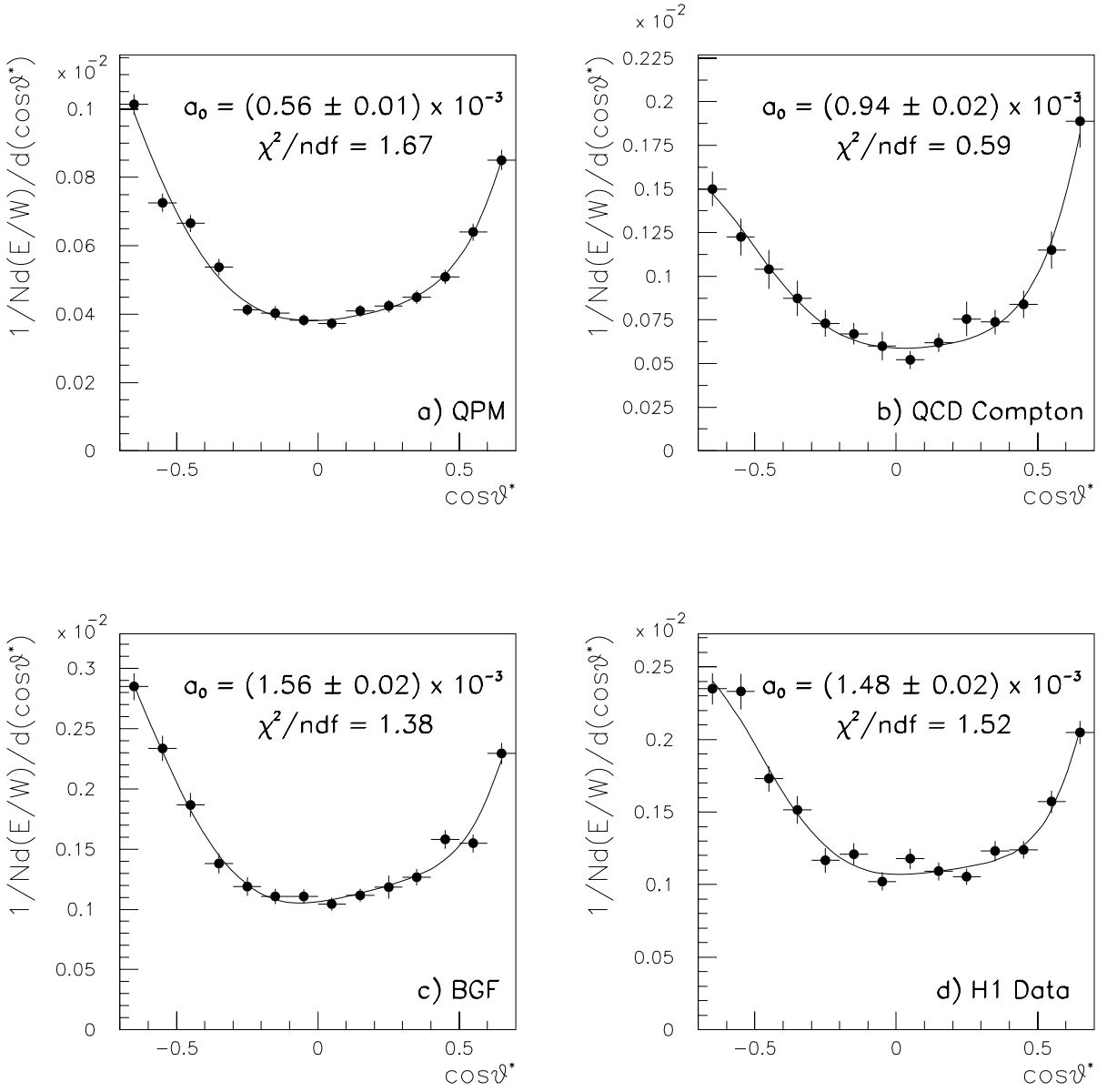

Figure 8.2: The fit to the energy flow distributions in the bin $x = 0.6 \times 10^{-3}$ and $Q^2 = 12\ GeV^2$ for the three subprocesses in LEPTO and the data sample. In each case the value of the coefficient a_0 and the χ^2 of the fit is shown.

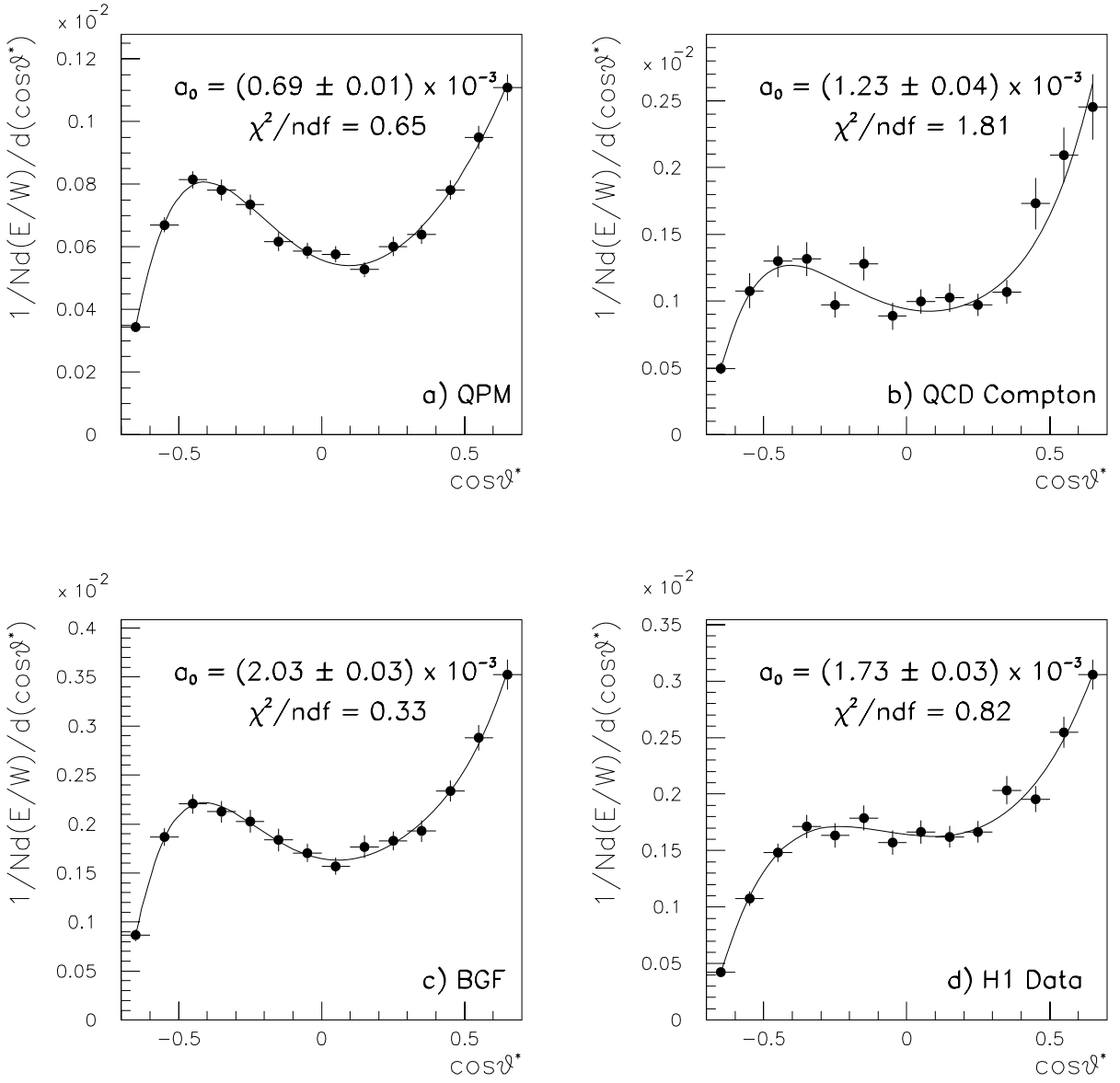

Figure 8.3: The fit to the energy flow distributions in the bin $x = 0.14 \times 10^{-2}$ and $Q^2 = 15\ GeV^2$ for the three subprocesses in LEPTO and the data sample. In each case the value of the coefficient a_0 and the χ^2 of the fit is shown.

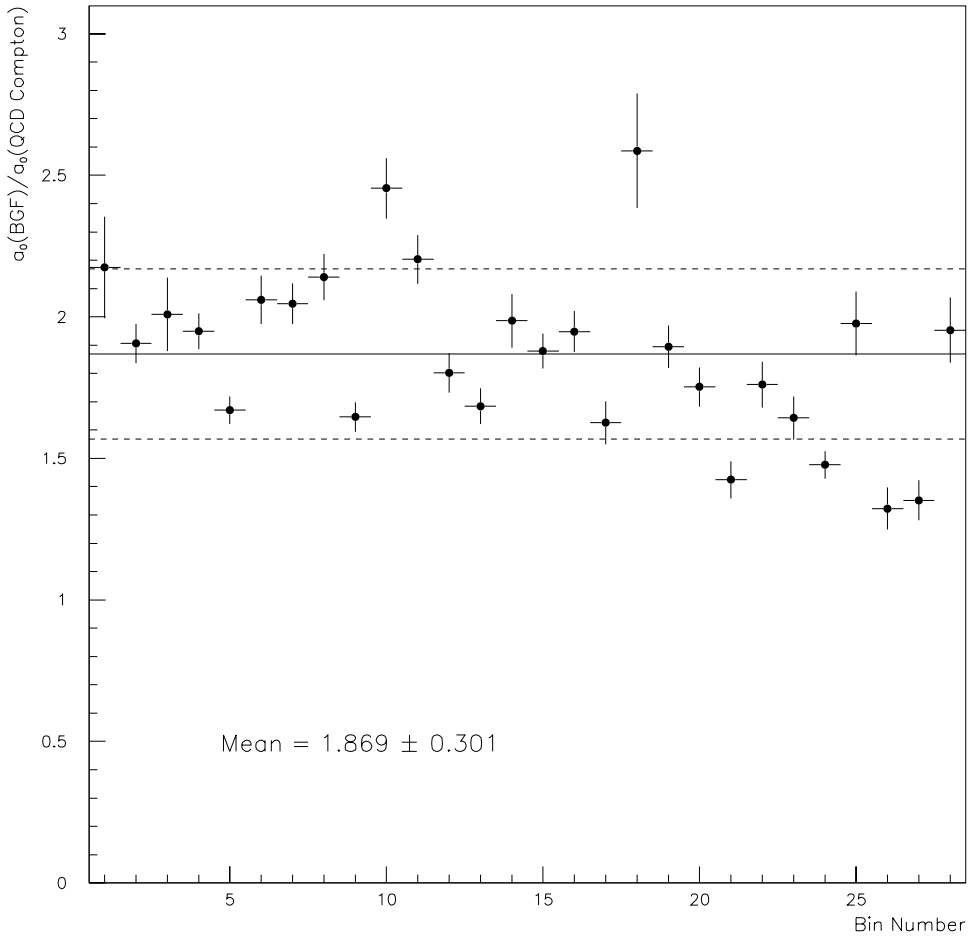

Figure 8.4: The ratio of a_0 for the sample of BGF events to a_0 for the QCD Compton events in each of the bins used in the analysis. The bins are numbered consecutively according to their position in table 7.2. The lines mark the mean value and one standard deviation from the mean.

points show the predicted energy flow after hadronization but before detector simulation and the solid points show the same energy flow with the detector acceptance included. The acceptance in the HCMS is different in all four cases, which leads to a change in the shape of the energy flow distribution. However in this analysis the a_0 coefficients for each of the processes are obtained from the Monte Carlo after a full-detector simulation has been performed and thus include the effects of detector acceptance. It is then possible to make direct comparisons between values of a_0 obtained from data and from Monte Carlo, assuming that the detector acceptance has been correctly modelled in the simulation.

We can now use the a_0 coefficients to measure f_g, the true fraction of gluon initiated processes, using the formula:

$$f_g = \frac{\epsilon_q(a_0^d - a_0^q)}{\epsilon_g a_0^g - \epsilon_q a_0^q - a_0^d(\epsilon_g - \epsilon_q)} \tag{8.2}$$

where the subscript q refers to quark initiated processes, g refers to gluon initiated processes and d refers to the measured quantity in the data. The derivation of this formula is outlined in appendix B.

The quantities ϵ_q and ϵ_g enable us to relate the measured fraction of gluon initiated processes in the selected low Q^2 data sample as a function of the reconstructed kinematics to the true fraction of gluon processes as a function of the true kinematics. They therefore include the efficiency of the data selection procedure and the effect of migrations between bins due to the resolution in reconstructing x and Q^2 from the scattered electron 4-vector. They are obtained from LEPTO in each (x,Q^2) bin and are defined as:

$$\epsilon = \frac{N_{meas}}{N_{gen}}$$

N_{meas} is the number of events from a sample of LEPTO events with full detector simulation which, in a given bin defined from the reconstructed kinematics, pass the event selection criteria. N_{gen} is the number of events generated by LEPTO in that (x,Q^2) bin, defined from the true kinematics, when no event selection procedure is applied. The same invariant mass cut-off is applied in throughout. The assumption is made that the migrations in the sample of LEPTO events with detector simulation are the same as in the data, which is reasonable given that the structure function used in the Monte Carlo, MRSH, is the best existing fit to the HERA F_2 measurements and that the x and Q^2 distributions from data are well reproduced [22].

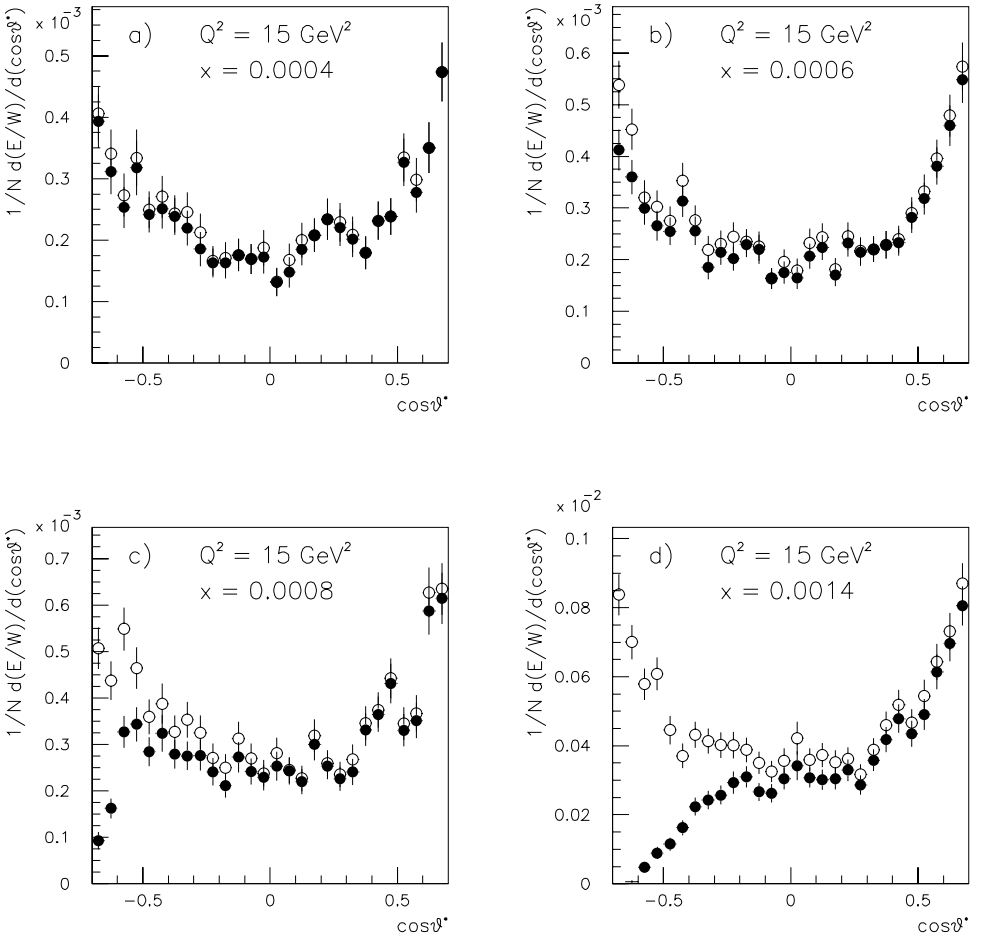

Figure 8.5: The energy flow as a fraction of W in the HCMS in the range $|\cos\theta^*| < 0.7$ for four bins of x and $Q^2 = 15\ GeV^2$. The open points show the energy flow without acceptance effects and the solid points show the effect of losing particles down the beam pipe.

The values of ϵ for each of the three subprocesses in LEPTO are shown in table 8.3.

The parameters a_0^q and ϵ_q are a combination of the parameters obtained separately from the sample of QPM and QCD Compton events:

$$a_0^q = (1-r)a_0^{QPM} + r a_0^{COM}$$

$$\epsilon_q = \frac{\epsilon_{QPM}\epsilon_{COM}}{(1-r)\epsilon_{COM} + r\epsilon_{QPM}}$$

where r is the fraction of the selected quark initiated events which are QCD Compton events in that (x,Q^2) bin. For a given invariant mass cut-off in the QCD Compton cross-section, r is well defined. In this analysis, r is extracted from the same sample of LEPTO events from which the a_0 coefficients are obtained.

8.3 Sources of Systematic Error

The sources of systematic error on the measurement of f_g are as follows:

- The error on the a_0 coefficients obtained from Monte Carlo and the error on the ϵ factors and the value of r.
- $\pm 2\%$ uncertainty in the BEMC electromagnetic scale. This will affect the migrations between bins and the reconstruction of 4-vectors in the HCMS, as the event kinematics and the boost vector are both calculated from the scattered electron.
- ± 2 mrad uncertainty in the measured θ of the scattered electron. This will have the same effect as the uncertainty in the electron energy.
- Choice of the range in $\cos\theta^*$ over which the fitting is performed. This is varied by ± 0.1 either side of the nominal choice of 0.7.
- A 5% uncertainty in the hadronic energy scale of the Liquid Argon Calorimeter. This leads to an uncertainty in the overall normalization of the measured values of f_g. By varying the value of the energy scale by $\pm$ 5% it was established that this normalization uncertainty was about 9%. This error is not included in the systematic error, but is quoted separately.

Bins		ϵ		
Q^2	x	QPM	QCD Compton	BGF
8.5	0.18×10^{-3}	0.166 ± 0.009	0.325 ± 0.052	0.307 ± 0.030
	0.26×10^{-3}	0.693 ± 0.022	1.211 ± 0.119	1.214 ± 0.071
12.0	0.26×10^{-3}	0.397 ± 0.018	0.687 ± 0.095	0.608 ± 0.050
	0.40×10^{-3}	0.977 ± 0.035	1.655 ± 0.174	1.661 ± 0.103
	0.60×10^{-3}	1.002 ± 0.034	1.428 ± 0.134	1.522 ± 0.092
15.0	0.40×10^{-3}	0.600 ± 0.029	1.162 ± 0.146	1.171 ± 0.092
	0.60×10^{-3}	0.992 ± 0.042	1.658 ± 0.197	1.855 ± 0.132
	0.80×10^{-3}	1.046 ± 0.046	1.391 ± 0.161	1.613 ± 0.110
	0.14×10^{-2}	1.041 ± 0.038	1.358 ± 0.126	1.805 ± 0.112
20.0	0.60×10^{-3}	0.785 ± 0.042	1.274 ± 0.168	1.366 ± 0.108
	0.80×10^{-3}	0.907 ± 0.048	1.649 ± 0.215	1.817 ± 0.147
	0.14×10^{-2}	1.061 ± 0.046	1.319 ± 0.136	1.982 ± 0.134
	0.26×10^{-2}	0.904 ± 0.040	1.301 ± 0.143	1.635 ± 0.116
30.0	0.80×10^{-3}	0.851 ± 0.052	1.625 ± 0.243	1.796 ± 0.162
	0.14×10^{-2}	0.989 ± 0.050	1.611 ± 0.186	1.924 ± 0.150
	0.26×10^{-2}	0.884 ± 0.046	1.287 ± 0.151	1.649 ± 0.131
	0.50×10^{-2}	0.968 ± 0.056	1.098 ± 0.131	1.533 ± 0.140
40.0	0.80×10^{-3}	0.372 ± 0.037	0.667 ± 0.122	0.597 ± 0.079
	0.14×10^{-2}	1.022 ± 0.062	1.510 ± 0.193	1.780 ± 0.155
	0.26×10^{-2}	0.942 ± 0.059	1.588 ± 0.201	2.119 ± 0.209
	0.50×10^{-2}	1.023 ± 0.065	1.582 ± 0.212	1.630 ± 0.157
50.0	0.26×10^{-2}	0.931 ± 0.069	2.014 ± 0.297	1.809 ± 0.186
	0.50×10^{-2}	0.970 ± 0.075	1.892 ± 0.290	1.960 ± 0.215
	0.80×10^{-2}	1.044 ± 0.088	1.484 ± 0.244	1.175 ± 0.150
65.0	0.26×10^{-2}	0.626 ± 0.062	1.145 ± 0.199	1.226 ± 0.154
	0.50×10^{-2}	1.079 ± 0.102	1.400 ± 0.219	2.189 ± 0.278
	0.80×10^{-2}	1.051 ± 0.104	1.719 ± 0.286	1.567 ± 0.211
	0.014	0.563 ± 0.064	0.951 ± 0.174	1.524 ± 0.303

Table 8.3: ϵ for each subprocess, as calculated from LEPTO.

The error arising from the uncertainty in a_0 for the data sample is quoted as the statistical error.

As it is unlikely that, for example, shifting the electron energy by +2% and by −2% will lead to an error on f_g of the same size but the opposite sign, due to the effect this would have on the boost to the HCMS for instance, the positive systematic errors and the negative systematic errors are added in quadrature separately.

A discussion of how other possible sources of error may affect the measurement of f_g and its interpretation is included after the presentation of the results, in section 8.5.

8.4 Results

Table 8.4 shows the measured values of f_g with the statistical and systematic errors.

Figure 8.6 shows f_g as a function of x in bins of Q^2 and figure 8.7 shows f_g as a function of Q^2 in bins of x. For each point, the inner error bar shows the size of the statistical error and total error is the statistical and systematic error added in quadrature.

The results show that the measured fraction of gluon initiated processes falls steeply with increasing x at fixed Q^2 and is approximately constant with Q^2 at fixed x. It is important to note that the method used to measure f_g does not constrain the results to lie between 0 and 1, although these are the physical limits. A value of f_g outside these limits implies that the data and the Monte Carlo are incompatible. However, in all bins the measured f_g is consistent with lying within the physical range, given the error on the measurement.

The method was also used to measure f_g for the full sample of LEPTO events after full detector simulation. The result is shown as a function of x in bins of Q^2 in figure 8.8 (the points) along with the true fraction of gluon initiated processes generated by LEPTO as a function of the true kinematics and with no selection procedure applied (the solid line). The good agreement between the two shows that the efficiency of the cuts and the migration between bins have been

Q^2	x	f_g	$\delta f_g(stat)$	$\delta f_g(sys^+)$	$\delta f_g(sys^-)$
8.5	0.18×10^{-3}	1.296	0.123	0.163	0.365
	0.26×10^{-3}	1.006	0.039	0.125	0.047
12.0	0.26×10^{-3}	0.919	0.053	0.148	0.058
	0.40×10^{-3}	0.968	0.036	0.080	0.116
	0.60×10^{-3}	0.871	0.030	0.040	0.161
15.0	0.40×10^{-3}	1.147	0.072	0.156	0.202
	0.60×10^{-3}	0.919	0.041	0.211	0.125
	0.80×10^{-3}	0.703	0.029	0.090	0.062
	0.14×10^{-2}	0.650	0.028	0.047	0.040
20.0	0.60×10^{-3}	0.727	0.033	0.046	0.130
	0.80×10^{-3}	0.683	0.034	0.095	0.046
	0.14×10^{-2}	0.853	0.047	0.035	0.174
	0.26×10^{-2}	0.441	0.025	0.064	0.075
30.0	0.80×10^{-3}	0.737	0.045	0.092	0.150
	0.14×10^{-2}	0.559	0.031	0.096	0.069
	0.26×10^{-2}	0.579	0.036	0.079	0.041
	0.50×10^{-2}	0.521	0.040	0.043	0.118
40.0	0.80×10^{-3}	0.796	0.058	0.056	0.190
	0.14×10^{-2}	0.609	0.034	0.137	0.097
	0.26×10^{-2}	0.540	0.040	0.052	0.147
	0.50×10^{-2}	0.374	0.037	0.082	0.090
50.0	0.26×10^{-2}	0.371	0.028	0.056	0.082
	0.50×10^{-2}	0.568	0.051	0.052	0.127
	0.80×10^{-2}	0.566	0.058	0.067	0.143
65.0	0.26×10^{-2}	0.578	0.049	0.062	0.087
	0.50×10^{-2}	0.294	0.039	0.082	0.107
	0.80×10^{-2}	0.576	0.076	0.118	0.163
	0.014	0.162	0.039	0.075	0.094

Table 8.4: Values of f_g with the associated statistical and systematic errors. The 9% uncertainty in the overall normalization is not included.

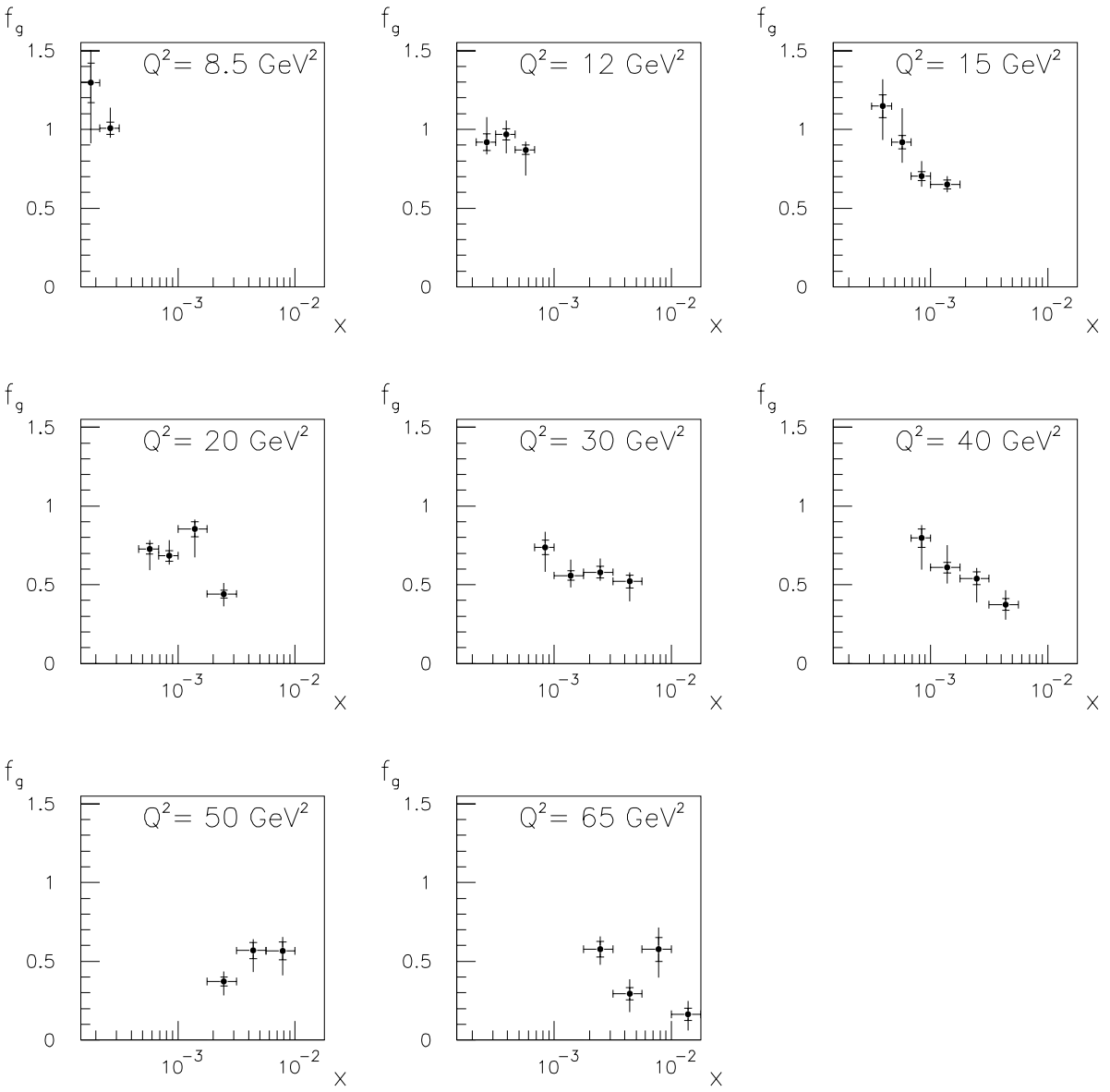

Figure 8.6: The measured f_g as a function of x in bins of Q^2. The inner error bar shows the statistical error and the total error is the statistical error and the systematic error added in quadrature. The 9% uncertainty in the overall normalization is not shown.

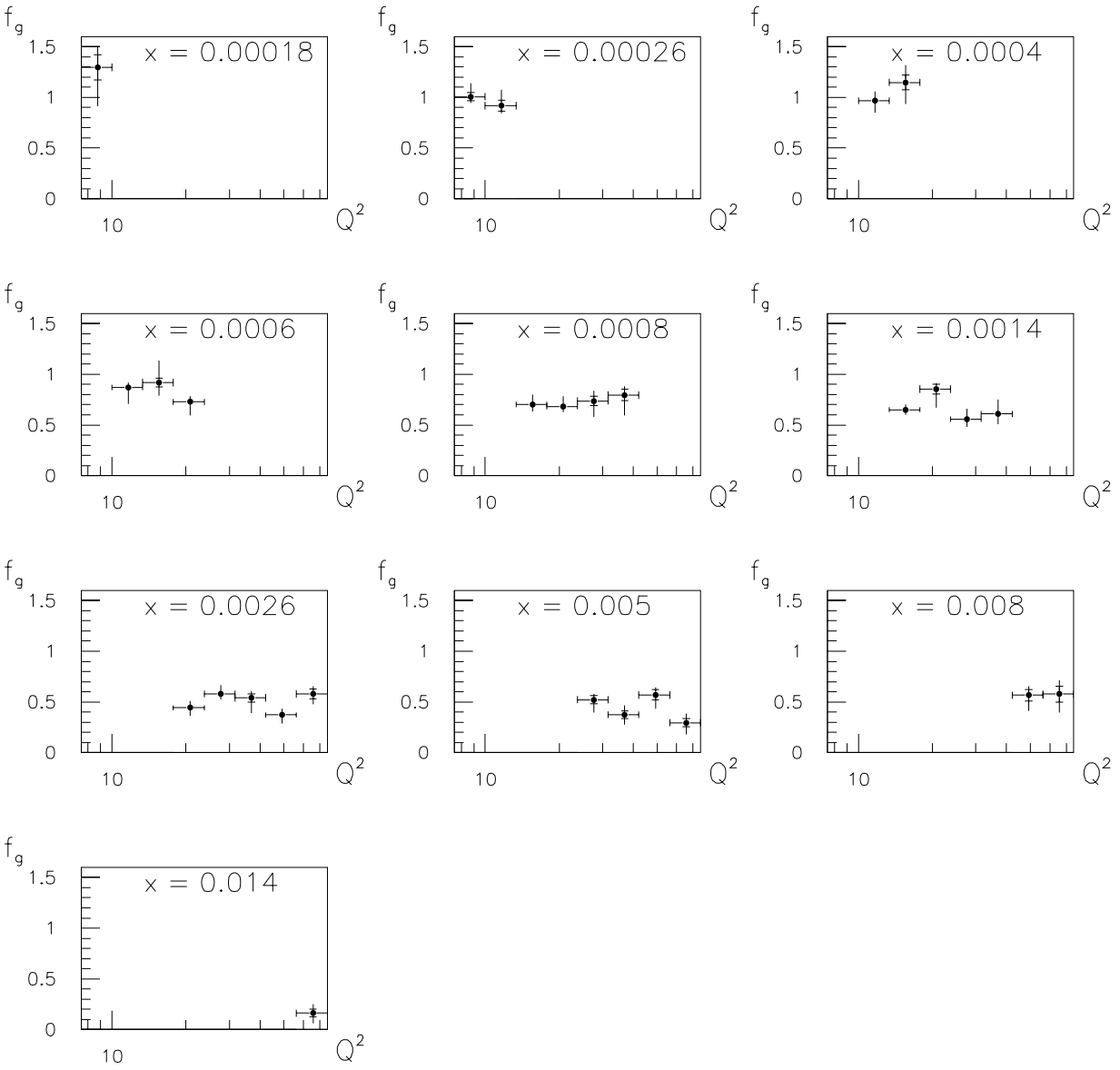

Figure 8.7: The measured f_g as a function of Q^2 in bins of x. The inner error bar shows the statistical error and the total error is the statistical error and the systematic error added in quadrature. The 9% uncertainty in the overall normalization is not shown.

correctly accounted for. On the whole, the fraction of gluon processes in LEPTO is less than the measured value of f_g in the data, particularly at low x, and is approximately constant with x at fixed Q^2.

8.5 Additional Considerations.

There are other possible sources of systematic error which are discussed here.

8.5.1 Cut-off

The cut-off was introduced in section 7.2. There it was explained that the definition of QCD Compton and BGF events in LEPTO depends on the choice of this cut-off. It is therefore necessary to consider how the choice of this cut-off affects the measurement of f_g.

Changing the value of the cut-off in the Monte Carlo has two effects. Firstly, the absolute number of QPM, QCD Compton and BGF events generated in an (x,Q^2) bin changes. Although this information is used in the calculation of the ϵ factors, as both N_{meas} and N_{gen} will change in the same way, we expect the values to be insensitive to changes in the cut-off. Secondly, the kinematics of the $O(\alpha_s)$ events generated in each bin will also change. As can be seen from table 8.2, a_0 is a function of x and Q^2. We measure the average value of a_0 over all the events in a bin so if we change the kinematics of the events in that bin we will subsequently also alter the mean value of a_0. To investigate the magnitude of this effect, the value of the cut-off was varied by $\pm$ 1 GeV from its nominal value, and it was found that the changes in a_0 varied from 5–20 %. If we assume that the ϵ factors are unaffected by changing the cut-off, this would result in a change in f_g by at maximum 15%.

However, rather than include the effect of changing the cut-off in the systematic error for f_g it is desirable to quote the results with a certain value for the cut-off. A sophisticated extraction of $G(x)$ from f_g takes into account the phase space for the $q\bar{q}$ pair, which in turn depends on the value of the invariant mass cut-off. Thus it is necessary only that the cut-off is a well-defined parameter.

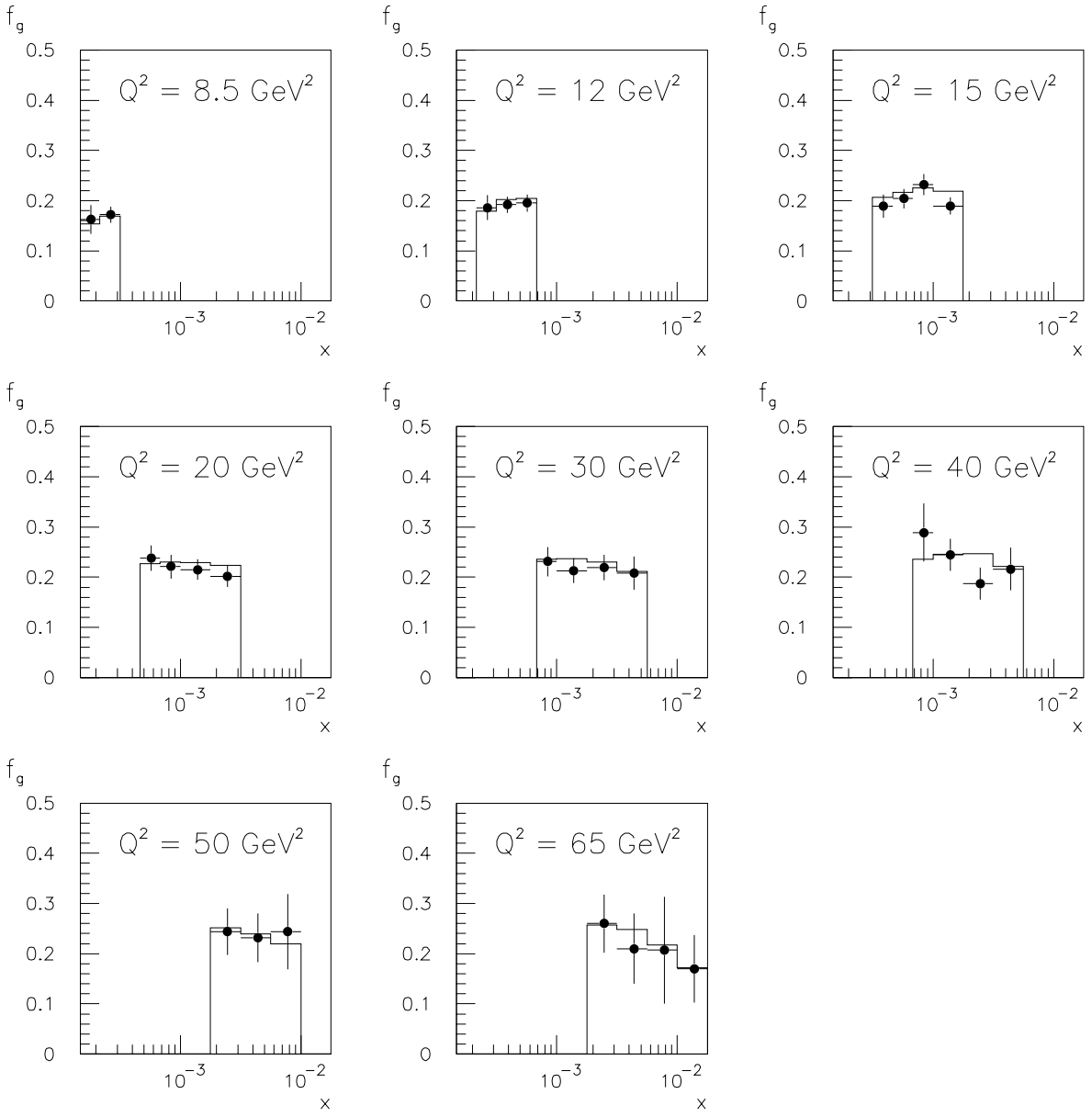

Figure 8.8: The points show the value of f_g, as a function of x at fixed Q^2, extracted from a sample of events from LEPTO with full detector simulation, and the solid line shows the true generated fraction of gluon initiated processes. The good agreement shows that the data selection efficiency and the migration between bins have been correctly accounted for.

8.5.2 Sensitivity to Hadronization Model

This analysis was based on the LEPTO Monte Carlo which uses the Lund string model for hadronization. The model has been seen to give a good description of certain properties of the DIS data (e.g jet rates [35] and energy-energy correlations [23]).

As mentioned before, we expect the ratio of the a_0 coefficients for quark and gluon processes to be insensitive to the hadronization model used by the the Monte Carlo, but the absolute values of a_0 may change. In order to test the sensitivity of the a_0 coefficients to the Monte Carlo model and to estimate the contribution to the systematic error on f_g arising from this it is desirable to repeat this analysis using other DIS Monte Carlos. In practice, however, this requires a detailed understanding of the Monte Carlo on both the parton and the hadron level. At present the systematic error on f_g from the Monte Carlo model used in the analysis has not been evaluated, and requires additional detailed studies.

8.5.3 Radiative corrections

The effect of radiating a photon from the incident or scattered electron has also not been included in the systematic error.

If the scattered electron radiates a photon after the interaction the photon will nearly always be clustered with the electron in the BEMC (owing to the coarse granularity of the device and the fact that the photon is preferentially radiated collinear to the electron) so the measured energy of the BEMC cluster will not be affected. If, on the other hand, a photon is radiated by the electron before the interaction, the incident electron will have a lower energy than the beam energy and the measured event kinematics will be wrong.

Thus, initial state radiation will cause migrations between (x,Q^2) bins, changing the values of ϵ. The boost to the HCMS will also be affected. As LEPTO does not include electroweak radiative corrections, it cannot be used to quantify this effect. However, although the radiative corrections can become large at low x, for the region $0.1 < y < 0.6$ in which f_g is calculated, they are known to be less than 10% [38]. Further Monte Carlo studies are necessary to study the effect

of radiative corrections in more detail.

8.6 Energy Flow in the Lab Frame

The measurement of f_g involves being able to reproduce the energy flow measured in the data in the central region of $\cos\theta^*$ in the HCMS by some mixture of quark and gluon processes as modelled by LEPTO with detector simulation. This region in the HCMS is equivalent to the forward region of the detector in the laboratory frame, where we have already shown (chapter 6) that there is a significant discrepancy between the measured energy flow and that predicted by LEPTO with the standard mixture of subprocesses. However, we have already observed that the fraction of gluon initiated processes in standard LEPTO is significantly lower than the measured f_g in the data, especially at low x, where the discrepancy in the energy flow between data and Monte Carlo is also largest (see figure 8.8). Thus if we reweight the events generated by LEPTO in each (x, Q^2) bin such that the fraction of BGF in the sample is equal to the measured value of f_g obtained from the data, we expect to see an improvement in the description of the energy flow in the forward region. Although this is to some extent an artifact of the way in which f_g has been measured, it is important to note that if it were impossible to describe the energy flow in this region by any mixture of the processes in LEPTO, the measured values of f_g would have been unphysical. As we have already seen, all the values of f_g are consistent with lying in the range 0 and 1, given the errors on the measurement.

Figure 8.9 shows the transverse energy flow per event as a function of pseudorapidity (η) in the laboratory frame for the same bins of (x, Q^2) as were shown in figure 6.3. The points show the energy flow for the data and the shaded histogram shows the prediction for LEPTO with the standard mixture of quark and gluon initiated processes after full detector simulation. The solid line shows the prediction from LEPTO after the events have been reweighted according to the measured fraction of gluon initiated processes, f_g.

It can be clearly seen that the reweighted LEPTO gives a better description of the transverse energy flow in the forward region of the detector than the standard version. This means that the energy flow in the forward region can be explained by LEPTO with a different, and yet still physical, mixture of quark and gluon

processes. The agreement between data and Monte Carlo is, however, still not perfect as the reweighted Monte Carlo tends to overestimate the energy flow in the current region (near $\eta = 0.$). The main reason for this is that the invariant mass cut-off used in the Monte Carlo defines the minimum energy in the current jet. These results would seem to suggest that although more gluon initiated processes are required to describe the forward transverse energy flow, the minimum value of the invariant mass of the $q\bar{q}$ pair in these events must be lower than the value of the cut-off used in LEPTO.

The same reweighting technique was applied to the distributions of P^{out} (equation 6.5) in these bins. The results can be seen in figure 8.10, where the points show the data, the shaded histogram the reweighted Monte Carlo and the solid line the standard LEPTO prediction. Again the reweighted Monte Carlo is able to give a significantly better description of the data than the standard version.

8.7 Forward Energy and Signatures for BFKL

The analysis described in this chapter has implications for the search for BFKL (see chapter 2) signatures in the H1 data. In particular, calculations have been performed [36, 37] which compare the transverse energy (E_t) in the forward region of the H1 detector at the partonic level for BFKL evolution and for standard DGLAP evolution. As might be expected, the k_t ordering in DGLAP evolution suppresses the E_t close to the proton remnant. It is therefore predicted that BFKL evolution will produce more E_t in the forward region of the H1 detector than is seen in a standard DGLAP Monte Carlo.

The observation of an excess of E_t in the forward region over the prediction from standard LEPTO (see figure 6.3), a Monte Carlo which is based on DGLAP evolution, may appear to be significant. However, as has been shown in this analysis, relating a calculation of E_t at the parton level to a prediction after hadronization requires knowledge of the mixture of quark and gluon initiated processes in the event sample. Each gluon initiated process produces approximately twice as much energy in the forward region of the detector after hadronization as a quark initiated process. It has been demonstrated that with a different mixture of quark and gluon initiated processes LEPTO, in conjunction with the standard detector simulation, is able to reproduce the observed transverse energy flow in

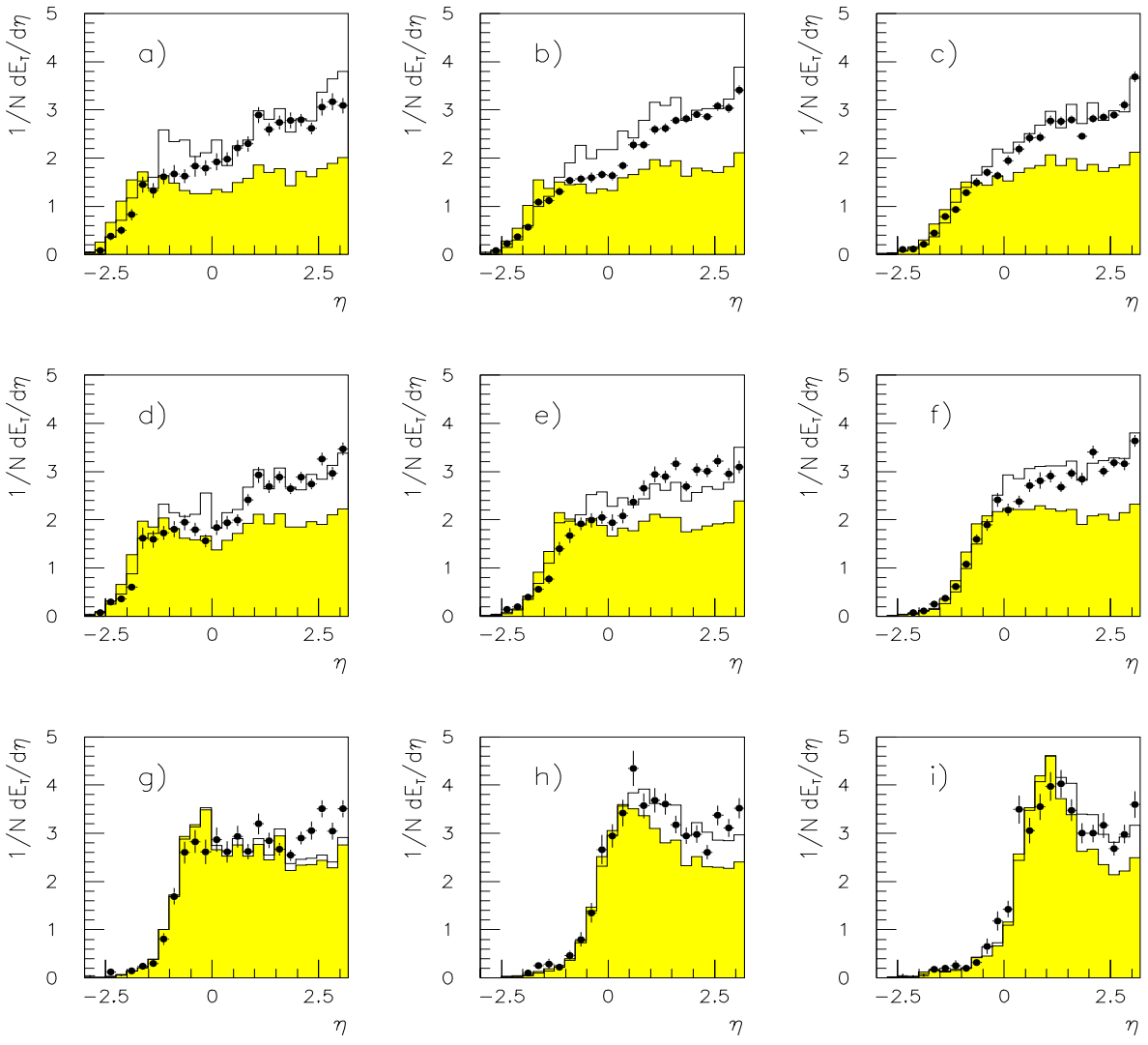

Figure 8.9: Mean transverse energy flow per event as a function of pseudorapidity, η, in the laboratory frame, for data (points), standard LEPTO (shaded histogram) and LEPTO reweighted according to the measured f_g in the following bins of x and Q^2:

a) $10.0 \leq Q^2 < 13.3$; $-3.7 \leq \log x < -3.5$; **b**) $10.0 \leq Q^2 < 13.3$; $-3.5 \leq \log x < -3.3$
c) $10.0 \leq Q^2 < 13.3$; $-3.3 \leq \log x < -3.2$; **d**) $17.8 \leq Q^2 < 23.7$; $-3.3 \leq \log x < -3.2$
e) $17.8 \leq Q^2 < 23.7$; $-3.2 \leq \log x < -3.0$; **f**) $17.8 \leq Q^2 < 23.7$; $-3.0 \leq \log x < -2.8$
g) $42.2 \leq Q^2 < 56.2$; $-2.8 \leq \log x < -2.5$; **h**) $42.2 \leq Q^2 < 56.2$; $-2.5 \leq \log x < -2.3$
i) $42.2 \leq Q^2 < 56.2$; $-2.3 \leq \log x < -2.0$

The points are for H1 data and the shaded histogram for LEPTO after full detector simulation. The solid line shows the predicted energy flow from LEPTO after re-weighting with the measured f_g.

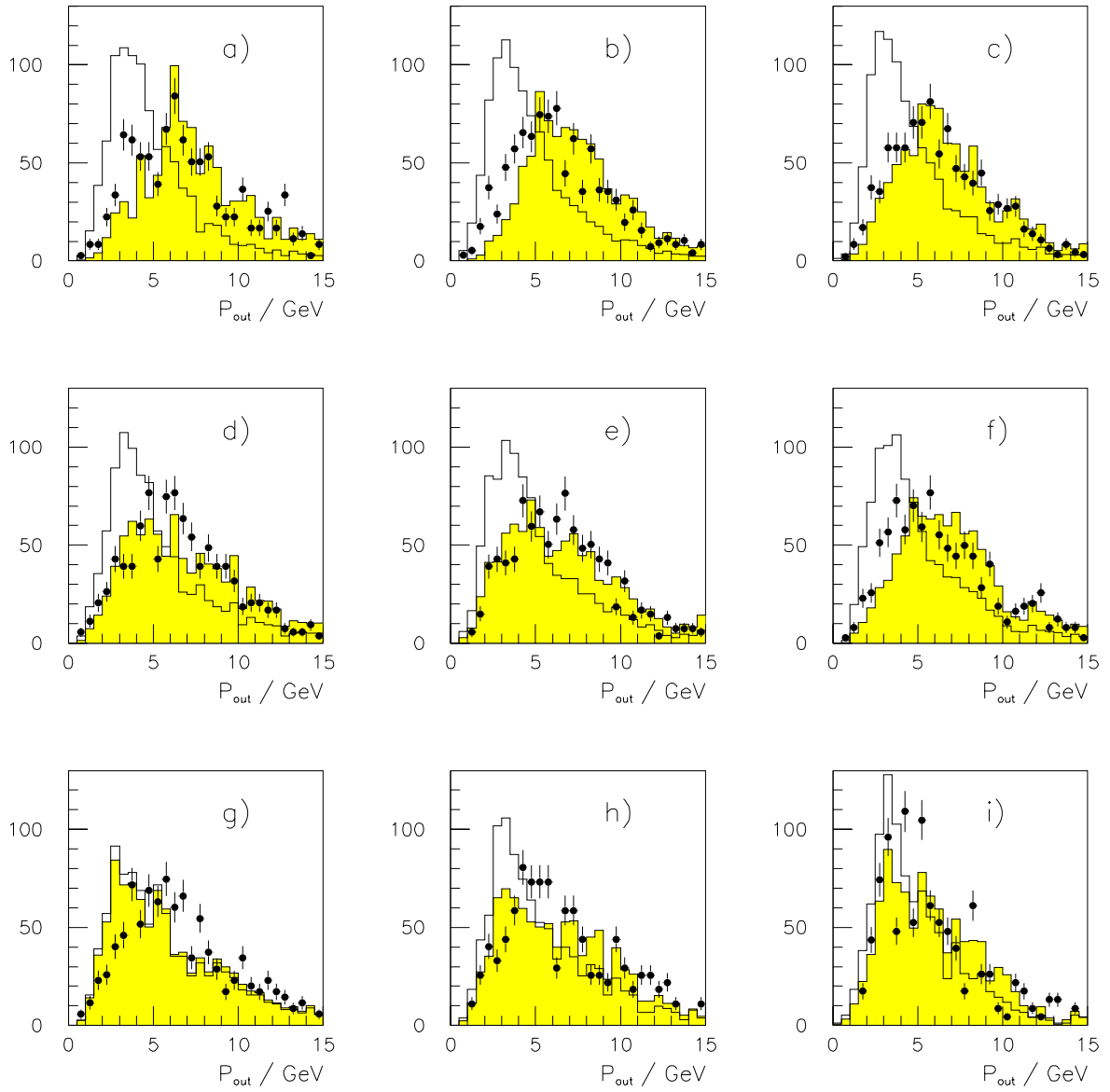

Figure 8.10: P^{out} for data (points), standard LEPTO (solid line) and LEPTO reweighted according to the measured f_g (shaded histogram) in the following bins:

a) $10.0 \leq Q^2 <$ 13.3 ; -3.7 $\leq \log x <$ -3.5 ; **b**) $10.0 \leq Q^2 <$ 13.3 ; -3.5 $\leq \log x <$ -3.3
c) $10.0 \leq Q^2 <$ 13.3 ; -3.3 $\leq \log x <$ -3.2 ; **d**) $17.8 \leq Q^2 <$ 23.7 ; -3.3 $\leq \log x <$ -3.2
e) $17.8 \leq Q^2 <$ 23.7 ; -3.2 $\leq \log x <$ -3.0 ; **f**) $17.8 \leq Q^2 <$ 23.7 ; -3.0 $\leq \log x <$ -2.8
g) $42.2 \leq Q^2 <$ 56.2 ; -2.8 $\leq \log x <$ -2.5 ; **h**) $42.2 \leq Q^2 <$ 56.2 ; -2.5 $\leq \log x <$ -2.3
i) $42.2 \leq Q^2 <$ 56.2 ; -2.3 $\leq \log x <$ -2.0

the forward region. This is not evidence against the existence of BFKL, as it is possible that many BFKL properties could be mimicked using DGLAP evolution and gluon distribution which rises steeply with decreasing x. Indeed the MRSH parton density functions which are based on DGLAP evolution are influenced by BFKL predictions for the x dependence of the gluon density ($G(x) \sim x^{-0.5}$). However, the results of this thesis show that it is at present difficult to find a distinct signature for BFKL from studying the transverse energy in the forward region of the H1 detector.

8.8 Extraction of $G(x)$ from f_g.

One possible approach to the extraction of $G(x)$ from the measurement of f_g has been investigated.

The first step in the method is to calculate the contribution to F_2 from gluon initiated processes:

$$F_2^g(x,Q^2) = f_g(x,Q^2) \times F_2(x,Q^2) \tag{8.3}$$

The F_2 values obtained from the 1993 data sample using the "electron" method are used to calculate F_2^g. The values of both F_2 and F_2^g along with their statistical and systematic errors are listed in table 8.5. The conservative assumption is made that the errors on f_g and on F_2 are independent, and they are added in quadrature to give the error on F_2^g.

Figure 8.11 shows both F_2 and F_2^g as a function of x in bins of Q^2 and figure 8.12 shows them a function of Q^2 in bins of x. It can be seen that F_2^g falls more steeply with increasing x than F_2, but that the variation with Q^2 is the same.

The $O(\alpha_s)$ leading $\log Q^2$ expression which relates F_2^g to the gluon density is:

$$F_2^g(x,Q^2) = \frac{\alpha_s}{2\pi}\log(\frac{Q^2}{\mu^2})\sum_q e_q^2 \int_x^1 \frac{dx_g}{x_g} g(x_g) P_{qg}\left(\frac{x}{x_g}\right) \tag{8.4}$$

which is just the gluonic piece of equation 2.36, where x_g is the fraction of the proton's momentum carried by the incoming gluon. The factorisation scale μ is chosen to be 4 GeV, as used in the MRS set of parton density functions. The running coupling constant α_s is parameterized as:

$$\alpha_s(Q^2) = \frac{12\pi}{(33-2n_f)\log(Q^2/\Lambda^2)} \tag{8.5}$$

Q^2	x	F_2	$\delta F_2(stat)$	$\delta F_2(sys)$	F_2^g	$\delta F_2^g(stat)$	$\delta F_2^g(sys)$
8.5	0.18×10^{-3}	1.356	0.059	0.223	1.757	0.186	$+0.364\ -0.573$
	0.26×10^{-3}	1.570	0.058	0.212	1.580	0.085	$+0.290\ -0.226$
12.0	0.26×10^{-3}	1.440	0.069	0.190	1.323	0.099	$+0.276\ -0.193$
	0.40×10^{-3}	1.331	0.054	0.178	1.289	0.071	$+0.203\ -0.231$
	0.60×10^{-3}	1.302	0.052	0.161	1.134	0.060	$+0.150\ -0.252$
15.0	0.40×10^{-3}	1.376	0.069	0.180	1.589	0.126	$+0.298\ -0.346$
	0.60×10^{-3}	1.251	0.061	0.109	1.150	0.076	$+0.282\ -0.186$
	0.80×10^{-3}	1.131	0.054	0.148	0.795	0.050	$+0.146\ -0.126$
	0.14×10^{-2}	1.068	0.040	0.155	0.694	0.039	$+0.112\ -0.109$
20.0	0.60×10^{-3}	1.437	0.077	0.154	1.045	0.074	$+0.130\ -0.218$
	0.80×10^{-3}	1.282	0.070	0.137	0.876	0.065	$+0.153\ -0.111$
	0.14×10^{-2}	1.005	0.048	0.133	0.857	0.063	$+0.119\ -0.209$
	0.26×10^{-2}	0.830	0.040	0.144	0.366	0.027	$+0.083\ -0.089$
30.0	0.80×10^{-3}	1.272	0.078	0.132	0.938	0.081	$+0.150\ -0.214$
	0.14×10^{-2}	1.093	0.057	0.118	0.611	0.046	$+0.124\ -0.100$
	0.26×10^{-2}	0.930	0.050	0.131	0.539	0.044	$+0.106\ -0.085$
	0.50×10^{-2}	0.856	0.050	0.137	0.446	0.043	$+0.080\ -0.124$
40.0	0.80×10^{-3}	1.594	0.117	0.130	1.268	0.131	$+0.141\ -0.321$
	0.14×10^{-2}	1.125	0.068	0.104	0.685	0.056	$+0.167\ -0.126$
	0.26×10^{-2}	1.024	0.062	0.118	0.553	0.053	$+0.083\ -0.163$
	0.50×10^{-2}	0.740	0.048	0.100	0.276	0.033	$+0.071\ -0.076$
50.0	0.26×10^{-2}	0.963	0.068	0.081	0.358	0.037	$+0.062\ -0.084$
	0.50×10^{-2}	0.700	0.054	0.098	0.398	0.047	$+0.067\ -0.105$
	0.80×10^{-2}	0.773	0.059	0.126	0.437	0.056	$+0.088\ -0.131$
65.0	0.26×10^{-2}	0.950	0.084	0.077	0.549	0.067	$+0.073\ -0.094$
	0.50×10^{-2}	0.835	0.068	0.105	0.245	0.034	$+0.075\ -0.095$
	0.80×10^{-2}	0.676	0.064	0.096	0.389	0.063	$+0.097\ -0.124$
	0.014	0.575	0.060	0.098	0.093	0.025	$+0.046\ -0.057$

Table 8.5: F_2 and F_2^g with statistical and systematic errors.

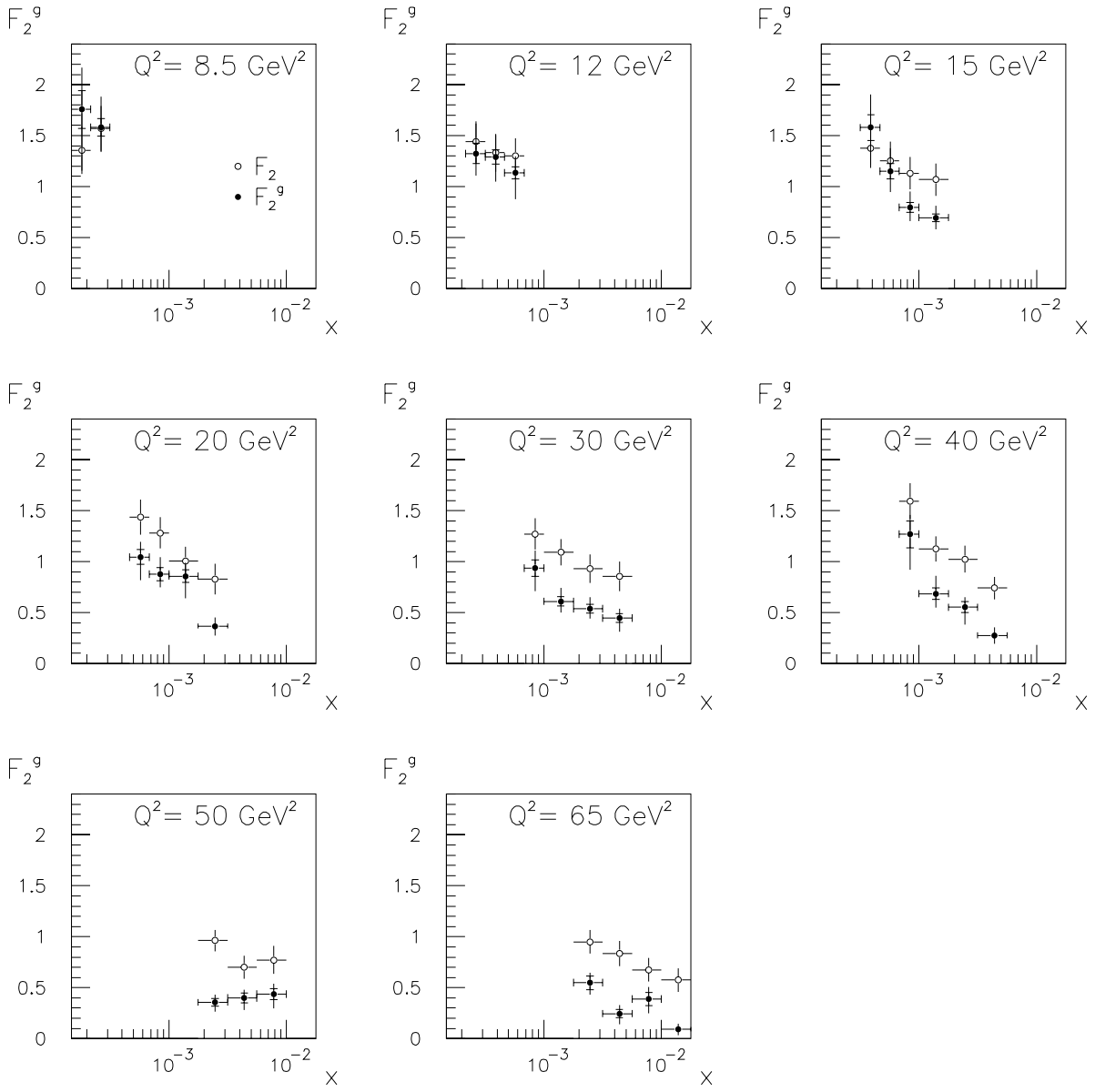

Figure 8.11: The solid points show F_2^g, the contribution to F_2 from gluon initiated processes, as a function of Q^2 in bins of x. The open circles show the values of F_2 in the same bins. In both cases, the inner error bars show the statistical errors and the total error is the result of adding the statistical and systematic errors in quadrature.

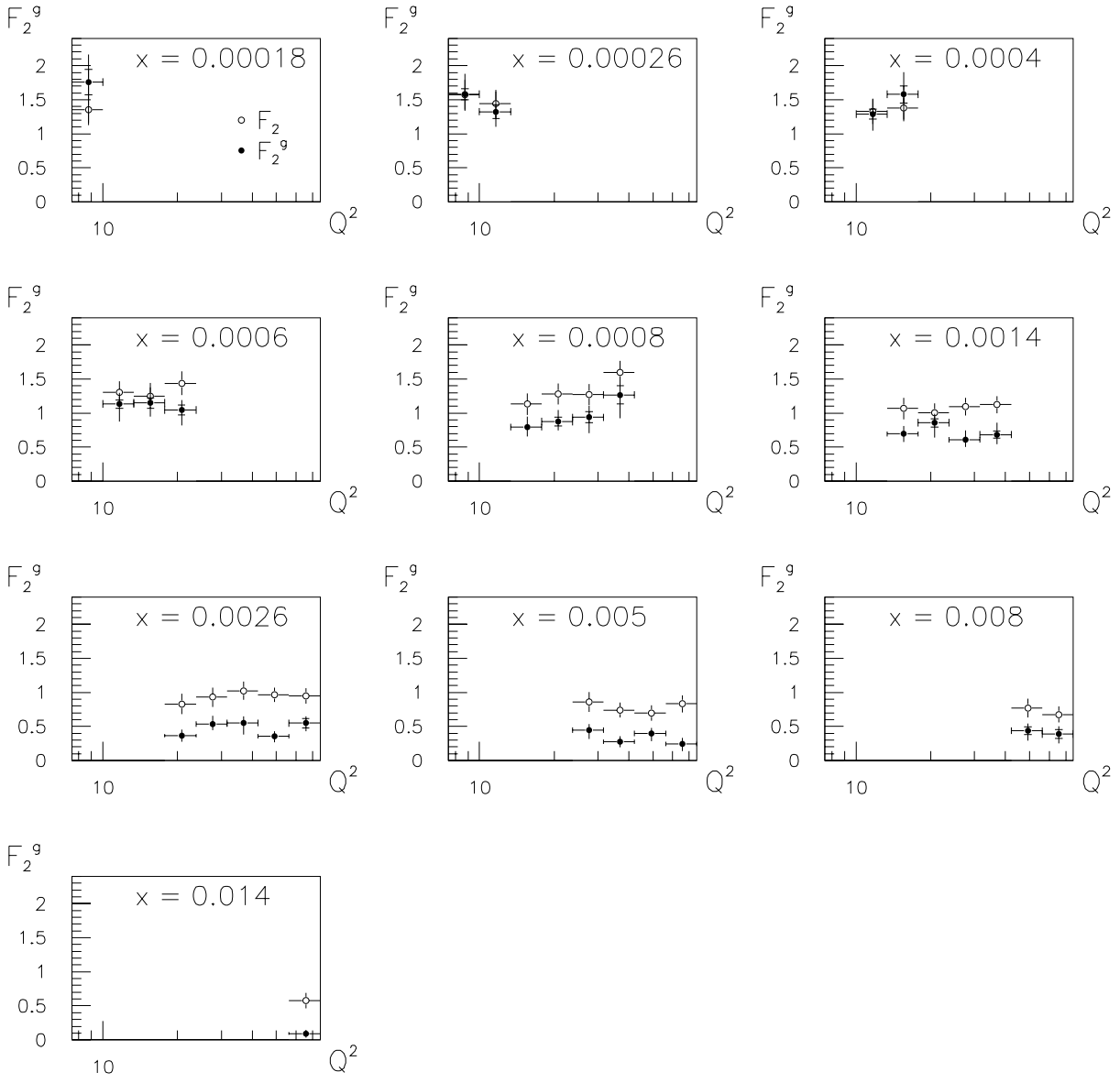

Figure 8.12: The solid points show F_2^g, the contribution to F_2 from gluon initiated processes, as a function of Q^2 in bins of x. The open circles show the values of F_2 in the same bins. In both cases, the inner error bars show the statistical errors and the total error is the result of adding the statistical and systematic errors in quadrature.

where Λ has the value 0.215 GeV for four quark flavours. $G(x_g)$ is assumed to have the form:

$$G(x_g) = x_g g(x_g) = A(1+\alpha)(2+\alpha)x_g^{\alpha}(1-x_g) \tag{8.6}$$

where A and α are two unknown parameters. The functional form is chosen such that A is equal to the total momentum fraction of the proton which is carried by the gluons. Substituting this expression in 8.4 then gives:

$$\begin{aligned}\frac{F_2^g}{C(Q^2)} &= \frac{3\alpha-\alpha^2-4}{(\alpha-1)(\alpha-2)(\alpha-3)}x^{\alpha} + \frac{\alpha^2-\alpha+2}{\alpha(\alpha-1)(\alpha-2)}x^{\alpha+1} \\ &\quad + \frac{x}{\alpha(\alpha-1)(\alpha-2)} - \frac{2x^2}{(\alpha-1)(\alpha-2)} + \frac{2x^3}{(\alpha-2)(\alpha-3)}\end{aligned}$$

where:

$$C(Q^2) = \frac{3A(1+\alpha)(2+\alpha)}{(33-2n_f)}\frac{\log(Q^2/\mu^2)}{\log(Q^2/\Lambda^2)}$$

The parameters A and α can now be determined by fitting this expression to the measured values of F_2^g.

In practice, we perform a global fit to all the F_2^g points in all the Q^2 bins. The error on each F_2^g is taken to be the maximum of the positive and negative systematic error added in quadrature with the statistical error.

The fit to the points in the eight Q^2 bins are shown in figure 8.13. The two unknown parameters in the formula for $G(x_g)$ (equation 8.6) are found to be:

$$\begin{aligned}A &= 0.520 \pm 0.041 \\ \alpha &= -0.771 \pm 0.054\end{aligned}$$

with a χ^2 per degree of freedom of 0.82.

The measured values of A and α are then used to construct the $O(\alpha_s)$ leading $\log Q^2$ gluon density $G(x_g)$ at $Q^2 = 4\ GeV^2$, according to equation 8.6. The shaded band in figure 8.14 shows the result. Also shown for comparison is a leading order parameterization of the gluon density from Glück, Reya and Vogt (GRV) [39] at the same Q^2. In this parameterization, the parton densities are evolved from a very small Q_0^2 ($0.3\ GeV^2$) using the double leading log approximation. The resulting gluon density rises steeply with x_g ($G(x_g) \sim x_g^{-0.4}$). In addition, the next-to-leading order (NLO) gluon distribution used in the MRSH set of parton density distributions is also shown, again at $Q^2 = 4\ GeV^2$.

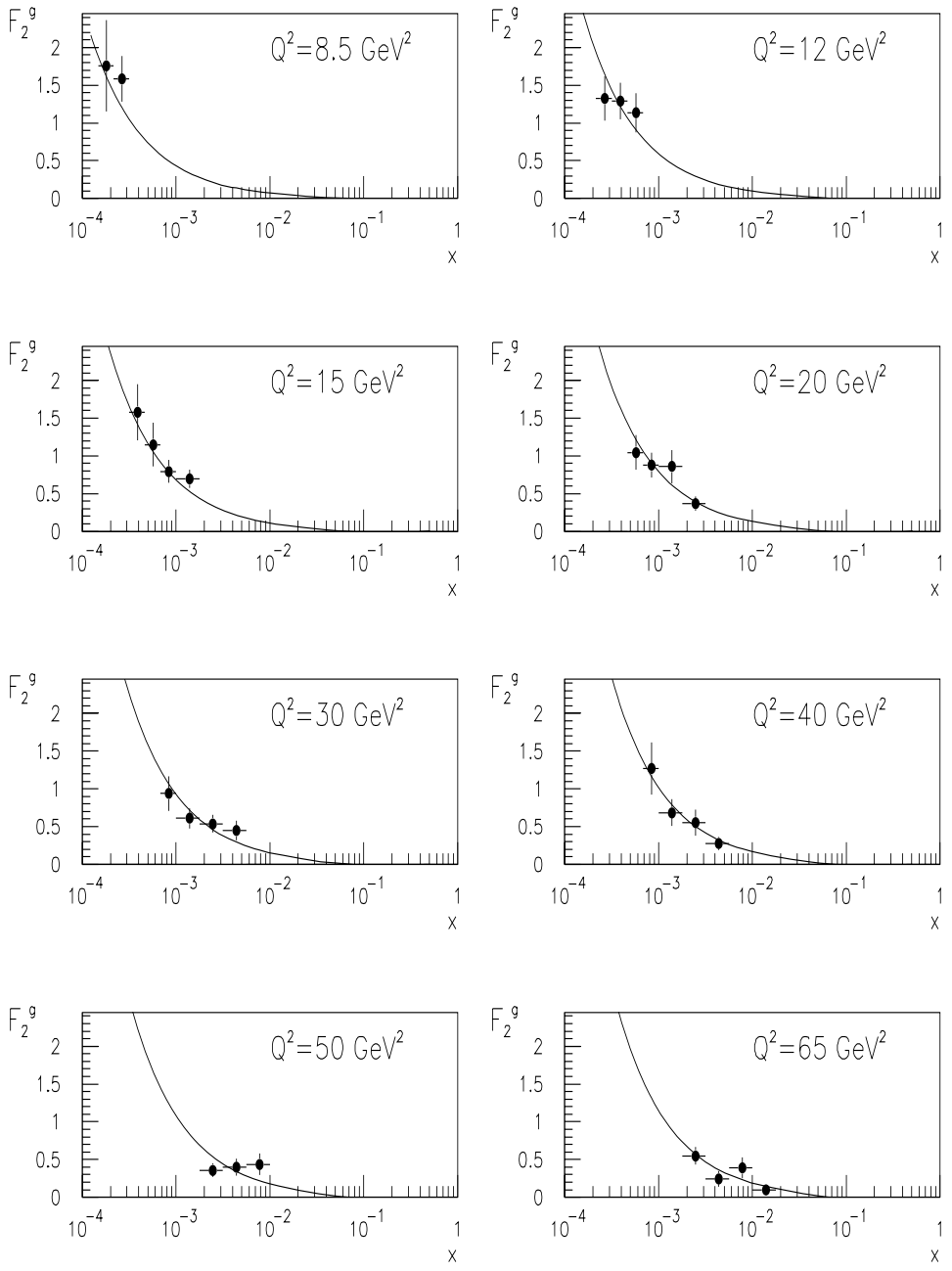

Figure 8.13: The result of fitting equation 7.7 to the measured values of F_2^g in bins of Q^2.

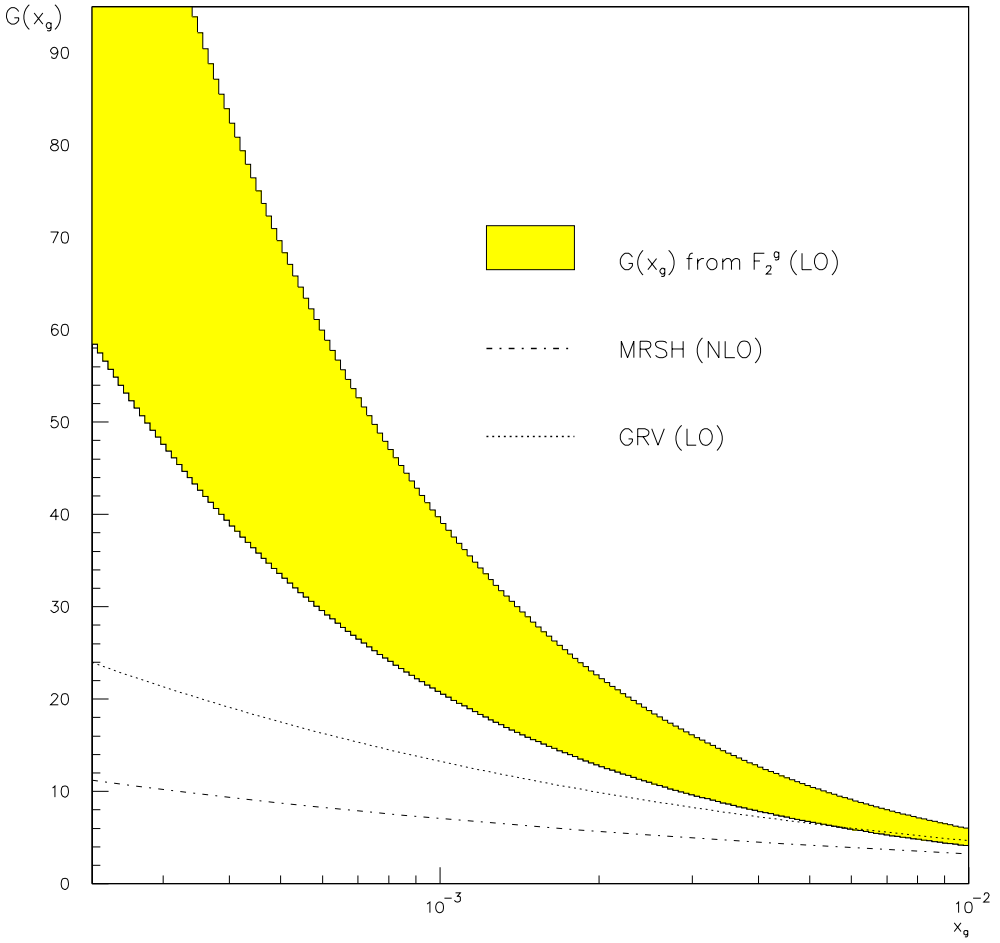

Figure 8.14: The shaded band shows the $O(\alpha_s)$ gluon density $G(x_g)$ at $Q^2 = 4$ GeV^2, extracted in the leading $\log Q^2$ approximation from F_2^g. Also shown is the GRV leading order gluon density and the next-to-leading order gluon density from the MRSH set of parton distribution functions at the same Q^2.

The H1 collaboration has used other methods to extract a leading order gluon density in the proton. The results from these analyses are shown in figure 8.15 along with the result from the fit to F_2^g, extrapolated to the range $10^{-4} < x < 1$. The open circles show the result from an analysis based on the measured rate of (2+1) jets [40]. The full circles and the dotted line show the results from two different approaches to extracting $G(x_g)$ from the measured F_2 values [41]. The Q^2 values at which these gluon densities are quoted are different, so they are not directly comparable. However it is interesting to observe that the only measurement which extends to as low values of x_g as the analysis presented in this thesis is the leading order QCD fit to F_2.

The $O(\alpha_s)$ gluon density which has been extracted from F_2^g is large, although it is consistent with the momentum sum rule (see section 2.4). It shows a rise with decreasing x_g which is steeper than either the GRV ($\alpha \sim -0.4$) or the MRSH ($\alpha \sim -0.3$) gluon densities. It is also larger at low x_g than the leading order gluon density extracted from a QCD fit to F_2. The results indicate that further understanding is required to relate the measured F_2^g to the gluon density in the proton. The method presented here includes certain assumptions. For example, it does not address the fact that in LEPTO the phase space for the partons in both QCD Compton and BGF events is limited by the invariant mass cut-off. It is assumed that the energy flow in the central region of $\cos\theta^*$ (and hence the values of a_0) is determined by the colour force and that the effect of the parton kinematics is small. This is, however, only an approximation, and a more sophisticated measurement of $G(x_g)$ must explicitly include the effect of this limited phase space in the Monte Carlo events. Also, the assumption is made that we are probing the gluon density in the proton. When the total invariant mass of the hadronic final state (W) is large, the probability that the exchanged photon is no longer a structureless probe but that it has dressed into partons is significant. In this case, it is no longer clear that we are directly measuring proton structure.

It must be stressed therefore that, at present, the interpretation of F_2^g is incomplete. Further theoretical insight is required before the gluon density extracted from F_2^g can be meaningfully compared to theoretical parameterisations and other experimental results.

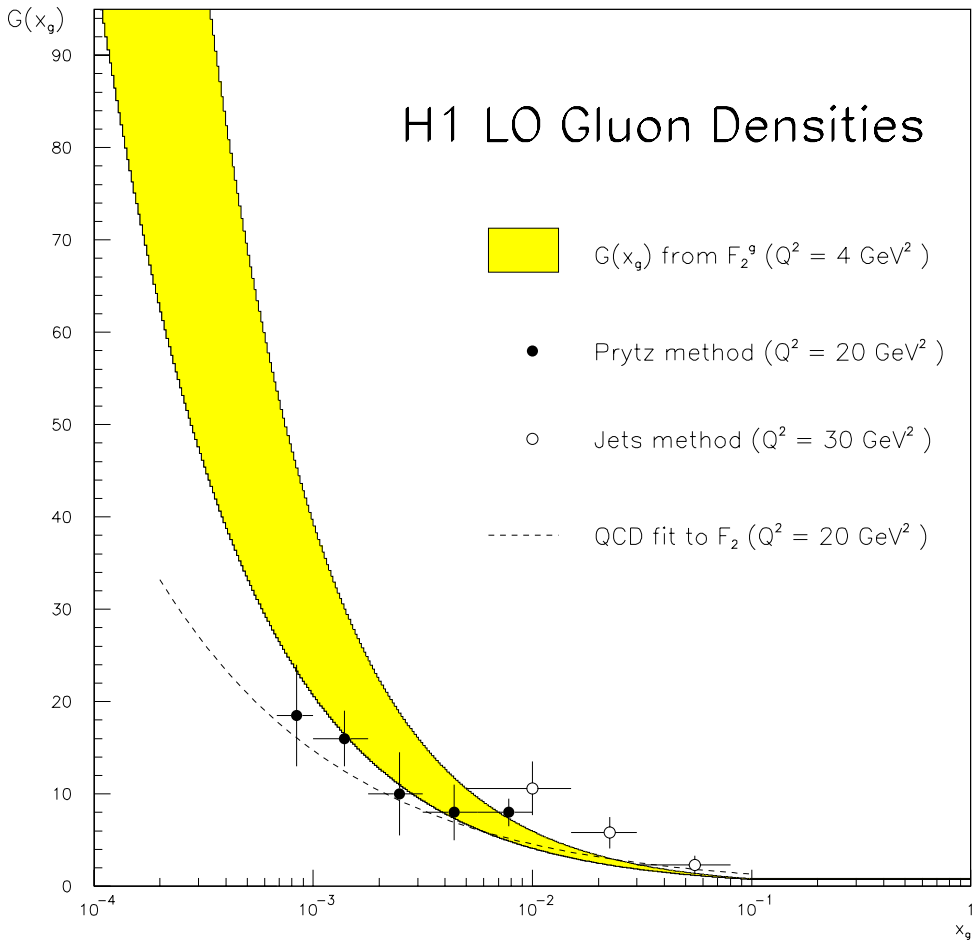

Figure 8.15: The shaded band shows the O(α_s) gluon density $G(x_g)$ at $Q^2 = 4$ GeV^2, extracted in the leading $\log Q^2$ approximation from F_2^g. Also shown is the leading order gluon density at $Q^2 = 30$ GeV^2 calculated from the rate of (2+1) jets (open cicles) and the results from two different approaches to measuring $G(x_g)$ from F_2 (the black points and dotted line), both at $Q^2 = 20 GeV^2$.

Chapter 9

Summary and Conclusions

The work discussed in this thesis is a first attempt at understanding the composition of the proton in the kinematic region $10^{-4} < x < 10^{-2}$ and $5 < Q^2 < 100$ GeV^2 by studying the colour structure of the remnant in neutral current DIS.

It has been demonstrated that the way in which the total available energy is distributed in the hadronic final state is different for events in which the remnant is in a colour octet state ('gluon initiated' processes) than for events in which it is in a colour triplet or anti-triplet state ('quark initiated' processes). This is a direct consequence of the fact that the force between two colour octets is 9/4 times stronger than the force between a colour triplet and an anti-triplet.

Subsequently, the fraction of gluon initiated processes (f_g) as a function of x and Q^2 has been measured by finding that mixture of processes (as modelled by LEPTO with detector simulation) which is able to reproduce the energy flow in the central region of $\cos\theta^*$ in the HCMS observed in the data. The resulting fractions are all consistent with being less than one, within errors. When the events are reweighted such that the fraction of BGF is equal to the measured f_g, LEPTO is able to describe the transverse energy flow in the forward region of the detector, which the standard version of LEPTO is not able to do. The description of the E_t flow is still not perfect, however, probably owing to the crude nature of the reweighting technique. The fact that a standard DGLAP Monte Carlo with a steep gluon distribution is able to describe the forward energy has implications for the search for BFKL signatures in the data.

The extraction of G(x) from this measurement is theoretically complicated.

One possible approach has been shown, which involves calculating the contribution to the total F_2 from gluon initiated processes. The resulting gluon distribution rises steeply with decreasing x. However, it is not clear as of yet how this measurement can be compared either to parameterisations of $G(x)$ or to other measurements. This requires further theoretical input.

Appendix A

Colour Factors

A.1 Introduction

For each flavour of quark, there are three colour states, conventionally labelled red (r), green (g) and blue (b). Gluons are bicoloured, and exist in eight different colour states:

$$r\bar{b}, r\bar{g}, b\bar{g}, b\bar{r}, g\bar{b}, g\bar{r}, \frac{r\bar{r} - b\bar{b}}{\sqrt{2}}, \frac{r\bar{r} + b\bar{b} - 2g\bar{g}}{\sqrt{6}}$$

In QCD, the strength of the coupling for single gluon exchange between two colour charges is $\frac{1}{2}c_1 c_2 \alpha_s$ [42] where c_1 and c_2 are the colour coefficients associated with the vertices. The colour factor C_F is defined as:

$$C_F \equiv \frac{1}{2} |c_1 c_2|$$

A.2 Colour factor for quark initiated processes.

In a QPM or a QCD Compton event, the proton remnant is left in a colour triplet (or anti-triplet) state. As there was no net colour before the interaction there must be no net colour in the final state. This means that the final state excluding the proton remnant (the struck quark for QPM events and the combination of the quark and gluon for QCD Compton events) must be in a colour anti-triplet (or triplet) state. Thus the force between the proton remnant and the partons in the final state for the two 'quark initiated' processes is identical to the force between

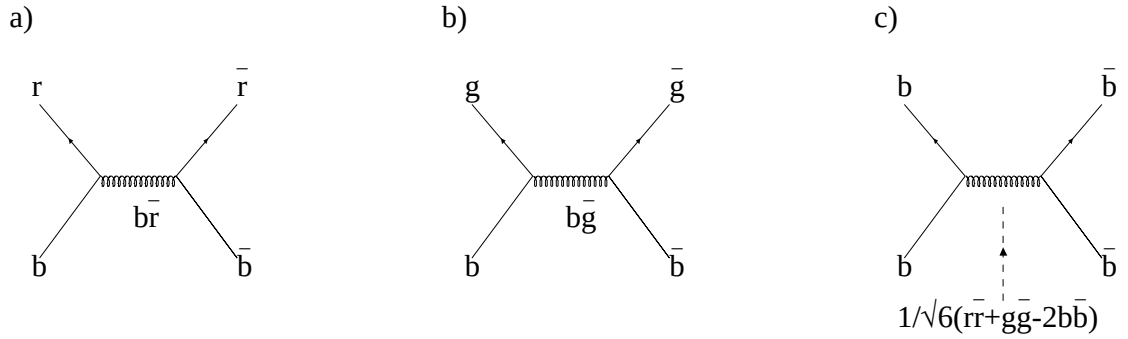

Figure A.1: Diagram showing the colour flow for the interaction between a quark and anti-quark of the same colour, in this case blue. The interaction is mediated by single gluon exchange.

a quark and an anti-quark of the same colour, except for a 'form factor' which must be included to take into account the spatial extent of the proton remnant.

Consider the interaction between a blue quark and anti-quark, mediated by single gluon exchange. The colour factor is independent of this choice of colour. We also apply the constraint that there is no net colour in the final state.

There are three possible final states ($r\bar{r}$, $b\bar{b}$ and $g\bar{g}$) and these are shown in A.1*a*–*c*.

In figure A.1*a* the colour state of the exchanged gluon is $b\bar{r}$ and c_1 are c_2 are both 1. Similarly, in figure A.1*b* the colour state of the exchanged gluon is $b\bar{g}$ and again c_1 and c_2 are both 1. However, in figure A.1*c* the exchanged gluon has the form $\frac{1}{\sqrt{6}}(r\bar{r} + g\bar{g} - 2b\bar{b})$, giving a colour coefficient at each vertex of $\frac{2}{\sqrt{6}}$.

Thus the colour factor for the interaction between a quark and anti-quark of the same colour is:

$$\begin{aligned} C_F^{q\bar{q}} &= \frac{1}{2}(1 + 1 + \frac{2}{3}) \\ &= \frac{4}{3} \end{aligned}$$

A.3 Colour factor for gluon initiated processes.

In a BGF event the proton remnant is left in a colour octet configuration and the $q\bar{q}$ also forms a colour octet. In this case, the force between the proton remnant and the $q\bar{q}$ pair is equivalent to the force between two gluons, where the gluons have equal and opposite colour quantum numbers, again except for a form factor to account for the finite size of the proton remnant.

Consider the interaction between two gluons, mediated by single gluon exchange. The interacting gluons must have equal and opposite colour, and we chose them to have the colour composition $r\bar{b}$ and $b\bar{r}$ respectively. The colour factor will be the same independent of this choice. There must also be no net colour in the final state.

Figure A.2 shows the colour flow in this case. The exchanged gluon is of the form $x\bar{b}$, where x can be either r, b and g. At each vertex there are three contributions to the colour coefficients. These are referred to as c_a, c_b etc according to diagrams a–f, with $c_1 = c_a c_b c_c$ and $c_2 = c_d c_e c_f$. The coefficients c_a and c_d do not depend on the choice of x and both have the value 1.

Let us suppose that the unknown colour x is blue (b). The exchanged gluon must therefore be in the colour state $\frac{1}{\sqrt{6}}(r\bar{r} + g\bar{g} - 2b\bar{b})$, and the two gluons in the final state are in the colour states $r\bar{b}$ and $b\bar{r}$ respectively. Thus c_b is 1 and c_c is $\frac{2}{\sqrt{6}}$ giving a colour coefficient of $\frac{2}{\sqrt{6}}$ for the vertex V1. We can also deduce that c_2 is $\frac{2}{\sqrt{6}}$.

In the same way, it is possible to calculate the colour factors assuming that x is either red or green. The results are shown in table A.1. There are two contributions to the colour factor when the exchanged gluon is in the state $r\bar{b}$ because the two final state gluons could either both have the form $\frac{1}{\sqrt{2}}(r\bar{r} - g\bar{g})$ or both have the form $\frac{1}{\sqrt{6}}(r\bar{r} + g\bar{g} - 2b\bar{b})$. In addition, as we have two identical gluons in the final state, we have two contributing diagrams, shown in A.3, so the colour factors must be multiplied by a factor two.

The exchanged gluon could also have the form $b\bar{x}$, with x being r, g or b. Thus we must include a further factor of two to take these diagrams into account.

Combining all this information gives the colour factor as:

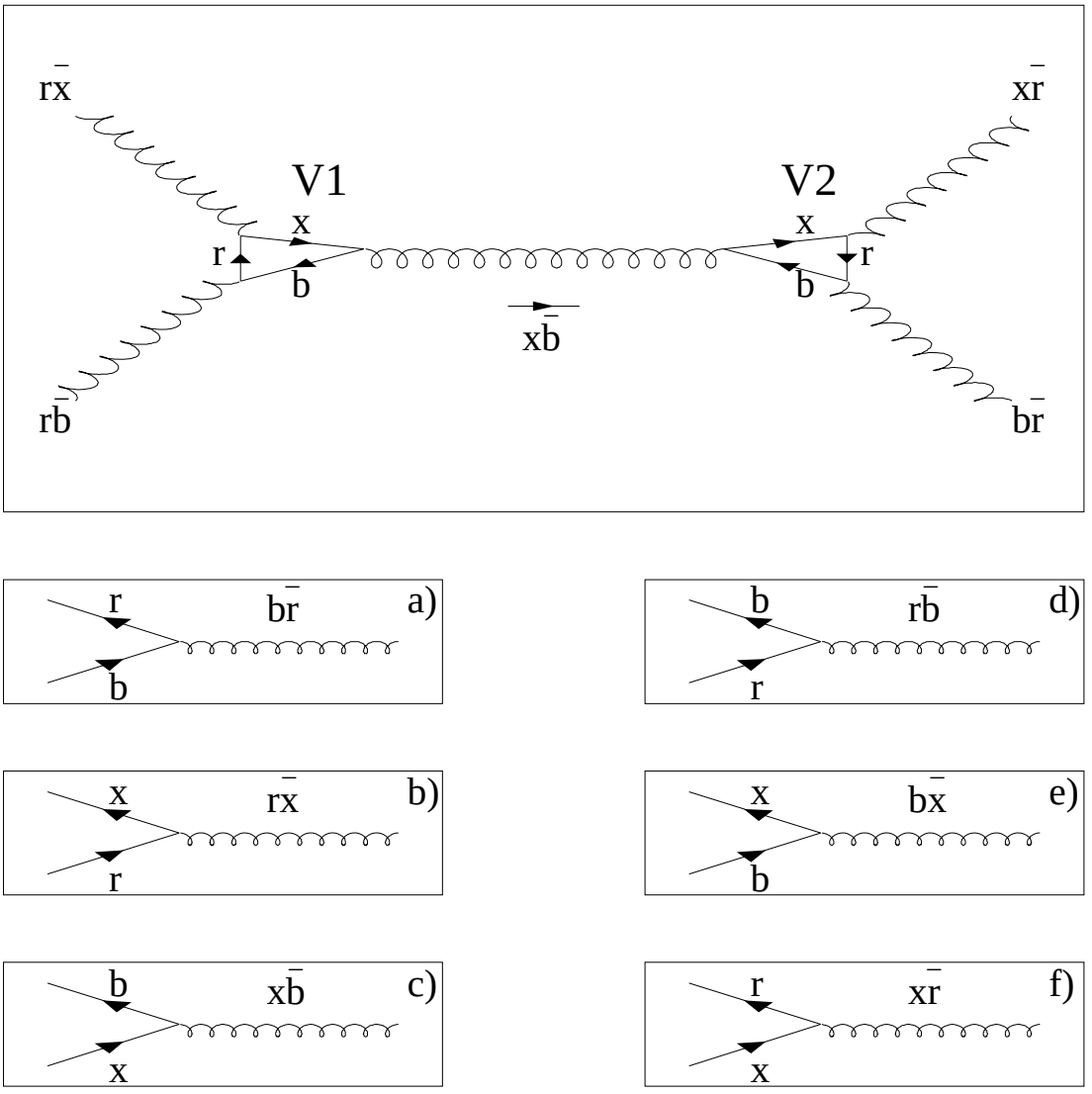

Figure A.2: The interaction between two gluons of equal and opposite colour, as mediated by single gluon exchange. Figures *a–c* show the three contributions to the colour coefficient at the vertex V1 and figures *d–f* show the contributions to the colour coefficient at the vertex V2.

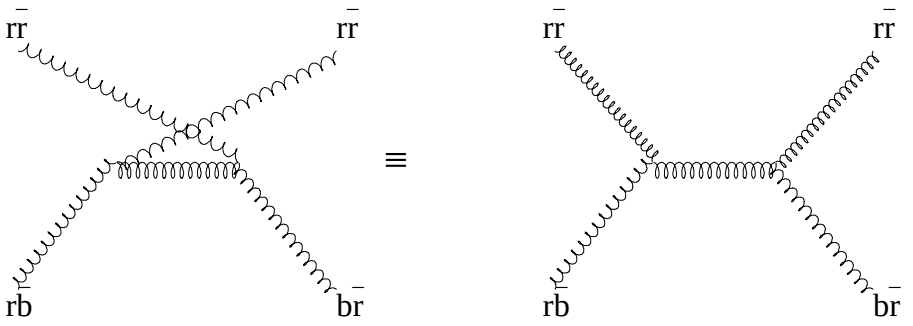

Figure A.3: These two diagrams are indistinguishable when there are identical gluons in the final state.

	V1			V2		
x	c_a	c_b	c_c	c_d	c_e	c_f
green	1	1	1	1	1	1
blue	1	1	$\frac{2}{\sqrt{6}}$	1	1	$\frac{2}{\sqrt{6}}$
red	1	$\frac{1}{\sqrt{2}}$	1	1	$\frac{1}{\sqrt{2}}$	1
	1	$\frac{1}{\sqrt{6}}$	1	1	$\frac{1}{\sqrt{6}}$	1

Table A.1: The colour coefficients for figure A.2 when x is red, green and blue.

$$\begin{aligned} C_F^{gg} &= 2 \times \frac{1}{2} \left| 2 \times \left(\frac{1}{2} + \frac{1}{6} \right) + \frac{2}{3} + 1 \right| \\ &= 3 \end{aligned}$$

A.4 Conclusion

We have calculated the colour factors for the interaction between a quark and an anti-quark of the same colour and for the interaction between two gluons with equal but opposite colour quantum numbers. Also, we have explained that these can only be related to the colour forces in quark and gluon initiated processes if we include a form factor to take into account the spatial extent of the proton remnant. However, if we assume that the proton remnant is similar for the two processes, the form factors will be the same and we can thus conclude that the ratio of the colour factors for quark and gluon initiated processes is:

$$\frac{C_F^{gg}}{C_F^{q\bar{q}}} = \frac{9}{4}$$

Appendix B

Determination of f_g

B.1 Energy flow in the HCMS

Assume the particles in the HCMS are distributed in angle and energy according to the probability distribution $P(z, E)$, where z=cos θ^*. The number of particles between z and $z + dz$ which have an energy between E and $E + dE$ is:

$$d^2n = NP(z, E)\, dE\, dz \tag{B.1}$$

for a sample of N events.

However, due to the finite acceptance of the H1 detector not all the particles will be detected. If the acceptance function is $A(z, E)$, such that $0 \leq A(z, E) \leq 1$, then the measured number of particles in the H1 detector between z and $z + dz$ with energy between E and $E + dE$ is :

$$d^2n = NP(z, E)A(z, E)\, dz\, dE \tag{B.2}$$

So the total energy in the detector between z and $z + dz$ is:

$$dE^{det} = \int_E ENA(z, E)P(z, E)\, dz\, dE \tag{B.3}$$

and the total number of events recorded by H1 will be:

$$N^{det} = \int_E \int_{-1}^{1} NA(z, E)P(z, E)\, dz\, dE \tag{B.4}$$

Thus, the mean energy per event detected in H1 between z and $z + dz$ is:

$$d\bar{E}^{det} = \frac{N\,dz \int\limits_{E} EA(z,E)P(z,E)\,dE}{N \int\limits_{E}\int\limits_{-1}^{1} A(z,E)P(z,E)\,dz\,dE} \tag{B.5}$$

It follows, therefore, that the average energy flow per event in the detector can be expressed as:

$$\frac{d\bar{E}^{det}}{dz} = \frac{\int\limits_{E} EA(z,E)P(z,E)\,dE}{\int\limits_{E}\int\limits_{-1}^{1} A(z,E)P(z,E)\,dz\,dE} \tag{B.6}$$

In practice, we choose to express the average energy detected as a fraction of the total available energy, W. If we define:

$$d\omega = \frac{d\bar{E}^{det}}{W}$$

then:

$$\frac{d\omega}{dz} = \frac{\int\limits_{E} EA(z,E)P(z,E)\,dE}{W \int\limits_{E}\int\limits_{-1}^{1} A(z,E)P(z,E)\,dE} \tag{B.7}$$

B.2 The data as a mixture of $O(\alpha_s)$ processes

Assume that the data sample is composed of gluon initiated events (BGF) and quark initiated events (QPM and QCD Compton) only. The two classes of events will have different probability distributions and different acceptance functions owing to the different event topologies. Thus, we can write (see B.2):

$$d^2n_q = N_q A_q(z,E)P_q(z,E)\,dz\,dE \tag{B.8}$$

and:

$$d^2n_g = N_g A_g(z,E)P_g(z,E)\,dz\,dE \tag{B.9}$$

where the subscript q refers to the quark initiated processes and g refers to gluon initiated processes. The measured population of particles in the detector is:

$$d^2n_d = d^2n_q + d^2n_g \tag{B.10}$$

where the subscript d refers to the data sample. Using this, equation B.7 can be written:

$$\frac{d\omega_d}{dz} = \frac{\int\limits_E \left\{N_q E A_q(z,E) P_q(z,E) + N_g E A_g(z,E) P_g(z,E)\right\} dE}{W \int\limits_E \int\limits_{-1}^{1} \left\{N_q A_q(z,E) P_q(z,E) + N_g A_g(z,E) P_g(z,E)\right\} dz\, dE} \tag{B.11}$$

If we define f_g as the fraction of gluon initiated events in our sample of N events, this can also be written:

$$\frac{d\omega_d}{dz} = \frac{\int_E \left\{(1-f_g) E A_q(z,E) P_q(z,E) + f_g E A_g(z,E) P_g(z,E)\right\} dE}{W \int\limits_E \int\limits_{-1}^{1} \left\{(1-f_g) A_q(z,E) P_q(z,E) + f_g A_g(z,E) P_g(z,E)\right\} dz\, dE} \tag{B.12}$$

However, we can also express the average energy deposition for a quark event (see B.5) as:

$$\frac{d\omega_q}{dz} = \frac{N_q \int\limits_E E A_q(z,E) P_q(z,E)\, dE}{W N_q^{det}} \tag{B.13}$$

where N_q^{det} is the total detected number of quark initiated events. Using the definition:

$$\epsilon_q = \frac{N_q^{det}}{N_q} = \int\limits_E \int\limits_{-1}^{1} A_q(z,E) P_q(z,E)\, dz\, dE \tag{B.14}$$

then equation B.13 becomes:

$$\frac{d\omega_q}{dz} = \frac{\int\limits_E E A_q(z,E) P_q(z,E)\, dE}{W \epsilon_q} \tag{B.15}$$

ϵ_g can be defined in a similar way for gluon initiated processes.

Using equations B.14 and B.15, B.12 can be written:

$$d\omega_d = \frac{\epsilon_g f_g d\omega_g + \epsilon_q (1-f_q) d\omega_q}{f_g \epsilon_g + (1-f_g)\epsilon_q} \tag{B.16}$$

B.3 Expansion in terms of orthogonal functions

The energy flow per event as a fraction of the available energy W between symmetric limits in z ($|z| < c$) can be expanded in terms of a series of orthogonal functions, $f_l(z)$:

$$d\omega = \sum_l a_l f_l(z) \tag{B.17}$$

The coefficients of this expansion are defined by:

$$a_l = \frac{\int_{-c}^{c} \frac{d\omega}{dz} f_l(z)\, dz}{\int_{-c}^{c} f_l^2(z)\, dz} \tag{B.18}$$

given that the functions $f_l(z)$ are orthogonal, meaning that:

$$\int_{-c}^{c} f_l(z) f_k(z)\, dz = \text{ constant } \times \delta_{lk} \tag{B.19}$$

In practice, the distribution is expanded in terms of a series of Legendre polynomials. The coefficients of the polynomials are modified such that:

$$\int_{-c}^{c} f_l(z) dz = 0 \,\text{for}\, i > 0 \tag{B.20}$$

The term in the expansion which is significantly different for quark and gluon initiated processes is the constant term, a_0. From B.18:

$$a_0 = \frac{\int_{-c}^{c} \frac{d\omega}{dz}\, dz}{2c} \tag{B.21}$$

However, from equation B.16:

$$\int_{-c}^{c} \frac{d\omega_d}{dz}\, dz = \frac{\epsilon_g f_g \int_{-c}^{c} \frac{d\omega}{dz}\, dz + \epsilon_q (1 - f_g) \int_{-c}^{c} \frac{d\omega}{dz}\, dz}{\epsilon_g f_g + \epsilon_q (1 - f_g)} \tag{B.22}$$

so:

$$a_d^0 = \frac{\epsilon_g f_g a_g^0 + \epsilon_q (1 - f_g) a_q^0}{\epsilon_g f_g + \epsilon_q (1 - f_g)} \tag{B.23}$$

Re-arranging this expression, the fraction of gluon initiated processes, f_g is given by:

$$f_g = \frac{\epsilon_q (a_0^d - a_0^q)}{\epsilon_g a_0^g - \epsilon_q a_0^q - a_0^d (\epsilon_g - \epsilon_q)} \tag{B.24}$$

References

[1] S. Bentvelsen, J. Engelen, P. Kooijman, Proceedings of the HERA Workshop Vol. 1 (October 1991), ed. W. Buchmüller and G. Ingelman, p. 23

[2] G. Miller et al., Phys. Rev. **D5** (1972) 528

[3] C. Callan and D. Gross, Phys. Rev. Lett. **22** (1969) 156

[4] A. Martin, R. Roberts, W. Stirling, J. Phys. **G19** (1993) 1429

[5] A. Bodek et al., Phys. Rev. Lett. **30** (1973) 1087
A. Bodek et al., Phys. Lett. **51B** 417

[6] F. Halzen and A. Martin, *Quarks and Leptons*,
Wiley (1984), ISBN 0-471-88741-2, p. 229

[7] F. Halzen and A. Martin, *Quarks and Leptons*,
Wiley (1984), ISBN 0-471-88741-2, p. 215

[8] BCDMS Collaboration, Phys. Lett. **B223** (1989) 485

[9] G. Altarelli, G. Parisi, Nucl. Phys. **B126** (1977) 298 V. Gribov, L. Lipatov, Sov. Journal Nucl. Phys 15 (1972) 438 and 675

[10] E. Kuraev, L. Lipatov, V. Fadin, Phys. Lett. **60B** (1975) 50

[11] A. Martin and W. Stirling, *Parton Distributions of the Proton*,
RAL preprint, RAL-94-055 (1994)

[12] G. Ingelman, Proceedings of the HERA Workshop Vol. 3 (October 1991), ed. W. Buchmüller and G. Ingelman, p. 1366

[13] T. Sjostrand and M. Bengtsson, Comput. Phys. Commun. **43** (1987) 367

[14] B. H. Wiik, *Status of HERA and First Results*
Proceedings of Dallas Conference 1992 (High Energy Physics) Vol. 1 p. 278

[15] H1 Collaboration, *The H1 detector at HERA*
DESY preprint, DESY-93-103 (1993)

[16] H1 Calorimeter Group, *The H1 Liquid Argon Calorimeter System*
NIM **A336** (1993) 460-498

[17] H1 Calorimeter Group, *Results from Pion Calibration runs for the H1 Liquid Argon Calorimeter and Comparison with Simulations*,
DESY preprint, DESY-93-047 (1993)

[18] BEMC Group, *The H1 Backward Electromagnetic Calorimeter(BEMC)*
H1 Internal Note H1-08/92-233 (1992)

[19] G. Bernardi(Editor), DESY central IBM,
'HERA01.H1REC.DOC' and files therein

[20] F. Charles, *Measurement of the proton structure function F_2 in the experiment H1*, H1 Internal Note, H1-09/94-377 (1994)

[21] J. Ban et al, *The BEMC Single Electron Trigger*
H1 Internal Note H1-07/92-235 (1992)

[22] H1 Collaboration, *A Measurement of the Proton Structure Function $F_2(x, Q^2)$*, DESY preprint 95-006 (1995)

[23] H1 Collaboration, Z. Phys. **C63** (1994) 377

[24] C. Hilton, *Forward Muon Detection in H1 and Hadronic Energy Flow in Deep Inelastic Scattering*, University of Manchester (1993).

[25] K. Muller, *Results on the Proton Structure Function F_2 and the Diffractive Contribution to F_2*, H1 Internal Note, H1-05-94-360

[26] H. Kuester, *On the treatment of Calorimeter Cells and Clusters in H1REC and PHAN physics analysis*, H1 Internal Software Note 45 (1994)

[27] H1 Collaboration, Nucl. Phys. **B429** (1994) 477

[28] H1 Collaboration, *First Measurement of the Deep-Inelastic Structure of Proton Diffraction*, DESY preprint 95-036 (1995)

[29] G. Ingelman, *LEPTO version 6.1 - The Lund Monte-Carlo for Deep Inelastic Lepton-Nucleon Scattering*, Proceedings of the HERA Workshop (October 1991) Vol. 3, p.1366, ed. W. Buchmüller and G. Ingelman

[30] J. Meyer (Editor),*Guide to the Simulation Program H1SIM* DESY Central IBM, 'HERA01.H1SIM.GUIDE', Hamburg(1991)

[31] H1 Collaboration, Phys. Lett. **B298** (1993) 469

[32] C. Brune et al., *BEMC Calibration 1993* H1 internal note, H1-04/94-352 (1994)

[33] EMC Collaboration, Phys. Lett **100B** (1981) 433

[34] V. Hedberg et al., *Asymmetries in Jet Azimuthal Angle Distributions as a Test of QCD*, Proceedings of the HERA Workshop (October 1991) Vol. 1, p.331, ed. W. Buchmüller and G. Ingelman

[35] H1 Collaboration, Z. Phys. **C61** (1994) 59

[36] J. Kwieciǹski et al., Phys. Rev. **D50** (1994) 217

[37] J. Kwieciǹski et al., Phys. Lett. **B335** (1994) 220

[38] H. Spiesberger et al., *Radiative Corrections at HERA* , Proceedings of the HERA Workshop (October 1991) Vol. 2, p.798, ed. W. Buchmüller and G. Ingelman

[39] M. Glück, E. Reya, A. Vogt, Z. Phys. **C53** (1992) 127
M. Glück, E. Reya, A. Vogt, Phys. Lett. **306B** (1993) 391

[40] H1 Collaboration, *A Measurement of the Gluon Density at Low x from Multijet Events*, to be published

[41] H1 Collaboration, *The Gluon Density of the Proton at Low x from a QCD Analysis of* F_2, to be published

[42] F. Halzen and A. Martin, *Quarks and Leptons*, Wiley (1984), ISBN 0-471-88741-2, p. 67